VILNIUS UNIVERSITY
CENTER FOR PHYSICAL SCIENCES AND TECHNOLOGY

Andrius
PAULAUSKAS

Total internal reflection ellipsometry in metal and/or dielectric hybrid nanostructures

DOCTORAL DISSERTATION

Natural sciences,
Physics N002

VILNIUS 2019

This dissertation was written between 2013 and 2019 at Center for physical sciences and technology.

Academic supervisor:
Prof. Dr. Zigmas, Balevičius (Center for physical sciences and technology, natural sciences, physics – N 002).

Table of Contents

INTRODUCTION

Optical sensors are now widely used in various applications for the monitoring of surface modification by gas or bio-molecular processes [1–3]. Optical methods do not require physical or electrical contact with studied materials. This fact makes them non-destructive and non-invasive what is important at the nanoscale range of a thin film, or in situ monitoring of gas-, bio- or chemical studies. One of the common optical configurations used in gas-, bio- or chemical sensor design is the exploitation of total internal reflection (TIR) phenomenon [4]. This makes possible the monitoring of various adsorption processes on surfaces and their interaction with gas-, bio-substances in opaque media [5]. TIR setups are used in surface plasmon resonance (SPR) based optical sensors [6], reflectometry [7], interferometry [8] and in infrared techniques [9]. Ellipsometry also is used in TIR configuration [10]. Ellipsometry under total internal reflection mode called Total Internal Reflection Ellipsometry and applied as a sensor system for measurements in gaseous and aqueous media provides high sensitivity. The combination of ellipsometry and the SPR phenomenon (also called Total Internal Reflection Ellipsometry (TIRE)) uses a prism to obtain total internal reflection. This gives extremely high sensitivity to surface changes, when compared with traditional ellipsometry configurations and SPR in intensity interrogation modes [11]. The exploitation of the SPR phenomenon demands a semitransparent metal film (commonly gold). The application of a glass prism as an optical element to obtain internal reflection provides the possibility of studying surface modification or, for example, biomolecule immobilization processes without the light beam passing through the liquid medium where these processes occur. The main difference, however, between SPR and TIRE is that SPR utilizes only the intensity of reflected p- polarized light, meanwhile TIRE exploits ellipsometric principal and analyses both p- and s- polarizations. Regarding, the phase information in terms of ellipsometric parameter Δ is obtained as well as Ψ the ratio between amplitudes of p- and s- polarization. The sensitivity of Δ ellipsometric parameter for the interface and surface structures for angles of light incidence larger than the critical is the main feature of TIRE. The increased sensitivity in Δ parameter manifests in interfaces without metal layer as well as in combination with plasmonic effect.

However, rather small number of publications have been dedicated for studies of dielectric thin films in internal reflection ellipsometry modes [12]. An enhancement of the ellipsometric optical response due to multiple

reflection inside the additional dielectric tantalum oxide surface layer with a high refractive index in internal reflection configurations has been reported [13–15].
This Ph.D. thesis is dedicated to expand TIRE applications exploiting the novel type hybrid Tamm-plasmon polaritons modes for sensing applications not only for dielectric thin films, but also for structures which change the optical conductivity of plasmon active layers. Also, the studies related with bio-molecular sensing at the dielectric/dielectric interface, which are still underestimated in the field of optical sensors, where examined in TIRE with nanolaminates.

Objectives

The objectives of this Ph.D. thesis were to reveal the advanced possibilities of TIRE method with different plasmonic excitations such as SPP, TPP and hybrid TPP-SPP and also with biocompatible dielectric interfaces without metal layer in case when they are not preferable. The main contribution of the studies was related with hybrid TPP-SPP mode generation in TIRE setup and these modes application for plasmonic sensors with materials which change the conductivity of plasmon active layer. In particular, focusing on the investigation of:

- the influence of the interaction of Hg with an Au surface on the optical response of gold-based sensor and, as a result, on the determination of the composition by a percentage of the amalgam layer.
- the amalgam which also was used to study the fundamental properties of hybrid plasmonic modes as the material with high conductivity at optical frequencies, in order to have the possibility to tune the total dielectric function of the sensing layer through the presents of amalgam formation, which influence the coupling strength between the TPP and SPP resonances in the hybrid TPP-SPP mode.
- to investigate the kinetic features of mercury vapor adsorption onto gold surfaces by utilizing the hybrid TPP-SPP mode in TIRE configurations and demonstrate the advanced capabilities of such hybrid excitation in the design of plasmonic sensors.
- to evaluate the influence of the layered structures of Al_2O_3/ZnO nanolaminates on the optical responses of ellipsometric parameters Ψ and Δ in total internal reflection configurations and to demonstrate

the advanced possibilities of such layered structures in optical biosensors designs.

Tasks to achieve the objectives:

- to develop an adequate optical model using involving the Bruggeman EMA and taking into account the surface roughness for inhomogeneous surface structures containing mercury and gold atoms which formed during the initial phases of amalgam formation.
- to generate the ellipsometric spectra of hybrid TPP-SPP mode in TIRE configuration on the structure PC/gold layer.
- to compare the sensitivity features of a single SPR, a single TPP and hybrid TPP-SPP modes for mercury detection on the plasmon active gold layer.
- to study the coupling strength of the hybrid TPP-SPP mode through the repulsion of TPP and SPP components of the dispersion curves
- to develop the multi-layer optical model which reasonably well described the penetration of mercury atoms into the gold layer and further amalgam formation
- to apply the hybrid TPP-SPP mode as a sensor probe for the real time formation of amalgam structures on the surface of a plasmon active gold layer.
- to conduct the numerical simulations of the optical response of Al_2O_3/ZnO nanolaminates in TIRE configuration for optimized optical sensitivity
- to determine the thicknesses and dispersions of refractive indices of the Al_2O_3/ZnO nanolaminates from the spectroscopic ellipsometry
- to measure experimentally the evolution of ellipsometric parameters in time during BSA protein interaction with APTES surface
- evaluate the Al_2O_3/ZnO nanolaminates as possible substrates for biosensing purposes

Scientific novelty

The experimental optical studies conducted in the present Ph.D. thesis are in the field of emerging area of plasmonics and optical gas-/bio-sensing

applications.

The main novelty of these optical studies is the employed, for the first time, the spectroscopic ellipsometry in total internal reflection configuration for the generation and study of the hybrid Tamm plasmon polariton - surface plasmon polariton mode. The gold/mercury amalgam formation features and the penetration of the mercury atoms into the gold layer were determined by means of the experimental TIRE data and a regression analysis of a multi-layer model containing the index-profile amalgam layer.

From a point of view of a plasmonic surface waves physics the studies of the amalgam formation was to use mercury as a material with high conductivity at optical frequencies, in order to have the possibility to tune the total dielectric function of the sensing layer through the presents of amalgam formation, which, in turn, influence the coupling strength between the TPP and SPP resonances in the hybrid TPP-SPP mode.

It has been shown that the application of the Bruggeman EMA model for the real time TIRE spectra allowed reliably to evaluate the percentage composition of inhomogeneous structures such as gold/mercury amalgam. It should be noted that during the interaction of the mercury with the gold, the surface roughness of the gold increases in most cases. This fact creates a challenge, however, for optical methods due to increased light scattering. The present studies have shown, however, that the application of TIRE and an effective medium approximation can solve this problem reasonably well.

The spectroscopic dynamic TIRE method was utilized for the characterization of the real time formation of the BSA layer on the surface of the functionalized Al_2O_3/ZnO nanolaminates. The use of TIRE method for biosensing purposes with multilayer dielectric Al_2O_3/ZnO nanolaminates substrates produce possibilities of constructing optical biosensors with advanced features when metal surfaces are not possible to apply. The increased sensitivity of the ellipsometric parameters can be explained by the multiple reflection of the light waves in a condition of total internal reflection, especially for ellipsometric parameter Δ. These studies showed that the number of bilayers and the thicknesses of the films have a noticeable influence on the sensitivity of these kinds of optical biosensors.

Scientific statements

- The spectroscopic real time TIRE method and the adequate optical model involving Bruggeman EMA enables to characterize the

percentage composition changes of the inhomogeneous gold/mercury amalgam surface structures in time.

- The coupled excitations of the hybrid TPP-SPP mode gives information about the penetration of the mercury atoms into the gold layer and depth profile Au/Hg amalgam. This method based on the repulsion of the dispersion curves due to conductivity changes on the surface of plasmon active layer.
- In TIRE setup the sensitivity of optical response of ellipsometric parameters $\Delta(\lambda)$ and $\Psi(\lambda)$ during protein adsorption on the surface is enhanced due multiple total internal reflections in periodic multilayer Al_2O_3/ZnO structure compared with the same thickness of single ZnO layer.

Structure of the dissertation

Chapter 1 presents the literature survey of spectroscopic ellipsometry basics, total internal reflection with several dielectric layers or metals, surface plasmon polariton and Tamm plasmon phenomenon descriptions.
Chapter 2 presents materials and methods used in this work.
Chapter 3 presents ellipsometric investigation and analysis of real time thin gold layer amalgamation, laminated structure feasibility as an alternative for total internal reflection sensing when metals cannot be used along with real time amalgamation investigation using a hybrid mode of surface plasmon - Tamm plasmon.
Chapter 4 presents main results, discussions and conclusions.

Authors contribution
The author of the dissertation performed ellipsometric measurements in mercury sorption experiments and participated in biosensing capabilities investigation experiment. Participated in the analysis of results and data presentation: optical response modelling, manuscript preparation and layout, preparation for answers to the questions of article reviewers.

List of publications
Scientific papers
[1]* A.Paulauskas, A.Selskis, V.Bukauskas, V.Vaicikauskas, A.Ramanavicius, Z.Balevicius, Real time study of amalgam formation and mercury adsorption on thin gold film by total internal reflection

ellipsometry, Appl. Surf. Sci., **427**, 298-303(2018), https://doi.org/10.1016/j.apsusc.2017.08.236

[2]* Z.Balevicius, A. Paulauskas, I. Plikusiene, L. Mikoliunaite, M. Bechelany, A. Popov, A. Ramanavicius, A. Ramanaviciene, Towards the application of Al2O3/ZnO nanolaminates in immunosensors: total internal reflection spectroscopic ellipsometry based evaluation of BSA immobilization, J. Mater. Chem. C, **6**, 8778-8783(2018), https://doi.org/10.1039/c8tc03091j

[3]* A. Paulauskas, S. Tumenas, A. Selskis, T. Tolenis, A. Valavicius, Z. Balevicius, Hybrid Tamm-surface plasmon polaritons mode for detection of mercury adsorption on 1D photonic crystal/gold nanostructures by total internal reflection ellipsometry, Opt. Express, **26**, 30400-30408(2018), https://doi.org/10.1364/OE.26.030400

International conferences

1. A.Paulauskas, S. Tumėnas, C. Karam, I. Balevičiūtė, M. Bechelany, L. Mikoliūnaitė, P. Miele, A. Ramanavičienė, A. Ramanavičius, Z. Balevičius, Optical response of urchin-like ZnO nanowires analyzed by spectroscopic ellipsometry. 7th international conference on spectroscopic ellipsometry (ICSE-7), June 06-10, conference program and abstracts. Berlin: 2016.

Local conferences

1. A. Paulauskas, V. Vaičikauskas, Paviršinių plazmonų rezonansinės kreivės kitimas vykstant gyvsidabrio adsorbcijai Doktorantų mokslinė konferencija, FizTech Vilnius 2014.
2. A. Paulauskas, V. Vaičikauskas, Dujų jutikliai: gyvsidabrio garų detekcija paviršiniais plazmonais bei anglies izotopų (12C ir 13C) santykio detekcija IR sugerties spektroskopija, Doktorantų ir jaunųjų mokslininkų konferencija, FizTech Vilnius 2015.
3. A. Paulauskas, I. Balevičiūtė, C. Karam, S. Tumėnas, M. Bechelany, L. Mikoliūnaitė, P. Miele, A. Ramanavičienė, A. Ramanavičius, Z. Balevičius, Sferiškai išsidėsčiusių nano gijų optinio atsako analizė panaudojant spektrinės elipsometrijos metodą Doktorantų ir jaunųjų mokslininkų konferencija, FizTech Vilnius 2016.

Acknowledgements

Throughout the writing of this dissertation, I have received a great deal of support and assistance. I would like to thank Center for Physical Science and Technology, its director prof. habil. dr. Gintaras Valušis, head of Material Science and Electrical Engineering Department prof. habil. Dr. Saulius Balevičius. In addition, I am thankful to initial supervisor dr. Viktoras Vaičikauskas for this opportunity to work on this thesis and introducing me to an interesting and highly relevant scientific field of plasmonics.

I am indebted to my supervisor prof. dr. Zigmas Balevičius for knowledge and experimental expertise sharing, guidance, suggestions, encouragement, fruitful discussions and all-round support.

I would like to thank dr. Virginijus Bukauskas, dr. Algirdas Selskis, dr. Tomas Tolenis, Audrius Valavičius, dr. Mikhael Bechelany and dr. Andrius Urba for collaborative work in sample preparation and structural properties analysis. Their much appreciated and insightful input had a tremendous impact on the quality and completeness of this thesis.

I am grateful to dr. Arūnas Ramanavičius, dr. Saulius Tumėnas, dr. Ieva Plikusienė and other colleagues from Center of physical science and technology for guiding advises and friendly working environment. In addition, I am thankful to Raimundas Skipitis for engineering solutions that were required for some of the experiments.

In addition, I would like to thank my parents and wife Jurgita for continuous love and support. Finally, I would like to thank my high school physics teacher Ona Greviškytė for inspiring me to pursue physical sciences.

1. LITERATURE REVIEW

1.1. Ellipsometry

Ellipsometry is sensitive optical measuring method for study of thin films. Ellipsometry measure changes the state of light polarization upon reflection from the sample surface. This method was proposed in the late 19th century by Paul Drude [16]. Since this time ellipsometry was continuously developed and with progress in semiconductor electronics, where ellipsometry had an important contribution, which had a crucial impact to computer progress and as a result give possibilities to use automated spectroscopic ellipsometers which made ellipsometry much more powerful and attractive analytical tool for spectroscopic data analysis [17–19].

Ellipsometry is based on optical measurements of state of light polarization change upon reflection. The quantity measured with an ellipsometer is the ratio:

$$\rho = \frac{\chi_i}{\chi_r} \tag{1.1}$$

where $\chi_r$and $\chi_i$are complex polarization state representations for reflected and incident beams respectively [17]. In the Cartesian coordinate system where p corresponds to perpendicular and s to the parallel directions with respect to the plane of incidence, the quantityχ can be expressed by:

$$\chi = E_s/E_p \tag{1.2}$$

where E_p and E_s are complex electrical field representations for s- and p-components of electric field vector. Assuming that light is reflected from an isotropic sample the complex reflection coefficient for s- and p- polarizations become $r_p = E_{pr}/E_{pi}$ and $r_s = E_{sr}/E_{si}$. Using definitions of $\chi_r = E_{sr}/E_{pr}$and for $\chi_i = E_{si}/E_{pi}$reflected and incident beams we can expand $\rho = \chi_i/\chi_r$[17]:

$$\rho = \frac{E_{pr}E_{si}}{E_{sr}E_{pi}} = \frac{r_p}{r_s} = tan\Psi e^{i\Delta} \tag{1.3}$$

Where, so called, ellipsometric parameters Ψ and Δ represents the change in amplitude and phase of light wave upon reflected from the sample surface. Furthermore:

$$tan\Psi = \frac{|r_p|}{|r_s|}, \tag{1.4a}$$

$$\Delta = \delta_{rp} - \delta_{rs} \tag{1.4a}$$

, here δ_{rp} is the phase of p polarization reflection, δ_{sp} phase of s polarization reflection. Because ellipsometric parameters are acquired from: $\Psi = tan^{-1}|\rho|$ and $\Delta = arg(\rho)$ its values are restricted to $0º < \Psi < 90º$, $-180º \leq \Delta \leq 180º$ or $0º \leq \Delta \leq 360º$. Furthermore Ψ and Δ are polarization ellipse parameters that describe polarization change upon interaction thus reflection variation for s and p polarizations is measured as the changes of polarization state. The biggest difference between r_p and r_s is at Brewster's angle and is defined as the angle of incidence at which r_p is equal to zero. For a given refractive indexes of both mediums n_1 and n_2 Brewster's angle is determined as:

$$\theta_B = arctan\left(\frac{n_2}{n_1}\right) \tag{1.5}$$

Incidence angles close to Brewster's angle are preferred for ellipsometric measurements because they produce the biggest difference between p- and s-polarizations.

1.2. Optical models and data analysis

The electromagnetic wave is fully characterized when we can describe the amplitude and phase of the wave at any time in a free space. As noted above ellipsometric parameters Ψ and Δ represents amplitude and phase of reflected wave which is measured at the same time and it is the main advantage of ellipsometry compared with spectrophotometric optical measurements where intensity of light is registered, and amplitude and phase of the light wave are not separated. However, as all optical methods, ellipsometry is an indirect technique, thus regression procedure is needed to transform measured ellipsometric parameters Ψ and Δ into physical quantities such as optical dispersion of complex dielectric function and the thicknesses of the studied thin films. There are few edge cases where the analytical approach is sufficient for evaluation of complex dielectric function. In the case when ellipsometric measurements are performed at the boundary of bulk unknown medium with the air. Then the dielectric function ϵ_m of the medium can be calculated by:

$$\epsilon_m = sin^2\theta_i \left[1 + tan^2\theta_i \left(\frac{1-\rho}{1+\rho}\right)^2\right] \quad (1.6)$$

here θ_i is the angle of incidence and $\rho = r_p/r_s$. For more complex structures analytical formulae cannot be derived thus regression analysis should be employed.

Data analysis procedure can be split into several steps depicted in Fig. 1.1 [20]. Firstly, the optical model should be created that describes the sample structure. Layers with their thicknesses and dielectric constants are selected. This model should represent the physical properties of the structure. If the optical constants of a layer are not known the dispersion of optical constants can be modeled by using model dielectric function (MDF). In this way a parametrization is performed, and the optical properties are expressed as a set of parameters in the chosen function. Selection of the model dielectric function depends on the physical properties of the layer. For example, for metals Drude's model is usually used. If layer is a dielectric and has no absorption bands in the visible range Cauchy model is preferred. After the optical model creation ellipsometric parameters Ψ_m and Δ_m can be generated and compared with experimental data. By choosing the model fit parameters discrepancy between experimental and generated data is obtained. The regression procedure is performed by using iterative non-linear regression (e.g. Levenberg–Marquardt method) and the difference between measured and generated spectra is minimized. Incremental changes of selected parameters are made which result in generated ellipsometric spectra change. After fitting procedure is done, we must weigh fitting results. For this "goodness" of the fit between experimental and generated data must be estimated. Most commonly mean square error (MSE) is used. Values close to 1 is regarded as successfully good even though higher values (in the order of 10) can be accepted as sufficiently good. It is common to stumble upon a local minimum when fitting. At this point consecutive iterations of fitting will not produce better results even though the fit is far from ideal. In this case we need to change starting values of fitted parameters and start the fitting procedure again. When we are satisfied with the fit physical parameters can be extracted.

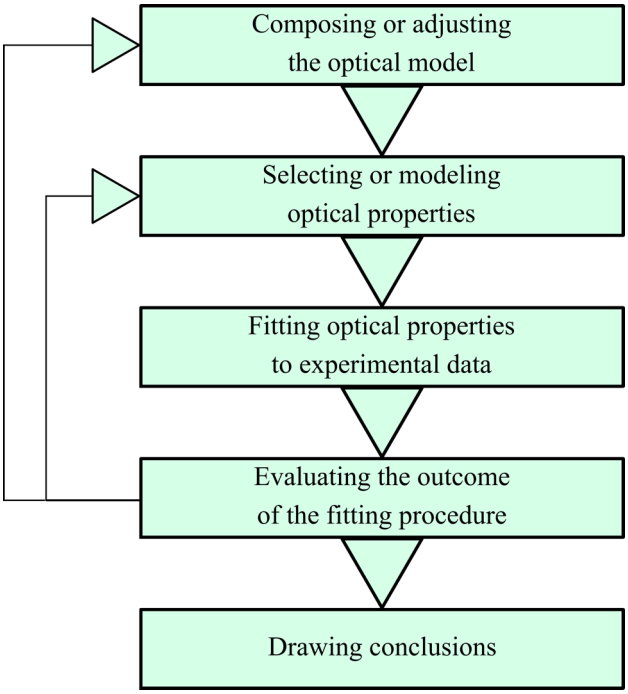

Figure 1.1. Data analysis procedure in spectroscopic ellipsometry

1.3 Internal reflection ellipsometry

In most applications such as thin films analysis, simple bulk samples or complex nanostructures ellipsometry is operated in external (conventional) configuration. However, in the external configuration signal-to-noise ratio increases when light propagates through liquids or opaque medium in which adsorption processes occur. Making the external reflection configuration complicated for studies of the surface adsorption process. This can be overcome by sample investigation in the internal reflection ellipsometry (IRE) configuration where light does not propagate directly through the adsorbing medium together with cuvette for liquids handling. The application of a glass prism as an optical element to obtain attenuated total internal reflection gives a possibility to study various processes on the base of the prism surface without the light beam passing through the liquid medium where adsorption occurs. However, only several publications [12,13] have been dedicated for studies of bio-adsorption processes on dielectric surfaces in the internal reflection ellipsometry. It was shown that thickness of thin films can be measured with descent precision when an additional high refractive index

layer is inserted on the base of prism [12]. Soichi et al. used tantalum oxide on a silica substrate with an additional thin silica layer on the top of Ta_2O. Enhancement of ellipsometric optical response due to multiple reflections inside the additional dielectric surface layer with the high refractive index has been reported [14,15,21].

1.4. Total internal reflection.

Total internal reflection (TIR) is an internal reflection configuration when the angle of incidence is larger than a particular critical angle θ_c. The critical angle can be calculated from Snell's law $n_i sin\theta_i = n_t sin\theta_t$. When electromagnetic radiation is illuminated at a critical angle the refracted angle θ_t is equal to 90º, then critical angle can be expressed as:

$$\theta_c = \theta_i = arcsin\left(\frac{n_t}{n_i}\right) \tag{1.7}$$

This angle depends on the refractive indexes of boundary mediums and exist only in the case when the light propagates from the medium with a higher refractive index (n_t) to the medium with a lower index of refraction (n_i). This means that the transmission beam travels along the surface of the boundary. For angles larger than the critical angle, Snell's law will not give real solutions because n_t is larger than 1 and become complex valued. Thus, no energy is transmitted, and everything is reflected for all light polarizations. However, a portion of the light wave penetrates into a medium with a lower index of refraction due to evanescent field that is localized at the interface of the boundary.

Even though everything is reflected in TIR configuration from the boundary conditions tangential components of electric field must be equal at the interface of two media. Thus, electric field penetrate into the second medium even though there is no energy transfer into the second medium. This means that incidence beam cannot abruptly change direction of propagation and direction should change gradually (see Fig 1.2). In other words, the beam penetrates into the second medium and after changing its direction of propagation at the penetration depth and have a lateral shift, due to evanescent wave excitation. This lateral shift is called Goos-Hänchen's shift [22]. This interference between incident and reflected electromagnetic fields result in a surface electromagnetic wave that is bound to the surface with exponential attenuation away from the interface. Transmitted electrical field's attenuation is exponential in a normal to the surface boundary direction [10]:

$$E_T(x,z,t) = e^{\frac{-z}{d_z}} e^{i\omega t - i\frac{2\pi n_o}{\lambda} x sin\theta_i} \quad (1.8)$$

here d_z is a constant describing the decay of an electrical field in z direction (penetration depth). For glass/air interface with n_{Glass} = 1.5 and n_{air} = 1 at λ = 633 nm and θ_i = 60º electrical field penetration depth is 122 nm. However, usually the intensity measurements were performed in real experiments:

$$I_T \propto E_T^2 \quad (1.9)$$

Hence the intensity probing depth into sensing medium is expressed as:

$$d_{Iz} = \frac{d_{Ez}}{2} \quad (1.10)$$

That is why, for the previously described mediums, probing depth is 61 nm [23].

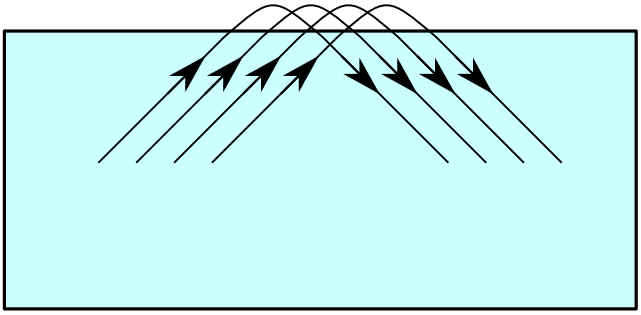

Figure 1.2. Electromagnetic field penetration into second media and reflected beam lateral shift upon reflection.

From (1.8) it can be seen that electrical field propagates along the surface in x direction. This corresponds to an energy flow in the second medium (optically less dense) within the bounds of penetration depth along the boundary surface. So, the tangential component of Poynting's vector is non zero even if it does not have a normal component along the surface. This energy flow can be used to couple energy to various surface polaritons excitations in thin metal films. In addition, TIR configuration also have been used for surface electromagnetic waves excitation in photonic crystal [21,24].

1.5. Surface plasmon resonance

Surface plasmon resonance (SPR) is an electromagnetic surface wave phenomenon that is caused by collective valence electron oscillation. This surface wave is generated at the interface of a good metal (e.g. Au, Ag) and a

dielectric. There are several SPR generation configurations but due to practical reasons Kretschmann configuration is the most popular. In this configuration resonance conditions depends on illumination wavelength, incident angle, dielectric and metal optical constants. By changing dielectric layers optical properties optimal resonance conditions changes too. This property is widely used in sensory applications.

1.5.1 Volume plasmons

In Drude model that describe free electrons in metals as a plasma of electrons in which each electron can freely move from one atom to another [25] dielectric function is expressed as:

$$\epsilon(\omega) = 1 - \frac{\omega_p^2}{\omega^2 + i\Gamma\omega} = 1 - \frac{\omega_p^2}{\omega^2 + \Gamma^2} + i\frac{\omega_p^2\Gamma}{\omega(\omega^2 + \Gamma^2)} \quad (1.11)$$

, here Γ – damping constant, ω_p - Drude plasma frequency expressed as $\omega_p = \sqrt{\frac{e^2 N_e}{\epsilon_o m_e}}$ with e – electron charge, N_e – number of electrons per volume unit, m_e – electron mass and ϵ_0 – vacuum dielectric function. When damping constant is small, $\epsilon(\omega_p)$ approaches 0, collective longitudinal optical (LO) modes can propagate. In visible range these longitudinal modes are called volume or "bulk" plasmons. First LO modes generation were performed employing electron energy loss spectroscopy (EELS) by Ferrell [26] and theoretically described by Ritchie [27]. Several years later McAlister and Stern [28] showed that LO modes can be exited in very thin films by light illumination of p-polarization at oblique angles. This normal to the surface excitation manifests as an absorption band in reflection and transmission measurements.

1.5.2 Surface plasmons polaritons

Previously briefly described volume plasmons are radiative modes that can be generated by fast electrons or by photons at an oblique angle. Because LO modes are radiative, they can decay by spontaneous photon emission in addition to collisional damping. In a situation when the wave vector of the plasmon and photon match a coupling can occur and collective excitation can exist. This photon and plasmon coupling is called plasmon polariton (PP) [29]. If the photon is decoupled, then the plasmon is dissipated. This can occur in materials where ϵ^i is negative and in turn electromagnetic wave propagation is forbidden. These conditions are met for metals below plasma frequency.

However, surface plasmons that are constrained at the boundary metal and dielectric interface can couple to photons. This coupled propagation is termed surface plasmon polariton (SPP). Sometimes the word “polariton” is omitted in literature when referring to SPP even though polaritonic nature of surface plasmon is implied.

Specific conditions must be met so that surface plasmons could couple with irradiated light. In principle all energy from light can be transferred into SPP at resonance. This resonance presents itself as a dip in reflection spectra and is called surface plasmon resonance (SPR). Angular and spectral position and shape of the resonance strongly depends on the refractive indexes of the boundary mediums at the interface. This phenomenon is widely used in bio-sensing and in the thin layer science due to the fact that only a thin layer has an impact on the SPR. The probed depth is of the same order as the penetration depth of the evanescent field.

1.5.3 Surface plasmons polaritons dispersion

Theoretical description of surface plasmons is analogous to similar quasiparticles analysis, such as phonons, magnons or excitons. Full derivation of surface plasmon polariton dispersion can be achieved by using Maxwell Equations with appropriate boundary conditions [30]. Due to the fact that surface plasmons are generated at the boundary of two media a continuity of electromagnetic field at the interface must be met. Same boundary conditions hold for Fresnel reflection coefficients. Thus, a solution of wave propagation along the semi-infinite surface can be found starting from Fresnel reflection coefficients.

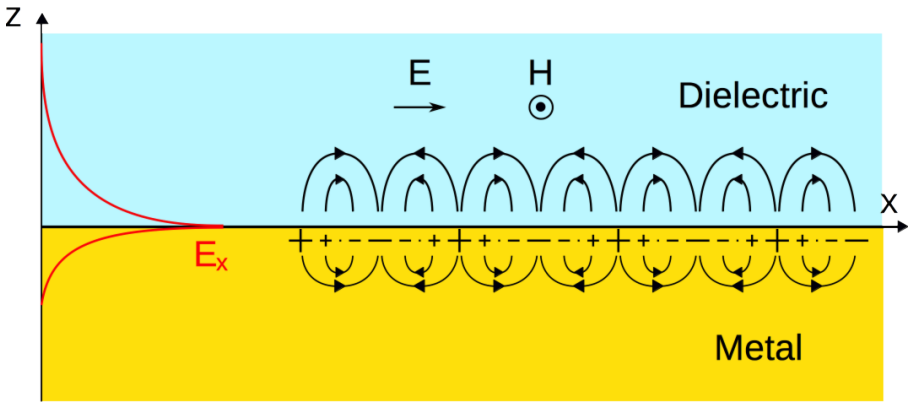

Figure 1.3. Electric charge and electromagnetic field distribution for SPP excitation at metal/dielectric interface.

During the coupled excitation of surface plasmon polaritons electric dipoles are created by collective oscillation of valence electrons (See Fig. 1.3). This continuous electron redistribution generates an electromagnetic field normal to the boundary surface. Because s-polarization is always parallel to the incidence surface only p-polarization can couple to SPP. At resonance when $r_p = 0$ Fresnel reflection coefficient for p-polarisation can be expressed as [31]:

$$\frac{k_{z,m}}{\epsilon_m} + \frac{k_{z,a}}{\epsilon_a} = 0 \qquad (1.12)$$

here k_z is a wave vector in the z direction, subscripts `m` and `a` denotes metal and ambient media. One of the possible solutions is when electric functions have opposite signs. This can occur if $\varepsilon_a > 0$ and ε_m real part (ε'_m) is negative. The later can be achieved for dielectric and the former for metals εμ below plasma frequency. Combining (1.12) with $k = \frac{\omega}{c}\sqrt{\varepsilon\mu}$ we get surface:

$$k_{SP}^{\infty} = \frac{\omega}{c}\sqrt{\frac{\epsilon_a\epsilon_m}{\epsilon_a+\epsilon_m}}; \qquad (1.13)$$

plasmon polariton dispersion for semi-infinite surface along the boundary:
Relation 1.13 is depicted in Fig. 1.4 from here we can see that for all photon energies light wave vector is larger than SPP wave vector. Thus, we cannot couple surface plasmon polaritons by direct boundary illumination.

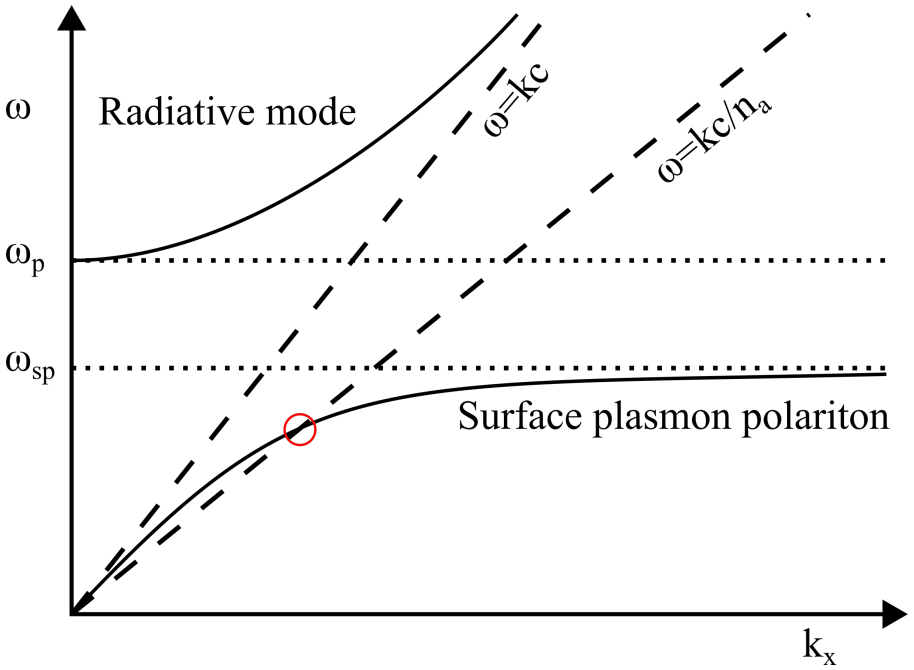

Figure 1.4. Surface plasmon polariton dispersion. Dashed lines indicate light line in air and in a dielectric medium with refractive index n_a. SPP excitation conditions are denoted by circled intersection of light line and SPP dispersion curves. Here: ω_p- plasma frequency, ω_{sp}- surface plasmon frequency, k_x- parallel to the surface component of wave vector.

Surface plasmon polaritons cannot be exited on a smooth metal surface by direct illumination because wave vector at every incidence angle for surface plasmon and incident light is mismatched. To circumvent this a glass prism can be used in a Kretschmann configuration. In this configuration a thin metal film is deposited on the base of the prism. For practical reasons, metal film is deposited on a thin glass substrate with the same refractive index as the prism. A refractive index matching liquid is used to bind prism and the substrate slide together. This way samples can be easily changed by swapping glass substrates with deposited thin metal films.

Thickness of the metal film must be appropriately selected so that a photon passing through the prism could penetrate the thin layer of metal via tunneling. Besides the film cannot be too thin and differs for various metals, for example optimal thickness for gold is 50 nm and for silver the optimal thickness is around 45 nanometers [25].

Tunneling through the thin metal film can only be achieved in the event of a total internal reflection. This happens when the incidence angle θ_a is greater than the critical angle. As mentioned before when total internal reflection occur an evanescent field is created. This field can couple to the surface plasmon on the other side of the metal film. Besides by changing the incidence angle we can tune the module of the wave vector:

$$k_{xa}^{light} = \frac{\omega}{c}\sqrt{\varepsilon\mu}sin(\theta_a); \qquad (1.14)$$

So, in this configuration surface plasmon resonance depends on all three media's refractive indexes: prism (glass), thin metal film and dielectric. In addition to requirements for optical constants and thickness of metal film the incidence angle has an optimal value too. From (1.14) we can see that wavelength of the incidence light is also a parameter that has to be tuned. If the dielectric media's refractive index changes optimal incidence angle and wavelength for the resonance condition changes too. By observing incidence angle or location of SPR dip in specter we can conclude how much dielectric media's refractive index changed. This is the main phenomenon used for bio-sensing and thin film analysis.

1.5.4. Photonic crystals

First relevant research dates back to 1887 years [32] when Lord Rayleigh examined wave propagation in a periodic structure. In his study stop band phenomenon was described and forbidden gap's edges position were expressed as a function of modulation period and relative density modulation. It was also mentioned that his ideas could be applied to light propagation through a periodic silver structure produced in a photographic medium. Besides total reflection could be achieved even with slight density modulation if the structure is infinite.

Later, in year 1913, collaborative research by William Henry Bragg and his son Lawrence Bragg described phenomenon that is currently known as Bragg diffraction of X-ray radiation by crystalline solids. They found that specific x-ray radiation wavelengths and angles produces intense peaks of reflected radiation in crystals. In order to explain this phenomenon crystalline solids were modeled as parallel planes with a fixed distance d between them. When phase shift, between reflections of different planes, is 2π a constructive interference occurs, and reflection peaks can be observed. This condition is called Bragg's law and is a simple yet powerful tool for studying crystalline structures. Independently, in 1914, C. G. Darwin proposed "dynamical theory

of X-ray diffraction" that explained reflection and transmission of X-ray in 3D crystals.

The concept of Photonic crystal (PC) was introduced by Yablonovich [33,34] in 1987 and the term was coined shortly after in 1989 and it is widely used to describe a periodic structure that affects electromagnetic field propagation. In general, periodicity can be achieved in multiple direction but for brevity discussions will revolve only around 1D photonic crystal also called Bragg gratings. When light propagates through a periodic structure, multiple reflections can occur. Similarly, to x-ray and crystal interaction, by setting appropriate propagation lengths, constructive interference of incident and reflected beams can occur. Multiple reflections can result in a forbidden band [34]. Periodic structure with different dielectric materials forms a photonic band gap where little to no light is transmitted through the structure for particular spectral region of wavelengths. Besides light is not absorbed in dielectric mediums upon constructive interference. To stress the reflective nature of the transmission decrease, this structure can be called Bragg mirror.

Because PC crystal is a spatially ordered element, its response for irradiated light depends not only on the structure but on the illumination angle and wavelength. By changing incidence angle Bragg's condition changes and the spectral position of the photonic stop band shifts. This property allows wavelength position tuning via angle change. Not only position, but its form can be tuned. Bigger contrast in refractive index and number of alternating layers results in a narrower band gap.

Photonic crystals can be formed naturally or synthetically. There is a wide range of naturally formed PC structures in pearls, opals or bird feathers, fish scales, inner shell of molluscs, beetle exoskeletons and butterfly wings of specific species [35–40]. Besides some reptiles and amphibians combine several chromophores, including natural PC structures iridophores [41]. In fact, it was only recently showed that panther chameleon color change is related to PC. Through active tuning of a lattice of guanine nanocrystals observable color shift occurs [42]. As for synthetic structures, various techniques can be employed in forming 1D, 2D or even 3D Photonic crystals [43–51]. For example, 1D structures can be fabricated via various sputtering technology of thin films or atomic layer deposition. And for 2D PC photolithography can be used.

Photonic crystals are structures with periodically modulated index of refraction on the scale of the wavelength of light. In the PC case, solution for Maxwell's equations have the form of the Bloch function, which is different from the uniform media case with the same effective refractive index where

plane waves approximation is used. Namely, periodic modulation of refractive index results in the photonic band gap formation in the reflection or transmission spectra. When PC is bounded with another PC or a layer with a negative dielectric function (noble metals for example) propagating surface modes (surface waves) and non-propagating surface states (standing waves) can be excited at the interface between PC and metal layer.

1.5.5. Tamm plasmon polaritons

Much attention has been given during the last decade to structures with covered thin metal layers placed on the top of the PC's. Nearly hundred years ago Igor Tamm described surface bound electron states in a periodic structure [52]. Analogous surface states can be observed in the optical range of electromagnetic radiation called optical Tamm state [53]. Tamm states can be realized at a boundary of two different periodic structures [53] or using metallic film atop of 1D photonic crystal [54]. In the latter case Tamm states are called Tamm plasmons due to resemblance to conventional surface plasmons. Although there are similarities with conventional surface plasmons, the differences in excitation and dispersion curves for Tamm plasmons, compared to surface plasmons, can be advantageous in real-life applications like optical sensing.

Theoretical Tamm state generation first time proposed by Kavokin et al. using a pair of two different multilayered dielectric structures [53]. Shortly after Katileevski suggested that optical Tamm plasmons should be obsered using a periodic structure and a metal film [55]. Their research predicted position and dispersion curve of Tamm plasmon for a quarter wave GaAs/AlAs Bragg reflector.

The Tamm plasmon-polariton (TPP) appears at the boundary between the photonic crystal and the metal layer [55,56]. Tamm plasmon-polaritons are optical states that can occur in the energy band gap on a photonic crystal surface. The stop band of the PC resembles the energy band gap due to Bragg reflections in its periodic structure. In contrast to the SPP propagated surface electromagnetic waves, the TPP are non-propagating states and can be excited in both their TM and TE polarizations (because of the PC) similar to the Bloch surface wave (BSW). In fact, the TPP is a standing wave, which is an interference phenomenon created by two surface waves propagating in opposite directions [56]. The TPPs have an in-plane wave vector, which is smaller than the wave vector of light in a vacuum, which allows for their direct optical excitation. For the SPPs, this total internal reflection condition can be

achieved only when the incident light reaches an in-plane wave vector equal to the surface plasmon resonance [54,57].

Recently, there has been a large interest in the Tamm plasmons effect application for optical sensing by using spectroscopic ellipsometry [58], the perfect absorption due to optical Tamm states accompanied by a singular behavior of the phase revealed the improved sensitivity of optical sensors [59]. Refractive index sensor concept applying optical Tamm states were proposed by Zhang *et al.* [59].The mesoporous distributed Bragg reflectors were applied for generation of Tamm plasmons and sensing of analyte which can diffuse in to the PC from mesoporous layers [60]. Several publications have been mostly dedicated to numerical studies of the hybrid TPP-SPP mode in optical sensing applications when changing the refractive index of the ambient [61] or the optical magnetic field enhancement due to Tamm plasmons [62]. The features of the optical dispersion of the hybrid TPP-SPP mode have also been studied for possible designs of refractometric sensors which vary the refractive indexes of the dielectric ambient [61]. The hybrid TPP-SPP modes have also been experimentally generated in metal/semiconductor microstructures by exciting the TPP by the photoluminescence of quantum dots [63].

The hybrid plasmonic excitations arise when such photonics structures with thin metal layers are attached to the prism. It has been shown [64] that both the TPP and the SPP modes can coexist on the same metal layer if suitable conditions (metal layer thickness and angle of incidence) for both excitations are satisfied and the coupling of these excitations results in the hybrid TPP-SPP mode. For TM polarized incoming light, both the TPP and the SPP are excited at different interfaces of the same metal layer, thus revealing the repulsive nature of these two resonances [64]. The hybrid TPP and the SPP modes can be excited by using a glass prism with a PC/gold layer structure attached to its base. At an appropriate angle of incidence (AOI) to the prism, both resonances can be excited, the TPP due to the Bloch waves in the PC and when the matching of the SPP in-plane wave vector is achieved through the prism coupler. The excitation of both the TM and the TE polarizations can be obtained by employing the spectroscopic ellipsometry technique in its total internal reflection geometry (TIRE) [65]. For the study of these hybrid excitations, TIRE method has several important advantages such analytical power of spectroscopic ellipsometry which allows detail analysis of changes of the state of light polarizations and simultaneous excitation of hybrid TPP-SPP modes.

1.6 Total Internal Reflection Ellipsometry

The application of ellipsometric method under conditions of total internal reflection firstly was proposed by Abeles [66]. Later the methodology has been called surface plasmon resonance enhanced ellipsometry [67], total internal reflection ellipsometry [68], surface plasmon resonance ellipsometry [69]. Structures under investigations without metal layers (without SPR effect) often called internal reflection ellipsometry (IRE) [14]. However, if surface electromagnetic waves excitation is of primary interest in nanostructures with or without metal films the conditions of total internal reflection should be fulfilled. Therefore, TIRE involved broad definition, not only related with SPR effect, and generally describe the excitations of surface electromagnetic waves on dielectric and/or metallic nanostructures under conditions of total internal reflection. The glass prism, as a coupler, plays an important role in TIRE method, because it allows to excite non-radiative modes of various type of surface electromagnetic waves depending on the nanostructure.

TIRE is an advanced optical technique, which, usually, combines spectroscopic ellipsometry and SPR. The sensitivity of this method is higher than conventional ellipsometry or SPR [11] used separately. In fact, TIRE utilizes the analytical power of ellipsometry and increases its sensitivity by introducing the SPR effect into the optical scheme of the ellipsometer. This increased sensitivity of TIRE enables one to analyze in detail the structure and properties of such ultra-thin layers [70].

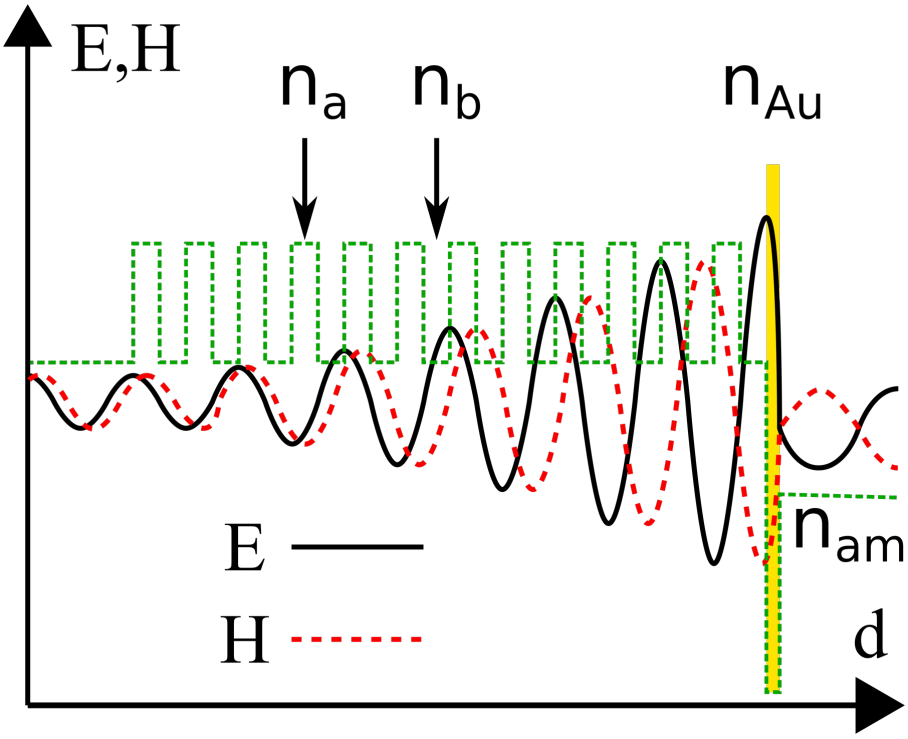

Figure 1.5. Principal representation of Tamm plasmon generation when 6 pairs of high and low refractive index mediums are used with a thin gold layer on top. Structure is illuminated from the Bragg grating's side. Here n_a and n_b- high and low refractive index materials, n_{Au} - gold refractive index, n_{am} - refractive index of ambient material.

More in depth description of TIRE can be achieved using Fresnel reflection equations [10]. In the most general case Fresnel reflection coefficients for p- and s- polarizations r_p and r_s are not equal and depends on the incidence angle and on the optical properties of the boundary mediums. In total internal reflection when the mediums are purely dielectric real parts of r_p and r_s equal to 1 with Ψ and Δ parameters expressed as [10]:

$$\Psi = 45º; \tag{1.15a}$$

$$\Delta = \delta_p - \delta_s = 2arctan\frac{\sqrt{sin^2\theta_i - sin^2\theta_c}}{sin\theta_i tan\theta_i}; \tag{1.15b}$$

Here we can see that Δ is not constant and dependent on the incidence as well

as critical angles. As previously stated, critical angle is a function of both mediums refractive index which in turn means that Δ is dependent on both mediums' properties.

1.6.1. TIRE with additional dielectric layers

Because penetration depth is in tens to hundreds of nm, we can add additional layers between two semi-infinite dielectrics. When adding additional thin dielectric layer Airy formulas can be used [10]:

$$r_{012p} = \frac{r_{01p}+r_{12p}e^{i2\beta}}{1+r_{01p}r_{12p}e^{i2\beta}}; \quad (1.16)$$

$$r_{012s} = \frac{r_{01s}+r_{12s}e^{i2\beta}}{1+r_{01s}r_{12s}e^{i2\beta}}; \quad (1.17)$$

where

$$\beta = \frac{2\pi d n_1 cos\theta_1}{\lambda}; \quad (1.18)$$

where n_1 - refractive index, θ_1 - incidence angle. Here we can see that Fresnel reflection depends not only on the optical properties (n_1) but on the thickness of the dielectric film. What this means is that we either need to know the thickness or optical constants of the investigated layer. In practice if thickness is the desired parameter of the film optical constants are taken from literature [71]. On the other hand, if we want to examine optical constants the thickness of the film must be measured using another technique.

Most commonly there are several thin layers used in experiments with each layer having separated needs to be included. For example, in the ellipsometric liquid crystal (LC) measurements semi-infinite glass substrates were coated with monolayers of silane surfactant molecules to assure LC alignment in nematic phase [17]. In another research Bloch surface waves were generated in a structure based on a multiplayer of alternating TiO_2 and Al_2O_3 [72] . For these complex multilayer systems reflection calculations can be performed using 2×2 transfer matrix formalism [10].

1.6.2. TIRE with additional metal layers

Metals are highly absorbing materials in the visible range that is why thickness must be limited to several tens of nm so that the layer would be semitransparent. Most important and common function of the metal film is sensitivity enhancement with surface plasmon polaritons. As mentioned before evanescent field can be coupled with surface plasmons and joined photon/surface plasmon excitation of surface plasmon polariton can exist. The

combined technique of TIRE and surface plasmon has higher sensitivity than both sensing techniques seperately.

In TIRE configuration a thin metal film is used and SPR resonance wave vector is expressed as:

$$k_{SP} = k_{SP}^{\infty} + \Delta k_{SP}; \tag{1.19}$$

here Δk_{SP} is and added term due to the perturbation caused by the glass prism. It depends on the thickness of the metal film. Increasing the thickness of the film reduces this term and we approach the semi-infinite case. Both k_{SP}^{∞} and Δk_{SP} can be separated into real and imaginary parts.

$$k_{SP}^{\infty} = k_{SP}^{r\infty} + ik_{SP}^{i\infty}; \tag{1.20}$$

$$\Delta k_{SP} = \Delta k_{SP}^{r} + i\Delta k_{SP}^{i}; \tag{1.21}$$

here $k_{SP}^{i\infty}$ is internal and Δk_{SP}^{i} additional damping.

To better understand the combination of TIRE with SPR phenomenon a reflection for glass/metal/air system must be derived. We are only interested in p- polarization because s- polarization does not have a x-component. For p-polarization previously mentioned formula can be used:

$$r_p = \frac{r_{01p} + r_{12p}e^{i2\beta}}{1 + r_{01p}r_{12p}e^{i2\beta}} = r_{01p}\frac{1 + r_{01p}^{-1}r_{12p}e^{i2\beta}}{1 + r_{01p}r_{12p}e^{i2\beta}}; \tag{1.22}$$

After approximating close to the resonance a derived (full procedure provided by Raether [73]) p- polarization Fresnel reflection is expressed as:

$$r_{012p} = r_{01p}\frac{k_x - \left(k_{SP}^{r\infty} + \Delta k_{SP}^{r}\right) - i\left(k_{SP}^{i\infty} - \Delta k_{SP}^{i}\right)}{k_x - \left(k_{SP}^{r\infty} + \Delta k_{SP}^{r}\right) - i\left(k_{SP}^{i\infty} + \Delta k_{SP}^{i}\right)}; \tag{1.23}$$

This expression for reflectance $R = \left|r_p\right|^2$ is used in SPR methods. Resonance condition is when $k_{xa}^{light} = k_{SP}^{r\infty} + \Delta k_{SP}^{r}$. In addition, if $k_{SP}^{i\infty} = \Delta k_{SP}^{i}$ then we get $R = 0, r_p = 0$. Recalling that Δk_{SP}^{i} depends on the thickness of the thin film and it is equal to zero only for semi-infinite case, we get that $k_{SP}^{i\infty} \neq 0$. This implies the need for non-zero imaginary part of the ε_m.

For ellipsometric measurements Ψ and Δ parameters angular and spectral dependence near the SPP resonance can be derived using an expression $\rho = tan\Psi e^{i\Delta}$ that can be derived dividing (1.23) by r_s and extracting:

$$\rho = tan\Psi e^{i\Delta} = \frac{r_p}{r_s} = \frac{r_{01p}}{r_s}\frac{k_x-\left(k_{SP}^{r\infty}+\Delta k_{SP}^{r}\right)-i\left(k_{SP}^{i\infty}-\Delta k_{SP}^{i}\right)}{k_x-\left(k_{SP}^{r\infty}+\Delta k_{SP}^{r}\right)-i\left(k_{SP}^{i\infty}+\Delta k_{SP}^{i}\right)}; \quad (1.24)$$

And in turn:

$$tan\Psi = \frac{|r_{01p}|}{|r_s|}\sqrt{1-\frac{4k_{SP}^{i\infty}\Delta k_{SP}^{i}}{Q^2+\left(k_{SP}^{i\infty}+\Delta k_{SP}^{i}\right)^2}}; \quad (1.25a)$$

$$\Delta = arg\frac{r_{01p}}{r_s} + arctan\frac{2Q\Delta k_{SP}^{i}}{Q^2+\left(k_{SP}^{i\infty}+\Delta k_{SP}^{i}\right)\left(k_{SP}^{i\infty}-\Delta k_{SP}^{i}\right)}; \quad (1.25b)$$

Here $Q = k_x - \left(k_{SP}^{r\infty} + \Delta k_{SP}^{r}\right)$. For both (1.25a) and (1.25b) expression the terms r_{01p} and r_s are slowly varying functions of k_x near the resonance. Thus $tan\Psi$ is dominated by the expression under the square root and Δ is dominated by the second term of (1.25b) equation. If the metal film's thickness is adjusted to result in 0 reflectance SPR (this is the case when $k_{SP}^{i\infty} = \Delta k_{SP}^{i}$) the (1.25b) can be expressed as:

$$\Delta = arg\frac{r_{01p}}{r_s} + arctan\frac{2\Delta k_{SP}^{i}}{k_x-\left(k_{SP}^{r\infty}+\Delta k_{SP}^{r}\right)}; \quad (1.26)$$

From (1.26) it is evident that Δ is a step function around the point where $k_x = k_{SP}^{r\infty} + \Delta k_{SP}^{r}$. Maximal value for the step is equal to π but because of the impurities and surface roughness real transition is not as sharp as a step function. Nevertheless, it is still faster varying than $tan\Psi$ and that is why Δ interrogation has higher changes that is relevant in sensors application.

1.6.3. Application of nanolaminates in TIRE method

Nanolaminates are a new class of promising nanomaterials with well-tailored properties. These materials are obtained by alternating layers with an individual thickness on the nanometer scale of different materials [74]. They manifest outstanding advanced mechanical [75], electrical and optical properties which depend from the constituent materials forming these nanolaminates. Nanolaminates are a subset of periodic structures with additional non optical advantageous properties. These structures exhibit increased mechanical resistance that are useful in harsh environments like outer space. Coatings of several tens of nm could be used for steel corrosion protection [76]. Different combinations of materials provided different properties. For best long-term durability Al_2O_3 and Ta_2O_5 combination is a suitable candidate. For biocompatibility ZnO can be chosen as the top most

layer of the structure. Nanolaminate periodic structures can be used for ellipsometric signal enhancement where other electromagnetic field confinement methods are less suitable [2*].

The exploitation of the SPR phenomenon demands a semitransparent metal film (commonly gold) what in some cases are not desirable, thus dielectric substrates should be used. However, the application of a glass prism as the optical element to obtain internal reflection provides the possibility of studying surface modification or biomolecule immobilization processes without the light beam passing through the liquid medium where these processes occur. However, only several publications have been dedicated to studies of dielectric thin films in internal reflection modes [12]. An enhancement of the ellipsometric optical response due to multiple reflection inside the additional dielectric tantalum oxide surface layer with a high refractive index in internal reflection configurations has been reported [13–15] .

Zinc Oxide is a prospective material for applications in optical coatings, gas and bio sensing. It is a wide band gap (around 3.3eV), n-type semiconductor with high exciton binding energy of 0.6 eV. Strong luminescent bands in UV and VIS range are present due to near band and defect level emissions, accordingly. ZnO optical properties can be tuned by changing fabricated layer's structure. The fact that ZnO is a chemically stable and bio-compatible renders it as a promising material for optical coatings and biosensing. ZnO layer can be incorporated in a nanolaminate where the surface of this type of structures resilience to ultraviolet radiation and high energy particles is attractive in aerospace. Besides a nanolaminate structure enables multiple reflections which in turn grants a possibility for enhancement of sensitivity in ellipsometric sensing. Several conditions must be met in order to observe this effect. Sufficient refractive index contrast is needed between bilayer materials. Furthermore, transparency in the visible range is preferred. If one of the materials is ZnO then the other Al_2O_3 is a good candidate for the second material. Besides, if thin layers are grown at low temperatures aluminum oxide is in an amorphous state [77,78].

Further ZnO thin layer properties review is done in the context of nanolaminate structure. Although most of the properties are comparable to pure non laminate configuration. For example, as noted before ZnO has strong luminescent bands in UV and VIS range even though exact wavelength position of excitonic peaks might not match.

The shape of the photoluminescence (PL) spectra provides information about the number of defects and structure. Ultraviolet PL band intensity

increases with increased bilayer thickness. Visible PL intensity does not follow this trend although this band is directly linked to the number of defects. With an increased number of defects relative VIS emission gets stronger.

This is linked to the increase of the number of defects in a volume unit when the size of the crystallite is reduced. Size of the crystallites were measured via AFM imaging and relative defect emission intensity corresponded to the thickness of the bilayer and in turn to size of the crystallite. In the same analysis [79] it was showed that crystal growth direction changes with increased ZnO thickness. By increasing the film's thickness excitonic peaks positions blue shifted.

Furthermore, PL excitonic peaks were visible only when the thickness was 10 nm [80]. Besides state of crystalline ZnO structure were reported at thicknesses of 10 nm or above [79]. In another research XRD analysis showed that even 10 nm thickness films displayed crystalline structure properties. This means that excitonic emission is directly linked to crystalline structure of ZnO. On the other hand if ZnO bilayers thickness were 2.5 nm, the zinc oxide film were fully amorphous [79] and near band gap luminescence were not observed.

Recently, there has been a large interest in the results obtained from zinc oxide (ZnO) thin films and nanolaminates and their relevant properties for use as materials for optical biosensors [81–83]. ZnO thin films and nanolaminates can be deposited using various methods [82,83]. ZnO nanolaminates are biocompatible, non-toxic and chemically stable [84]. The high isoelectric point of ZnO can also be used for the immobilization of proteins with low isoelectric points through electrostatic interactions [85]. Additionally, ZnO nanomaterials demonstrate controllable wettability, which allows the reduction of the volume of the sample, a quick response, increased sensitivity and signal-to-noise ratio of the developed biosensors [86]. Moreover, ZnO is compatible with complementary metal oxide semiconductor technology and therefore is suitable for the production of integrated circuits for devices with small integrated biosensors [81]. Thus, ZnO based multi-layered structures (nanolaminates) have been selected as substrates for optical biosensor designs in total internal reflection ellipsometry configurations.

1.7. Effective medium approximation

In some cases, there is a need to model optical properties of thin films using an average of multiple optical constants. This situation is most common for rough, structured surfaces or intermixed media. Treatment of complex, composite layer as uniform media with an averaged optical constants is called the effective medium approximation (EMA) or sometimes effective medium

theory (EMT) [87].

There are three most often used EMA theories in ellipsometry: the Lorentz-Lorenz theory, the Maxwell-Garnett theory and Bruggeman EMA. The general form of all three EMA theories can be expressed [88]:

$$\frac{\langle\epsilon\rangle-\epsilon_h}{\langle\epsilon\rangle+\gamma\epsilon_h}=\sum_j f_j\frac{\epsilon_j-\epsilon_h}{\epsilon_j+\gamma\epsilon_h}; \quad (1.27)$$

where $\langle\epsilon\rangle$ is the dielectric function of the effective medium, ϵ_h and ϵ_j are the dielectric functions for host and j-th constituent mediums, f_j – volume fraction of the j-th constituent and γ is screening and shape of the inclusion dependent factor which is equal to two for spheres. Expressions for different models are presented by changing the hosts dielectric functions value.

When the host material is vacuum or air ($\epsilon_h = 1$) we get Lorentz-Lorentz EMA. Based on Claussius-Mossotti this is the earliest EMA Theory. Its principle assumption that constituents are mixed on the atomic level makes this theory of limited usefulness. Larger scale is more desired for real life materials.

In the Maxwell-Garnett approximation the host material is the first medium ($\epsilon_h = \epsilon_1$) with the largest composition part of the material combination. Maxwell-Garnett approximation is most suitable for situations where composition percentage of inclusions are relatively low compared to the fraction of the host material. For example, this EMA theory is very useful for certain types of nanocrystals ingrained much lower than the percolation threshold.

The last EMA is called Bruggeman's approximation and host dielectric constant is equal to the effective dielectric function ($\epsilon_h = \langle\epsilon\rangle$). The fact that Bruggeman's model does not make assumptions about the host material makes this EMA approximation self-consistent. Although we do not need to know which material has the highest constituent fraction this EMA methods is most useful when there are no constituents with high constituent fraction. It was shown that this method can be used for surface roughness modeling when material was constituted out of ~50% voids and ~50% material [88].

1.8. TIRE for optical sensing application

Last two decades TIRE proved itself as an extremely sensitive [89] optical method in various applications of optical sensing. Most widely TIRE have been used for biosensing in detection of interaction between biomolecules such as proteins [90–93]. These general demonstrations of high sensitivity for

bio adsorption processes have been followed by more specific studies of Alzheimer's disease [94], immunosensor performance [91,92], drug efficiency after chemo-therapy investigations [3], low molecular weight proteins detection [11,95], polymer brushes growth on the top of the gold surface [96]. The imaging TIRE for biomedical applications has been applied for antibody screening [97], various biological markers detection [98] and virus recognitions [99]. Also TIRE method was used for gas adsorption studies such as nitrogen [100–102]. They noticed that changes in Δ was much slower in polar gases compared with non-polar gases whereas it only affects the bulk refractive index. TIRE was applied for detection and analysis of mercury vapor adsorption on the top of the gold and amalgam formation [1*]. It was shown that Bruggeman EMA reasonably well describe the formed amalgam surface structures on the gold surface. The hybrid Tamm plasmon – surface plasmon polaritons mode was generated by using TIRE method and penetration of mercury atoms into the gold layer with amalgam formation were revealed through the decrease of repulsion effect of two coupled resonances [3*]. Some works demonstrates the increased sensitivity of ellipsometric parameters (especially in Δ parameter) of TIRE method without metal layer (without SPR effect) [7,103] [2*]. Some applications of optical biosensing demands sensing surfaces without metal layers where various biomolecules attached to the dielectric surfaces such as titanium oxide (TiO_2) or Zinc oxide (ZnO) or others which are biocompatible materials. All these applications proven that TIRE method is rather universal, sensitive enough and can be used for studies in various fields of sciences to produce possibilities of constructing optical sensing platforms with advanced features.

2. METHODS AND MATERIALS

2.1. Equipment

2.1.1. Ellipsometers

In order to perform TIRE measurements, the basic experimental setup should consist from an ellipsometer and a prism with attached sample. The components in TIRE setup can vary widely depending on the application of interest. For real sensors approach the system should be simple in design with minimum optical elements that are required for a particular application. In the case when sensors platform is in research and development stage more sophisticated configurations of prism/sample, ellipsometers, adsorption chambers, flow systems, etc. can offer advanced measurement possibilities. The most specific component for the TIRE method is a prism and sample attached to its base. The geometry of the prisms and type of glass determine the application possibilities in particular case of approach. BK7 is a widely used glass [69,104–106] but other types of glasses also are used. For example, when studies are performed in the air or gas ambient the 45° prism is used when SPR effect is utilized. In the case of protein adsorption studies where ambient medium is aqueous the higher angles of prisms (60-70 deg.) are used for generation of SPR effect. When TIRE method is used without metal layers, the angle of incidence of light should be higher than the critical angle in order to achieve better sensitivity in the ellipsometric parameter Δ. However, one should then take refraction and polarization changes of the incident and transmitted light at the two prism/air interfaces, because light is not incident normal to the prism surface. In order to perform multiple angle of incidence the half-cylindrical or polygonal prism can be used. Such prisms allow to avoid unwanted reflections in the triangular prism, however, design of such a prism is more difficult, at the same time it works as a cylindrical lens for the incident beam and light is focused, so pre-focusing should be performed and thickness of the glass slide should be taken into account.

In this work two ellipsometers from J. A. Woollam Co., Inc. were used. RC2 (see Fig. 2.1) is a multichannel dual rotating compensator ellipsometer with a spectral range in 210-1690 nm. By employing two rotating compensators it can measure all 16 Mueller matrix elements. The first compensator is placed with a polarizer in a polarization state generator. The second one is placed after an analyzer in a polarization state analyzer part of the ellipsometer. Wide spectral range is achieved with a dual light source of

deuterium-halogen lamp. After light interaction with the sample spectral separation in space is done via prism and subsequently detected by two CCD arrays. First array detects 790 equally spaced points of electromagnetic radiation in 210-1000 nm spectral range and the other 275 points in the range of 1000-1600 nm. Motorized angular scanning is possible between 19° and 90° angles.

M2000X (see Fig. 2.2) is a multichannel spectrometer with simultaneous 470 wavelength acquisition in the possible range of 245-1000 nm. Implemented rotating compensator technology provides accurate ellipsometric parameter acquisition with high precision and speed. Automatic angle change in the range of 20°-90°. Sample tilt adjustable manually with motorized vertical sample alignment capability.

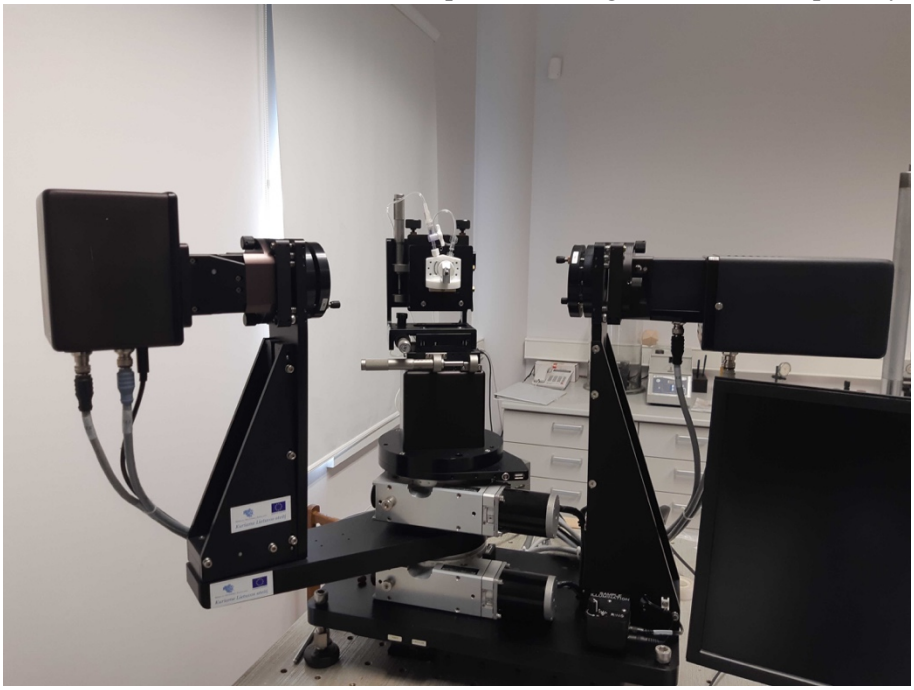

Figure 2.1. J. A. Woollam Co., Inc. RC2 ellipsometer.

Figure 2.2. J. A. Woollam Co., Inc. M2000X ellipsometer.

As mentioned before, both spectral ellipsometers were multi-wavelength. The white light of xenon or deuterium lamp incident on the sample and a multi-wavelength detector is used (grating or CCD array). Such principle of detection of optical response allows to perform whole wavelength range in one shot, what is important for fast real time measurements in various sensors applications.

2.1.2. Ellipsometric data analysis software

Motorized ellipsometer calibration, spectral and temporal data acquisition and obtained experimental data analysis were carried out using the J.A. Woollam Co., Inc. data acquisition software CompleteEase. Modeled system's optical response calculations are carried out using transfer matrix methods. For experimental data analysis, nonlinear regression is used. First, researcher has to select a model that represents the real structure as close as possible with several selected properties that can be adjusted. Then predicted model's optical spectral response is calculated and compared to the experimental data with a "goodness" of fit parameter MSE (mean square error). The process is repeated until reasonable MSE is reached or a fixed number of iterations are executed. If reasonable MSE cannot be reached initial model must be changed.

CompleteEase software is capable of temporal data regression analysis. This feature speeds up optical properties kinetics calculation.

2.1.3. Equipment for structural analysis

2.1.3.1. Atomic force microscopy

For topographic measurements Nanoscope IVa dimension 3100 atomic force microscope from Veeco was used. This device allows tapping mode and was mounted with Bruker's NCHV probe that can be used for any AFM device.

2.1.3.2. Scanning electron microscopy

The structure morphologies of the samples were examined using scanning electron microscopy (SEM). This was done using a dual-beam system Helios Nanolab 650 (FEI) equipped with an energy dispersive X-ray (EDX) spectrometer INCA X-Max (Oxford Instruments).

2.1.4. Photonic structure preparation method

An IBS coating plant from Cutting Edge Coatings GmbH was used for deposition. The apparatus was equipped with two vacuum pumps: a combination of a cryopump with a mechanical pump. Working pressure of the device is 3×10^{-3} Pa. A radio-frequency grid-system-based ion source is used to strikes at a set 57° angle. Typical parameters of the main ion source, using argon gas, are set to 1200 V = 130 mA. Coating plant is equipped with a translation stage for continuous target change and a circular rack that can rotate for substrates.

2.1.5. Hermetic chamber for sensing

In this experiment, an air tight system with a custom-built Teflon chamber was used with separate sections for the sample and for the mercury supply. These sections were connected with tubing via connecting valve that can be closed or opened to allow the mercury gas to spread to the chamber with the sample. Constant mercury vapor supply was implemented by mixing the gas using a periodic pumping mechanics (Fig. 2.3).

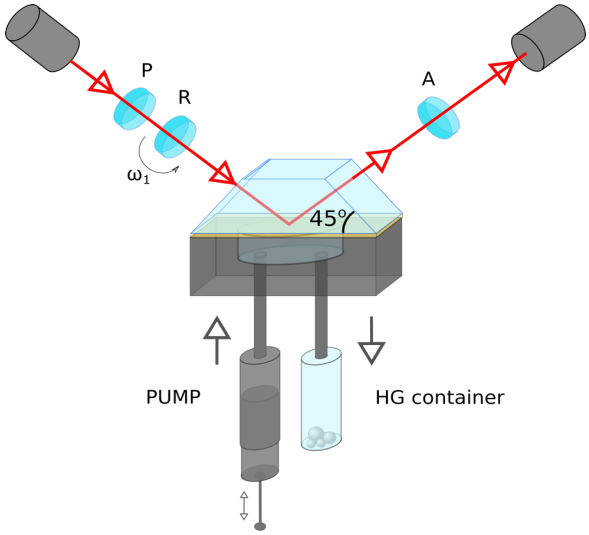

Figure 2.3. Experimental setup of TIRE measurements for mercury sorption. Here P- polarizer, R- rotating compensator, A- analyzer.

2.1.6. Bovine serum albumin adsorption

Bovine serum albumin (BSA) adsorption experiments were carried out in total internal reflection configuration with a 70° BK7 glass prism attached to the sample glass slide via optical contact using BK7 immersion liquid. BSA and buffer solutions were introduced to the functionalized surface using a custom-built Teflon chamber connected via tubing (Fig. 2.4).

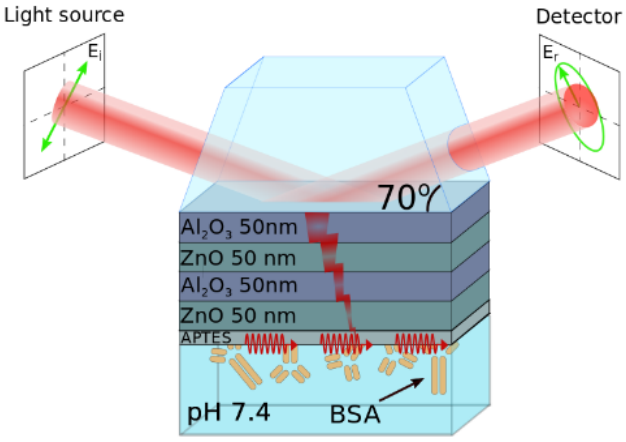

Figure 2.4. Experimental setup of TIRE measurements for BSA sorption.

2.2. Materials

2.2.1. Saturated mercury vapor adsorption

A medium sized glass vial with few mercury drops was used as a source of mercury gas. To disperse and prevent from forming larger mercury droplets a sponge was introduced into the vessel. Large number of small droplets have bigger total surface area and in turn enable faster saturated mercury gas recovery. The vial was at all times sealed with a rubber cap. In order to allow saturated mercury vapor flow to the system rubber cap was pierced with a hollow needle.

2.2.2. Nanolaminates silanization with APTES

N-(3-aminopropyl)triethoxysilane (APTES, 99%) and 1-ethyl-3-(3-diaminopropyl)carbodiimide hydrochloride (EDC) were obtained from Sigma-Aldrich (Germany). N-hydroxysuccinimide (NHS) was gotten from Merck (Germany). Bovine serum albumin (BSA, fraction V) was obtained from Carl Roth GmbH&Co (Karlsruhe, Germany). Phosphate buffered saline (PBS) tablets (0.14 M NaCl, 0.0027 M KCl, 0.01 M phosphate buffer pH 7.4) were purchased from AB Medicago (Sweden). All chemicals were of analytical grade or better. All aqueous solutions were prepared in UHQ water (conductivity less than 1 μS/cm), purified by DEMIWA rosa 5 (WATEK, Czech Republic).

The sample substrates under investigation were 1 mm thick glass plates coated with Al_2O_3/ZnO nanolaminate having total thicknesses of about 200 nm. Each Al_2O_3/ZnO (50 nm/50 nm) bilayer was approximately 100 nm thick. The Al_2O_3/ZnO nanolaminates on the glass substrates were formed using the atomic layer deposition (ALD) method. The procedure was performed in a custom-made ALD reactor at a fixed temperature of 100 ºC. Detailed deposition regimes were described in our previous publications [79,80,107].

2.2.2.1 Functionalization of the Al_2O_3/ZnO nanolaminates' surfaces

For nanolaminate application in biosensors, the design surfaces of the ZnO (the top layers of nanolaminates) were modified using (3-Aminopropyl)trimethoxysilane. Vapor phase salinization of the nanolaminates with APTES was performed according to the procedure described in [108]. To minimize the effect of humidity, the silanization was performed in a glovebox in an inert atmosphere. A few drops of APTES were deposited in a small vial, which was then placed next to the nanolaminates located in a glass Petri dish. The Petri dish was then covered and isolated from

contact with air with heat resistant insulation tape. The covered Petri dish was then placed in an oven and kept overnight at 90 °C. Afterwards, the modified nanolaminate was washed with toluene, ethanol and distilled water and dried in an oven at 110 °C. In this way, the surfaces of the Al_2O_3/ZnO nanolaminates were functionalized with amino groups, which are necessary for BSA covalent immobilization. The water contact angle on the modified and unmodified nanolaminates was measured with a KSV Instruments CAM200 optical goniometer. A drop of distilled water was placed on the surface with a micro syringe, captured with a camera 10 times and then fitted. This measurement was repeated 3 times on the same surface.

2.2.2.2 Immobilization of BSA on functionalized Al_2O_3/ZnO nanolaminates surface

In order to covalently immobilize the BSA on the salinized surfaces of the Al_2O_3/ZnO nanolaminates, the carboxyl groups of the BSA were activated using a mixture of EDC and NHS aqueous solutions for 15 min. A BSA concentration of 0.1 mg/ml was prepared in PBS, and the final concentration of EDC and NHS in the solution with the BSA was 400 mM and 100 mM, respectively. The activated BSA was exposed to the amino groups on the pre-modified Al_2O_3/ZnO nanolaminate surfaces. The covalent immobilization of the BSA on the pre-modified surfaces was registered in time using TIRE. The influence of the non-activated BSA adsorption on the registered signal was evaluated on Al_2O_3/ZnO nanolaminate surfaces before and after the surface salinization.

2.2.3. Immersion liquid

Optical contact was achieved via BK7 immersion liquid procured from Cargille laboratories. At 25° C temperature refractive index is n = 1.5167 ± 0.0005 for the 589.3 nm wavelength. Full spectral comparison with BK7 glass optical constants is shown in Fig. 2.5 [109].

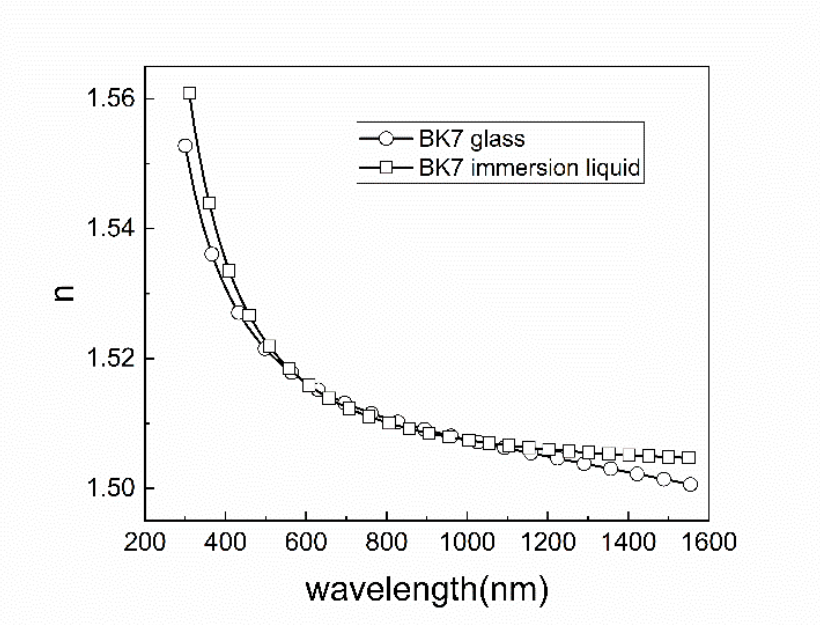

Figure 2.5. Immersion liquid refractive index dispersion comparison with BK7 glass refractive index.

2.2.4. Surface plasmon polariton sample

The single SPP samples consisted of the BK7 glass slide that was mounted on top of BK7 glass prism via optical immersion liquid and a gold layer (around 40 nm). Extra Cr layer was used between glass and gold for better Au adhesion. Coated Au layer was in a polycrystalline state.

2.2.5. TPP and hybrid TPP-SPP samples

Samples with periodic structure was coated with IBS plant. Before the deposition process, the vacuum chamber was held at 50 °C heat for 1 h. To remove the impurity layer, the ion source was used for presputtering of the target before deposition. During the process, oxygen gas was supplied toward the substrate to ensure complete oxidation of the growing coating. A radio-frequency grid-system-based ion source was used to bombard a flat metal target, consisting of high refractive index (Ti) and low refractive-index (Si) materials at a set angle of incidence of 57°. Typical deposition speeds for low and high refractive indexes were 1Å/s and 0.6Å/s, respectively. High and low index target were swapped with a linear translation stage. The substrates holding circular rack was rotated around its axis at an approximate speed of 20 rpm. Thickness of deposited material was tracked by an integrated broadband transmission optical monitoring system in the spectral range of

400–1000 nm.

Photonic crystal sample with six pairs of SiO_2/TiO_2 was fabricated beforehand for transmission measurements. For pure PC sample a PC band gap in the range of ~500 to ~700 nm is clearly visible in Fig. 2.6. After deposition of a thin 40 nm Ag layer a transmission peak was visible in an approximate place as the middle of the PC band gap center. This indicates a surface Tamm plasmon generation conditions predicted from simulations.

Consecutive Tamm plasmon polariton samples consisted of a fused silica substrate and a superlattice element of 5 bilayers with thicknesses of 130 nm/63 nm (SiO_2/TiO_2). For the single TPP, gold film of 40 nm thickness was used. The hybrid TPP-SPP samples consisted of the BK7 glass prism, five bilayers of SiO_2/TiO_2 (130 nm/63 nm) and a 40 nm gold layer.

A SEM cross section image was made for the evaluation of the layered coating thicknesses produced by ion-beam sputtering. From the Fig. 2.7, it can be seen that the PC samples have good uniformity and low roughness levels. Furthermore, SEM measured thicknesses matched thicknesses targeted during coating.

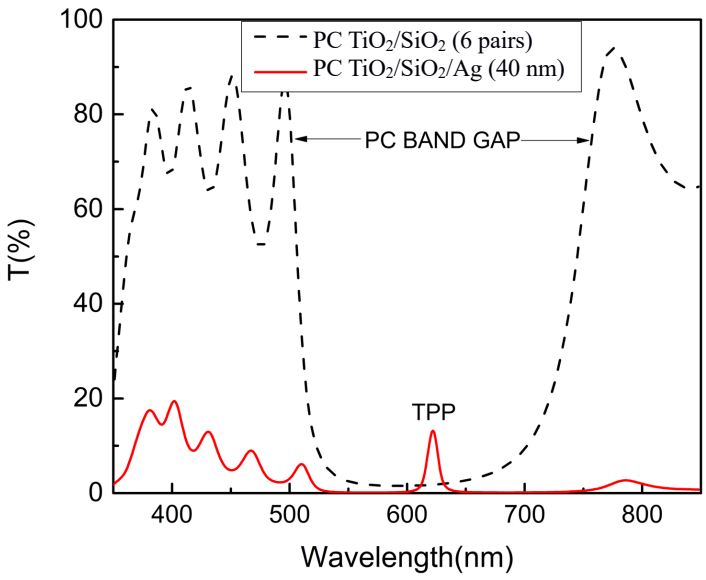

Figure 2.6. Transmission spectra for six bilayers photonic crystals with (solid red line) and without (dashed line) an additional 40 nm Ag layer on top.

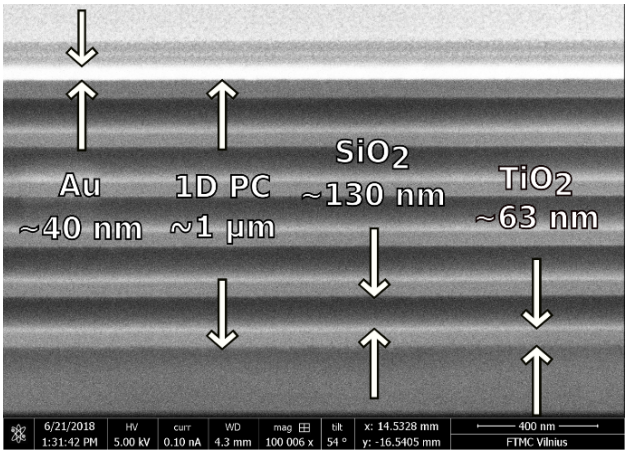

Figure. 2.7. SEM micrograph of 1D photonic crystal SiO_2/TiO_2 structure and thin (40 nm) gold layer.

2.2.6. Structural changes after mercury absorption

The surface morphology and elemental composition of the sample before (Au) and after (Au_{Hg}) mercury sorption were examined using a dual-beam system Helios Nanolab 650 (FEI), equipped with an energy dispersive X-ray (EDX) spectrometer INCA X-Max (Oxford Instruments) and a scanning probe microscope D3100, Nanoscope IVa (Veeco) (Fig. 2.8). In the first instance, the SEM images showed a smooth fine-grained pure Au layer structure with a grain size of a few tens of nanometers. After adsorption process observed on the Au layer were separated islands of surface dendrites (Fig. 2.9). What was unexpected, however, was that their characteristic contrast had disappeared in the areas that had been more affected by the electron beam. The EDX spectra contained glass substrate elements and Au peaks, but no traces of the Hg characteristic peaks.

The thickness of amalgam layer was determined from the surface topography maps of the sample (Au_{Hg}). As it can be seen from Fig. 2.8a, there were brighter areas on the surface. Moreover, the AFM phase lag in these areas showed different properties, such as the composition, adhesion, friction and viscoelasticity (not shown here). It was assumed that the brighter areas in Fig. 1a corresponded to the amalgam layer, while the darker areas were the bare gold substrate. The thickness of the layer can be evaluated from the cross section (Fig. 2.8b) marked by the dashed line in Fig. 2.8a. The step height in Fig. 2.8b was about 3.4 nm, but as the surface roughness was comparable with the layer thickness, the accuracy of this measurement was assumed to be low.

To improve this accuracy, a surface height distribution histogram was calculated from the area marked by the rectangular in Fig. 2.8. The smooth area was selected in order to avoid errors related to the surface roughness. Two peaks were detected in the height histogram (Fig. 2.8c). The position of each peak was calculated by fitting the Gaussian function. The difference between the peaks was averaged and consequently, the thickness of the amalgam layer was determined to be 3.4 nm.

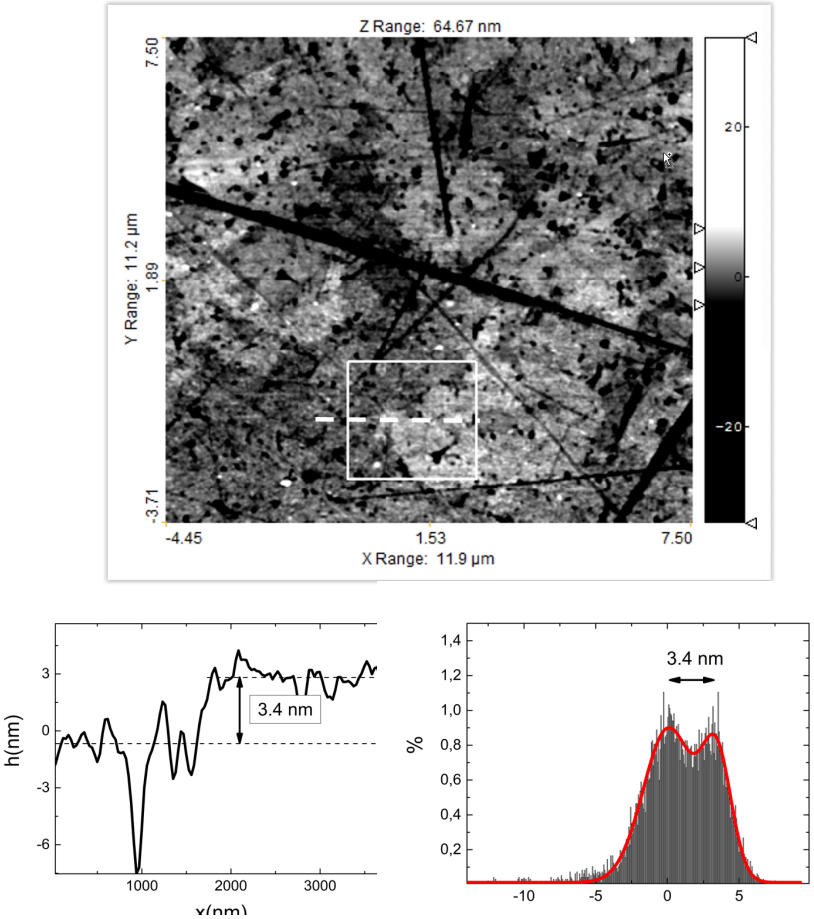

Figure 2.8. Maps of AFM surface topography a) of the sample Au_{Hg}. b) cross-section marked by dashed line in a) and height distribution histogram c) of the rectangular area marked in image a). section marked by dashed line in a) and height distribution histogram c) of the rectangular area marked in image a).

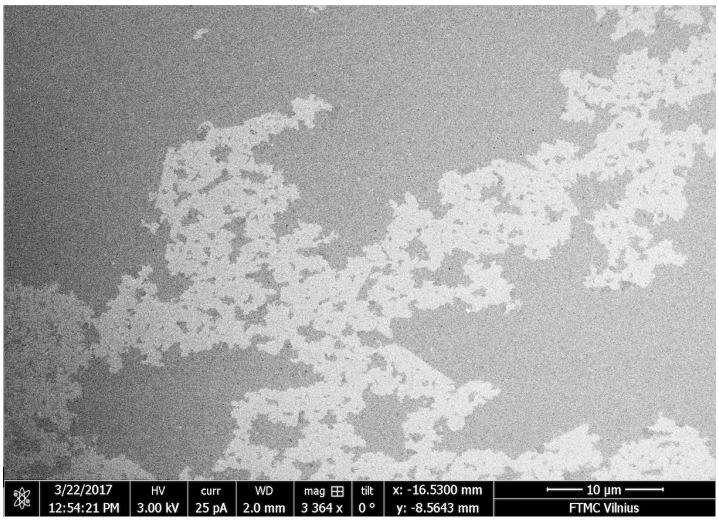

Figure 2.9. SEM micrograph of dendritic amalgam structure on the gold surface.

2.3. TIRE measurements

The ellipsometric experiments for mercury sorption onto bare SPR chip were conducted using a rotating compensator ellipsometer J.A. Woollam M2000X (Lincoln, USA). The TIRE experiments were carried out at a 45° angle of incidence with the illumination being at wavelengths in the 300 nm–1000 nm spectral range. This was conducted using a BK7 glass right angle prism connected via a refractive index matching fluid with the commercial SPR chip, which was covered with about a ~40 nm gold layer (Fig. 2.7). In this configuration, the typical surface plasmon resonance curves manifested themselves in the optical response of the ellipsometric spectra (Fig. 3.1, 3.2). The obtained experimental data was analyzed using the J.A. Woollam Co., Inc. data acquisition software CompleteEase in a multi-layer model. The system being modeled consisted of the BK7 glass, a gold layer of ~ 40 nm thickness and the surface layer of the Au/Hg amalgam. The thin (~ 2 nm) Cr layer used to get better gold adhesion between the Au and the BK7 glass was also taken into account in modeling the TIRE data. To evaluate the optical constants of the gold layer, two Lorentz and one Drude oscillators were included in the model of the gold layer. For the amalgam, an effective medium approximation surface layer composed of a mixture of gold and mercury was substituted for the Au/Hg amalgam film, which had formed

when the mercury was absorbed onto the gold. The changes of the surface roughness were also included in the fitting process of the EMA layer.

The subsequent stage of the research three types of samples were investigated. These consisted of structures supporting a single Tamm plasmon polariton (TPP), a single surface plasmon polariton (SPP) and a hybrid Tamm plasmon polariton/surface plasmon polariton (TPP-SPP). For the single TPP and the hybrid TPP-SPP, distributed Bragg gratings were formed on the tops of the substrates (SiO_2 glass), which had 5 bilayers of ~130 nm SiO_2 and ~63 nm TiO_2. These were created by ion beam sputtering. The single SPP sample consisted of only gold film having a thickness of about 40 nm, which was deposited using the magnetron sputtering technique. The single TPP and the hybrid TPP-SPP samples were also coated with gold layers of the same thickness as the SPP. All the gold layers under investigation were polycrystalline.

The spectroscopic ellipsometry (SE) experiments for TPP, SPP and SPP-TPP samples were conducted using a dual rotating compensator ellipsometer RC2 (J. A. Woollam Co., Inc.). The SE experiments were carried out in the 320 nm – 1700 nm spectral range. For the single TPP samples, a conventional ellipsometric configuration was used at an angle of incidence of 20° (Fig. 3.5). The angle of incidence (20°) was optimized in order to fulfill the excitation conditions of the TTP and to perform accurate spectroscopic ellipsometry measurements. For samples with the single SPP and with the hybrid TPP-SPP modes, experiments were conducted in a TIRE configuration using a glass BK7 prism (45°) at an AOI of 42.5° (Fig. 3.6, 3.7). The measured experimental data was then analyzed using the data acquisition software CompleteEase (J.A. Woollam Co., Inc.) in a multi-layer model. The simulated data were fitted to the experimental ellipsometric results using Levenberg-Marquardt algorithm for nonlinear regression and allowed to determine variable parameters in the model, such as thickness change during Hg adsorption, Hg concentration and depth-profile. The system analyzed consisted out of a fused silica substrate, namely, a superlattice element of 5 bilayers with thicknesses of 130 nm/63 nm (SiO_2/TiO_2). For the single TPP, gold film of 40 nm thickness was used. The single SPP samples consisted of the BK7 glass prism, a gold layer (40 nm) and a void. The hybrid TPP-SPP samples consisted of the BK7 glass prism, five bilayers of SiO_2/TiO_2 (130 nm/63 nm) and a 40 nm gold layer.

To form an amalgam surface layer, saturated mercury vapor with a concentration of 15 $\mu g/m^3$ at room temperature was introduced into the Teflon chamber [1*] containing the sensing gold layer. Ellipsometric parameters $\Psi(\lambda)$

and $\Delta(\lambda)$ were then measured in a dynamic acquisition mode at an average rate of one spectrum per 10 seconds. After the initial ~10 minutes of baseline measurements, saturated mercury gas was introduced into the sample chamber for approximately 100 minutes. Additionally, the sample with the thick (200 nm) gold layer attached to the glass substrate was incubated in the saturated mercury gas chamber for 48 hours in order to investigate the saturation of the mercury atoms into the thick gold layer. The variable angle ellipsometric spectra of the thick sample were measured after 24h and 48h. After introducing the mercury vapor, all the samples had a surface layer of the Au/Hg amalgam. The optical constants of the materials being used, namely Hg [110], BK7 [109], SiO_2 [111], Au [112] and TiO_2 [113] were taken from the literature.

The kinetics spectra of the ellipsometric parameters $\Psi(\lambda)$ and $\Delta(\lambda)$ were registered in their dynamic acquisition mode at an average rate of one measured spectrum per second. After the initial ~15 min. of baseline measurements, saturated mercury gas was introduced into the Teflon chamber containing the sensing layer until the dynamic processes settled, for mercury sorption on top bare SPR chip it was approximately 120 min. and for TPP, TPP-SPP samples it was approximately 100 min.

TIRE experiments for BSA immobilization were conducted using a rotating compensator based ellipsometer J. A. Woollam M2000X (Lincoln, USA). The TIRE experiments were carried out at a 70° angle of incidence with the illumination being at wavelengths in the 210–1000 nm spectral range. This was conducted using a BK7 glass 70° angle prism connected via a refractive index matching fluid with the glass plate being coated with the nanolaminates (Fig. 2.4). In the TIRE experiment, a liquid handling system with a custom-built Teflon chamber was used in which the nanolaminate surfaces were placed. The connecting valve was then opened, allowing the buffer solution to be injected into the chamber. This chamber was filled with PBS, pH 7.4, which was needed for the interaction of the proteins with the modified surface. The BSA solution (0.1 mg ml/l) in PBS, pH 7.4, was then injected into the Teflon chamber in order to form a thin protein layer.

The spectra of the ellipsometric parameters $\Psi(\lambda)$ and $\Delta(\lambda)$ were registered in their dynamic acquisition mode at the rate of one spectrum per second. After the initial ~15 minutes of baseline measurements the solution of BSA with the activated carboxyl groups was introduced into the Teflon chamber containing silanized Al_2O_3/ZnO nanolaminates, which contained amino groups. Ellipsometric parameters $\Psi(\lambda)$ and $\Delta(\lambda)$ in TIRE configurations have different sensitivities [114]. Ellipsometric parameter $\Delta(\lambda)$ was used for real time signal

registration because of its higher sensitivity towards surface changes during BSA immobilization. Simulations were conducted using the CompleteEASE software from J. A. Woollam Company. The ellipsometric measurements of the created optical models were conducted taking into account the methodology for the evaluation of absorbing films presented in another research study [115].

3. RESULTS

3.1 Mercury adsorption and amalgam formation studies by TIRE

3.1.1 Introduction

During the last decades, environmental pollution has had a growing influence on human health [116]. One of the most dangerous chemical elements in the atmosphere is mercury because of its long residence time and the distances that it migrates [117]. Even low levels of Hg in the atmosphere are enough to produce negative effects in human organs and immune systems [118]. The most common forms of mercury (elemental, inorganic, organic) are found in fish. This fact strongly influences the whole ecosystem and the food chains of various animals [116]. Modern industrial practices such as the combustion of coal, various technologies of plastics have long been identified as the source of mercury on a global scale [119]. All these processes are accompanied by the byproducts rich in toxic heavy metals such as mercury.

In order to assess the amount of mercury in the environment, it is necessary to develop sensitive and selective methods to determine its presence. For this purpose, gold-based surfaces are widely used as the mercury sorbent due to the strong interaction between Hg and Au. A further analysis of such surfaces is cumbersome, however, because as a further step, the gold has to be released by heating or by dissolution in various solvents and complex forming agents. Afterwards, the concentration of the gold on the surface also has to be determined using different physical methods, such as inductively coupled plasma-atomic emission spectroscopy (ICP-AES) [120,121], cold vapor atomic fluorescence spectroscopy (CVAFS) [122] or cold vapor atomic absorption spectroscopy (CVAAS) [123,124]. It was shown that CVAAS can be used for year-round monitoring of mercury in the air or precipitation[125–127]. To increase sensitivity mercury traps are used. Gold wool is the most popular trap material for elemental mercury. For gaseous oxidized mercury different trap materials should be used like quartz wool [128].

The application of these highly sophisticated methods is also limited because losses due to dissolution, the condensation of water vapor and the

spectral interference of organics, which lead to a loss in their sensitivity [129]. To avoid such limitations, other techniques such as electrical detection [130,131] and quartz crystal microbalance [132,133] are used to detect and monitor the amount of Hg on the surface of the Au layer. A comprehensive analysis of the amalgamation mechanism between the mercury and the gold was conducted using morphological methods: scanning electron microscopy (SEM), energy dispersive X-ray spectroscopy (EDX), atomic force microscopy (AFM) and the optical method of measuring fringes of equal chromatic order (FECO) [134]. They indicated that these amalgamation reactions are being formed on the surfaces of inhomogeneous films. Because of this, optical techniques have been considered unsuitable for conducting the quantitative monitoring of Hg and Au interactions.

Several publications [135–139] have been dedicated to studies of Hg adsorption onto Au film. These have used surface plasmon polariton resonance, spectroscopic ellipsometry, localized plasmons on gold nanoparticles and Raman spectroscopy. It is well known [140] that at the beginning of the process, the adsorption of mercury onto gold induces defects and island formations. After these mercury-rich islands are formed, such structures then grow to about 1μm in diameter, after which they join into pairs and form dendritic structures. Finally, these dendrites break up into threads and island structures. It has also been reported that Hg atoms diffuse more easily into polycrystalline gold than into crystalline Au (111) [141].

Such gold structures can be evaluated by total internal reflection ellipsometry (TIRE) [10]. TIRE is an advanced technique, which combines spectroscopic ellipsometry and SPR. Conventional surface plasmon polariton (SPP) optical sensors are among the most popular due to the high sensitivity which can be obtained because of the strong localization of the electric field at the metal/dielectric interfaces [142, 1*]. In SPP-type optical sensors, a glass prism as a coupler to achieve conditions of total internal reflection (TIR) is commonly used to excite the propagated SPP waves, which are transverse magnetic (TM) p-polarized. The exploitation of this SPP phenomenon requires the use of a semitransparent metal film (commonly gold or silver).

The sensitivity of TIRE method is higher than that of conventional ellipsometry or SPR [11] used separately. In fact, TIRE utilizes the analytical power of ellipsometry and increases its sensitivity by introducing the SPR effect into the optical scheme of the ellipsometer. This increased sensitivity of TIRE enables one to analyze in detail the structure and properties of such

ultra-thin layers [70]. As noted above, inhomogeneous surface structures containing mercury and gold atoms are formed during the initial phases of amalgam formation. This phenomenon, however, has not been utilized in analysis that is performed by means of commercially available SPR-based optical sensors. Some important features of such non-homogenous surface layers are therefore lost, and, as a result, the structural aspects of the investigated films cannot be completely characterized. For this purpose, an adequate optical model [143] of the structure under investigation is needed as the surface roughness and microstructure of Au/Hg films need to be taken into account in the modeling of this hybrid system.

Another type of surface mode, the so called Tamm plasmon-polariton (TPP) appears at the boundary between the photonic crystal and the metal layer [55,56]. In fact, the TPP is a standing wave, which is an interference phenomenon created by two surface waves being propagated in opposite directions [56]. The TPPs have an in-plane wave vector, which is less than the wave vector of light in vacuum, which allows for their direct optical excitation. It has been shown [64] that both the TPP and the SPP modes can coexist on the same metal layer if suitable conditions (metal layer thickness and angle of incidence) for both excitations are satisfied and the coupling of these excitations results in the hybrid TPP-SPP mode. For TM polarized incoming light, both the TPP and the SPP are excited at different interfaces of the same metal layer, thus revealing the repulsive nature of these two resonances [64].

However, the reason to study the amalgam formation was also related with general studies of various types of plasmonic surface waves optical features, when the use of material with high conductivity at optical frequencies, in order to have the possibility to tune the total dielectric function of the sensing layer through the presence of amalgam formation, which influence the coupling strength between the TPP and SPP resonances in the hybrid TPP-SPP mode.

The experimental studies of mercury adsorption and amalgam formation on the gold surface are consisted from two parts: the application of adequate optical model in order to characterize the inhomogeneous gold/mercury structures in real time (i) and to utilize different plasmonic excitations (single SPR, single TPP and hybrid TPP-SPP) for detection and analysis of gold/mercury amalgam structures (ii).

3.1.2 TIRE with surface plasmon resonance

In the present study, we utilized TIRE to demonstrate the influence of the interaction of Hg with an Au surface on the optical response of gold-based sensor and, as a result, on the determination of the composition by the percentage of the amalgam layer. It was shown that when an adequate optical model is used, the analysis of the experimental TIRE data gives close optical constants of the Au film before and after the formation of the amalgam layer on the gold surface.

This real time monitoring of the TIRE data produces important information about the formation of the amalgam layer on top of the gold film and its importance for sensor application.

3.1.3 Results and discussion

It is reasonable to assume that the mercury particles migrate not only to the surface but also diffuse deeper into the gold layer [141]. Thus, the amalgam layer was supposed to be composed of three Hg and two Au atoms with no regular structure in the surface plane. Therefore, the optical response of amalgam surface layer was analyzed in the frame of the Bruggeman EMA model. Even minuscule changes of the surface medium near the gold layer produce noticeable changes in the SPR resonance conditions (the curve shapes and the dip positions in the spectra). This is because the optical constants of the investigated mediums can be estimated with very high accuracy. In the EMA model for the amalgam surface layer on the top of gold film, it was assumed that the mercury atoms were attached and had penetrated through the surface to a depth of up to 5-6 nm. Indeed, the secondary ion mass spectroscopy results showed that the Hg response reached noise levels at 5-6 nm depths for the gold film left in a concentration of 0.007 mg/m^3 mercury for 30 minutes [144]. Previous studies had shown that the mercury atoms adsorb better onto a polycrystalline gold surface [141] because the mercury particles are more likely to aggregate at the surface defects. Furthermore, it has been argued that such mercury particles can migrate to energetically more favorable locations at the surface effects, hence forming islands instead of covering the whole surface evenly. The spectra of the ellipsometric parameters $\Psi(\lambda)$ and $\Delta(\lambda)$ for the pure gold layer showed (Fig. 3.1, Fig 3.2) that the surface plasmon waves manifested themselves as the dip in the $\Psi(\lambda)$ and the abrupt change of $\Delta(\lambda)$. This takes place at the λ = 598 nm wavelength at the external angle of the light incidence equal to 45°. As the amalgam layer was being formed on top of the gold surface, the SPR dip was blue shifted by 16 nm with

a decrease of the resonance depth from 2º up to 5.5º (Fig. 4a). Similar blueshift was observed for the $\Delta(\lambda)$ parameter in the vicinity of the PR generated wave. Meanwhile, the amplitude of the phase was suppressed from 360º up to 100º (Fig. 3.2).

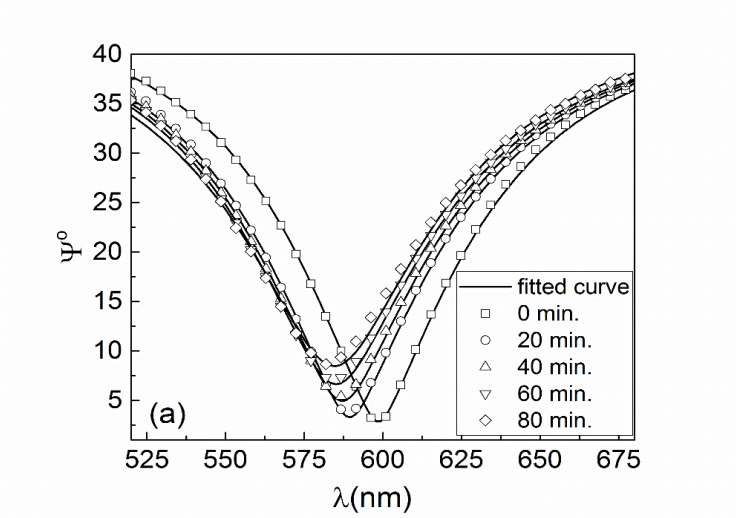

Figure 3.1. TIRE data of ellipsometric Ψ parameter points and fitted of different Au surface exposure to Hg times: □ - 0 min., ○ – 20 min., Δ – 40 min., ▽ – 60 min., ♦ – 80 min.

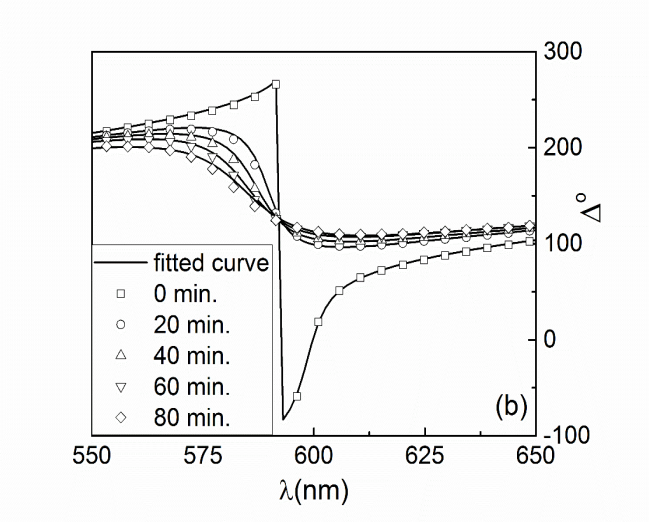

Figure 3.2. TIRE data of ellipsometric parameter Δ points and fitted of different Au surface exposure to Hg times: □ – 0 min., ○ – 20 min., Δ – 40 min., ▽ – 60 min, ♦ – 80 min.

The TIRE data for the pure gold layer was analyzed using the multi-layer model. In this study, the multi-layer model represented the following structure: BK7 glass prism/Cr/Au film/air. The optical constants of the thin gold layer were characterized using the Drude model and two Lorentz oscillators (Fig. 3.3). A layer of 1 nm thick Cr between the glass and the thin Au film was also included in the multi-layer model. The contribution of the gold layer surface roughness was taken into account in the calculations of the ellipsometric parameters $\Psi(\lambda)$ and $\Delta(\lambda)$ in order to develop an adequate model [143]. For the pure Au layer, the simulated data were fitted to the experimental ellipsometric results with a mean square error value of MSE = 9.

As was noted above, the Bruggeman EMA model was used in the analysis of the optical properties of the surface amalgam (Au_2Hg_3) layer (Fig. 3.1, Fig 3.2). The multi-layer ellipsometric model BK7 glass prism/Cr/Au film/Au_2Hg_3/air was used in the analysis of the hybrid structure containing the gold and mercury. The analysis of the TIRE data of a hybrid structure with an amalgam layer on top of the Au film was conducted using the analogues fitting procedure.

Several assumptions, however, were made. According to the AFM data, the island type structure of the amalgam layer situated on top of the gold surface was about 3.4 nm thick. SEM studies of this microstructure showed that the Au_2Hg_3 forms dendritic structures with an average surface coverage of ~35% percent. This data was acquired using the ImageJ image processing software. Bearing in mind the fact that most common amalgam structures consist of two gold and three mercury atoms (Au_2Hg_3) [145], it was reasonable to assume that the pure mercury in the surface layer of the amalgam would be about ~20% percent. Thus, the composition of the amalgam layer was estimated in the Bruggeman model as an effective media approximation using the parameters obtained from the SEM and ImageJ software analysis. It followed that the amalgam layer composed of 0.8Au + 0.2Hg and was used as a fix parameter to calculate the thickness changes of the pure gold and amalgam layers. The data of the optical constants for the Hg material were taken from the J. A. Woollam database [146], while the gold refractive index used was the same as that obtained from the regression procedure for the pure gold layer (Fig. 3.3). The regression analysis showed that the best fit was obtained when the thicknesses were d = 3.53 nm and d = 35.86 nm for the amalgam EMA and the pure gold layers, respectively. Furthermore, the thicknesses of both layers were fixed and only the percentage composition of Au and Hg in the amalgam

were being adjusted as free fitting parameters in the regression analysis of the formed structure. The best fitting of the experimental TIRE data was obtained for the following composition of the amalgam layer with a thickness of d = 3.53 nm: 0.84(Au) + 0.16(Hg). It should be noted that the amalgam layer thickness obtained from the regression analysis was in good agreement with the AFM data (d = 3.4 nm) (Fig. 2.8). The formed dendritic structure of the amalgam on the gold surface (Fig. 2.9) can be explained by the weak adhesion of some gold atoms to the film surface [144]. The SEM analysis showed that the mercury evaporated, whenever the surface areas were more intensely affected by the electron beam. Due to the mercury adsorption onto the gold, this increased the damping of the surface plasmon wave because the conductivity of mercury is higher than that of gold. This manifested itself as a decrease of the amplitude of the ellipsometric parameters $\Psi(\lambda)$ and $\Delta(\lambda)$ in the typical SPR curves and in the shifts to shorter wavelengths (Fig. 3.1, 3.2).

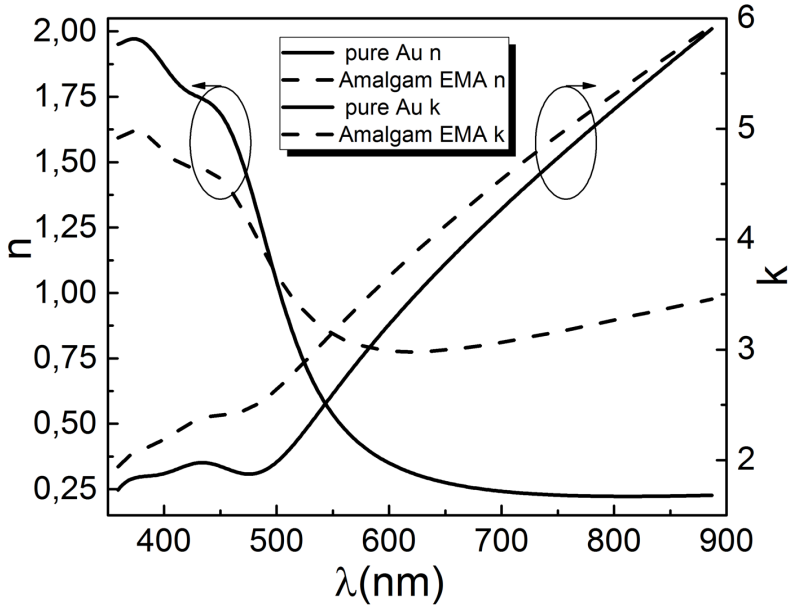

Figure 3.3. Complex refractive index n, k obtained from Bruggeman EMA multilayer model for mercury/gold EMA and pure gold layers.

A detailed understanding of the mercury adsorption mechanism on the gold surface can be acquired by analyzing the evolution of the ellipsometric parameters $\Psi(\lambda, t)$ and $\Delta(\lambda, t)$ over time. In this experiment, saturated mercury vapor with a concentration of 15 mg/m^3 at room temperature was used to form the amalgam layer on the top of the gold surface. The analysis of the dynamic TIRE data of the amalgam formation was performed using the reverse dynamic fitting procedure, starting from the values obtained for a completely formed amalgam layer. As noted above, the Bruggeman EMA has been used in kinetic data analysis for completely formed Au_2Hg_3 as well as for setting the initial point of regression. Reverse dynamic regression was performed starting from the thickness (d = 3.53 nm) and the ratio of gold ($84.00 \pm 0.43\%$) and mercury ($16.00 \pm 0.43\%$) in the completely formed amalgam film. During the mercury adsorption process, the percentage composition of the EMA layer needed to change, which was to be expected with the increasing number of mercury atoms adhering to the gold surface. Thus, the percentage composition (Fig. 3.4) of the amalgam dendritic structure were free adjustable parameters in the regression procedure. The regression analysis was performed backward in time starting from 120 min. back to 0 min. The real time measurements showed a fast change of the amalgam percentage composition up to 30 min. and then saturation. Similar regularities were reported for the SPR [135,136], ellipsometry [147], XPS and SEM [144] analysis. In this study the lowest obtained percentage composition of mercury was $0.6 \pm 0.4\%$ at the initial stage of the amalgam formation. In order to achieve reliable results, one point measurement time in our experiment was rather long, about 22 seconds, however, the detection limit of percentage composition with TIRE method can be even lower if time of data acquisition will be shorter with acceptable signal to noise ratio. Also, the noticeable influence to the precision comes from the gradient of the mercury gases in the chamber because SPR waves feel the changes of dielectric function of the medium below the gold surface [148].

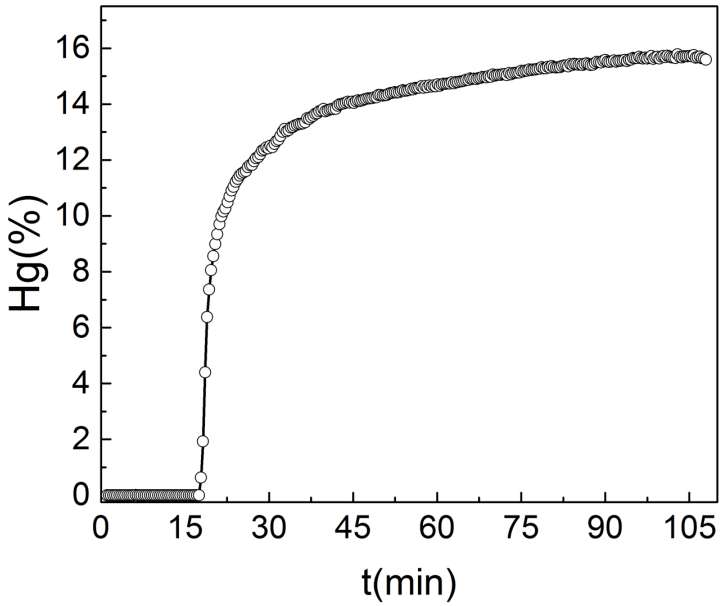

Figure 3.4. Percentage composition of mercury in Au and Hg EMA layer on mercury vapor exposure time.

3.1.4. Conclusions

The spectroscopic dynamic TIRE method was utilized for the characterization of the real time formation of the amalgam layer on the surface of a thin gold film. Summarizing, the structural and optical parameters that were determined from the regression analysis of the TIRE data provide important information about the amalgam surface layer, such as the percentages of its composition and its thickness. In particular, the regression results obtained by applying Bruggeman EMA model from steady state allowed us to reveal that the completely formed amalgam layer consist of $16.00 \pm 0.43\%$ mercury and $84.00 \pm 0.43\%$ gold. It should be noted that during the interaction of the mercury with the gold, the surface roughness of the gold increases in most cases. This factor creates a challenge, however, for optical methods. Present studies have shown, however, that the application of an effective medium approximation can solve this problem reasonably well.

To the best of our knowledge, the TIRE method in its dynamic acquisition mode was used for the first time to evaluate the percentage composition of the amalgam layer in real time. These results allow one not only to evaluate in

real time the percentage composition of the amalgam layer, but also to get further insight into the formation process during the interaction of the gold and mercury atoms on the sensor surface, which leads to the changes of the gold layer's optical constants. Moreover, TIRE, being an optical method, does not require any accumulation of the gold, unlike cold vapor atomic fluorescence spectroscopy (CVAFS), cold vapor atomic absorption spectroscopy (CVAAS) and inductively coupled plasma-atomic emission spectroscopy (ICP-AES). This makes it a promising method for obtaining rapid real time readouts.

3.2. TIRE with SPP, TPP and hybrid TPP-SPP mode

The aim of these studies has been to investigate the kinetic features of mercury vapor adsorption onto gold surfaces by utilizing the hybrid TPP-SPP mode in TIRE configurations, thus demonstrating the advanced capabilities of such hybrid excitation in the design of plasmonic sensors.

3.2.1. Results and discussions

The spectroscopic ellipsometry measurements of the single TPP and the single SPP samples indicated that the Tamm plasmon polariton and surface propagated plasmon waves manifested themselves as dips in the $\Psi(\lambda)$ spectra at 729 nm and 658 nm, respectively (Fig. 3.5 and 3.6). In the case of the single TPP sample, the external angle of light incidence was equal to 20º, while for the single SPP sample, the AOI was 42.5º in the prism coupler. For the single TPP sample, the fused silica substrate was set as the ambient material and according to the Snell law, the actual internal angle of light incidence for the fused silica glass/PC interface was adjusted via an angle offset of around $7º \pm 0.4º$. After the formation of the amalgam sub monolayer onto the gold surface, the ellipsometric parameters $\Psi(\lambda)$ and $\Delta(\lambda)$ blue shifted to 728 nm and 650 nm, respectively. A slight decrease of the resonance depths in $\Psi(\lambda)$ and the suppression of the amplitude in $\Delta(\lambda)$ were observed for both excitations. The predicted behavior of the optical response for both excitations was determined by the total conductivity changes in the mixed gold/mercury layer due to the formation of the amalgam.

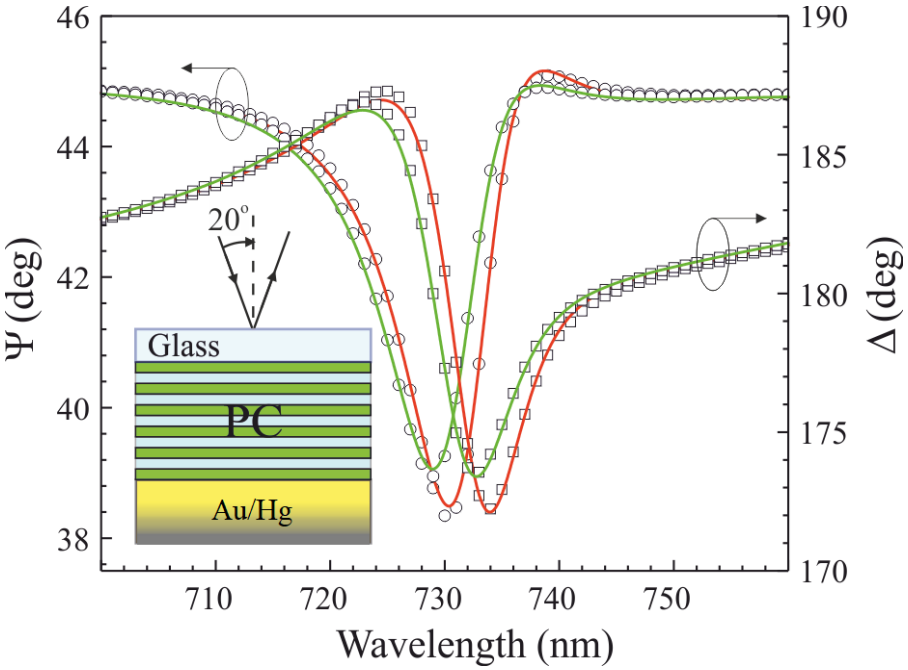

Figure 3.5. Experimental (dots) and calculated (solid curves) spectra of a single TPP sample before (red curves) and after (green curves) exposure to saturated mercury vapors. Inset represents the sample structure and the measurement configuration.

For the sample with the hybrid TPP-SPP mode, the behavior (Fig. 3.7) of the Tamm plasmon polariton component became opposite after the formation of the amalgam layer on the top of the gold layer. The TPP excitation moved to longer wavelengths, while the SPP moved to shorter wavelengths by the same blue shift (8 nm) as in the case of the single SPP sample (Fig. 3.6). It should be noted that the excitation of the hybrid TPP-SPP leads to different positions of the TPP (584 nm) and the SPP (684 nm) dip components (Fig. 3.7) when compared with the single TPP (729 nm) and the single SPP (650 nm), respectively. The TPP coupling with the SPP leads to the repulsion of both resonances. After the formation of the Au/Hg amalgam on the top of the gold layer, the coupling between the TPP and the SPP becomes weaker and both resonances move closer to each other.

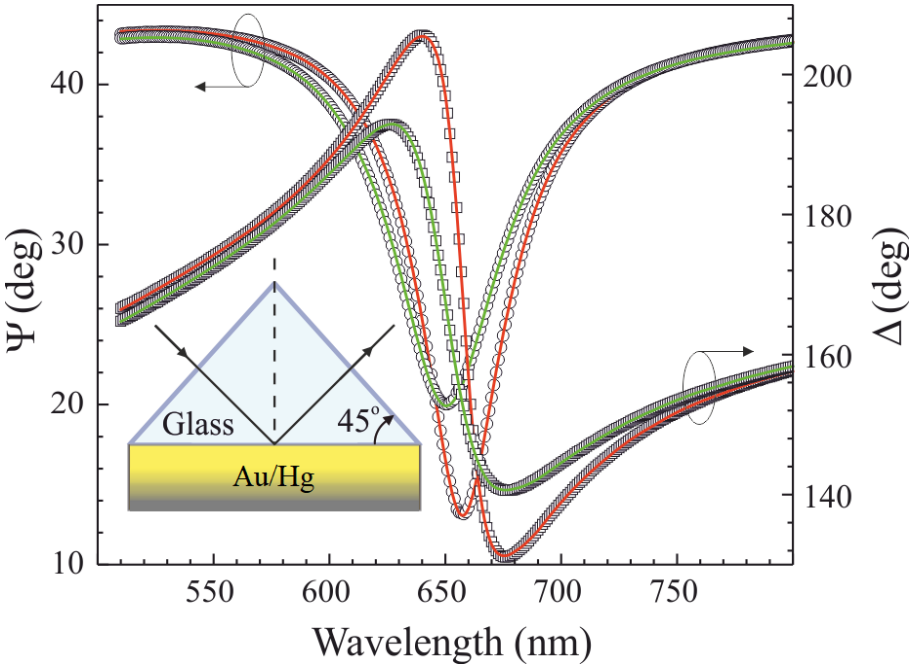

Figure 3.6. Experimental (dots) and calculated (solid curves) spectra of a single SPP sample before (red curves) and after (green curves) exposure to saturated mercury vapors. The inset represents the sample structure and measurement configuration.

It is reasonable to assume that the behavior of both TPP and SPP resonant components in the hybrid TPP-SPP mode were caused by two factors: the repulsion of the dispersion curves and the changes of conductivity in the plasmon active (gold) layer due to the formation of the amalgam. As noted above, the TPP and SPP resonances excited at different interfaces and were coupled inside the plasmon active layer. The penetration depth of both modes separately was about 25-30 nm into the gold layer [149].

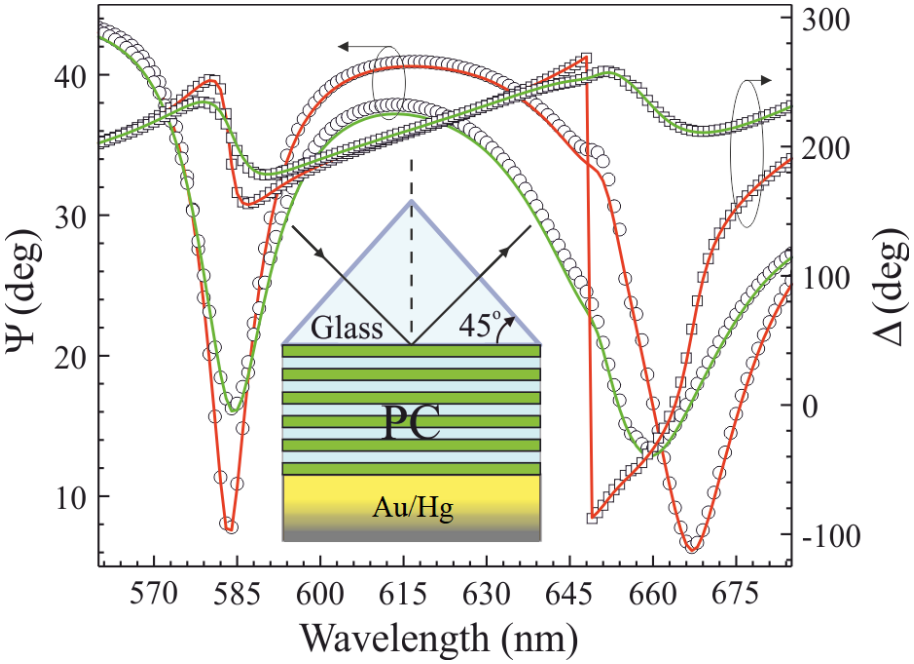

Figure 3.7. Experimental (dots) and calculated (solid curves) spectra of the hybrid TPP-SPP sample before (red curves) and after (green curves) exposure to saturated mercury vapors. The inset represents the sample structure and the measurement configuration.

The optical properties of the Au/Hg amalgam were determined from the thick gold layer, which had been incubated in the saturated mercury vapor chamber for 48 hours. The dielectric function of the Au/Hg amalgam was approximated as a homogeneous layer and described using the Bruggeman effective medium approximation (EMA). The EMA considers the Au/Hg amalgam film to be an isotropic physical mixture of two elements, Au and Hg, and homogenous on the scale of the wavelength. The dielectric function of the mixture was calculated from the volume fractions of its components, assuming that they retain their intrinsic optical properties. The evaluated volume fraction and thickness of the Au/Hg amalgam showed that the Au/Hg amalgam structure forms on the surface of the thick gold film, producing an increase of its thickness of 2.1 $\pm$ 0.2 nm (RMS = 1.1 nm). The volume fraction of the Hg in the EMA layer becomes 42 $\pm$ 1%. The thicker gold layer manifests better crystallinity and better adhesion, thereby blocking the further penetration of the mercury atoms deeper into the layer [144,147,150,151]. The same approach was used when analyzing the single TPP and the single SPP samples. The Au/Hg amalgam layer thicknesses and volume fractions of Hg obtained

from the analysis were 8.8 ± 0.1 nm (RMS = 0.4 nm), 4.9 ± 0.1 nm (RMS = 2.3 nm) and 19 ± 1 %, 14 ± 1% for single TPP and single SPP samples, respectively. Regression analysis of the single TPP and SPP samples also showed that the mercury atoms penetrated deeper into the gold layer by about 8 nm in the thin (~ 40 nm) gold films and showed comparable lower volume fractions of Hg.

T. Morris and G. Szulczewski have shown that spectroscopic ellipsometry is sensitive to mercury diffusion into the polycrystalline gold film [147]. However, due to the low penetration depth of the light, only a simple approximation can be used in the analysis of the data. For Au/Hg amalgam formation, the EMA approximation masks the details of the depth profile. The TPP and SPP resonances excited separately are in principle sensitive to their interfaces, inner and outer, respectively. Meanwhile, monitoring of the optical responses in the hybrid TPP-SPP modes has shown that changes of the coupling strength between the TPP and SPP resonances during the kinetic process can give additional information about the amalgam formation and the structural changes on the surface. A more adequate optical model with the contribution of the index-profile was applied to fit the experimental ellipsometric data of the hybrid TPP-SPP resonances in order to account for the penetration of the Hg atoms into the layer. For the Au/Hg amalgam, a gradient layer was used as an EMA mix of gold and mercury with two profiles, the linear and the exponential functions. However, only the exponential profile gave a satisfactory estimation of the optical properties of the Au/Hg amalgam in the investigated wavelength range. Dynamic regression analysis, however, allowed for the reliable determination of the thickness variation and index profile, which are presented in Fig. 3.8a. The thickness variation shown in Fig. 3.8a exhibits stepped Au/Hg amalgam growth process. For the first 40 min., the thickness increases exponentially. Later, after 30 min. of amalgam formation, the layer thickness begins to grow linearly up to 90 min. when the process was interrupted. This exponential growth corresponds to the Au/Hg amalgam formation, while linear part corresponds to the increased concentration (adsorption) of Hg atoms on the surface. The same similarities were observed in the dip position behavior shown in Fig. 3.8b. During formation of the Au/Hg amalgam surface layer, both resonances moved to shorter wavelengths, but after 30 min. the TPP dip started to move back. Finally, the TPP and SPP dips came closer to each other in the spectra by up to about 8 nm, indicating a weaker coupling between the resonances in the hybrid mode. The coupling strength of both resonances depends on the dispersion curves, which in turn are extremely sensitive to the total layer

conductivity, which increases drastically with the increase of the Hg atoms on the surface of the gold layer. The determined index profile shown in the inset of Fig. 3.8a demonstrated high, about 80% Hg, concentration near the surface, which decreased exponentially down into the layer. Numerical calculations were also performed to study how coupling of TPP and SPP depends on the conductivity and thickness of Au/Hg layer. The influence of metal layer thickness on dispersion curve repulsion was shown earlier [64]. Our evaluations were performed using the same parameters of the model structure as in the experiment for corresponding real time measurements. Calculation results revealed, that main influence at first minutes (t = 20 min) of Hg adsorption on coupling between TPP and SPP resonances (Fig. 3.8b) was due to increase of about 1.5 times of real part of conductivity from 300 to 500 $\Omega^{-1}cm^{-1}$ at 700 nm wavelength (Fig. 3.8a, green dots).

The determined values of the parameters from all the investigated samples confirmed the assumption that the mercury atoms penetrate into the gold layer for about 5 nm and form an Au/Hg amalgam structure, thus enhancing the optical signal changes related to the increased concentration of mercury atoms on the top of the sensor surface. It should be noted that the hybrid TPP component is not directly sensitive to the pure Hg, as this excitation formed on the other interface of the gold layer, however, weakening of coupling effect due to detuning of the SPP component from the optimal resonance conditions leads to the redshift of the TPP, which indicates Hg atoms adsorption on the surface. Very similar results of amalgam formation studies after 0.5-1 hour were reported earlier using structural methods such as XPS, secondary ion mass spectroscopy (SIMS), scanning Auger microscopy (SAM) and SEM [140,144].

The reported studies have shown that the saturation of the monitored signal takes place after about 30 min. and the penetration of Hg atoms deeper into the gold layer strongly depends on the adhesion and grain boundaries of the polycrystalline gold films [140,144]. It should be noted that in the case of the hybrid TPP-SPP mode, the behavior of the coupled excitations gives additional information about the penetration of the mercury atoms into the gold layer in comparison to the single TPP and SPP resonances.

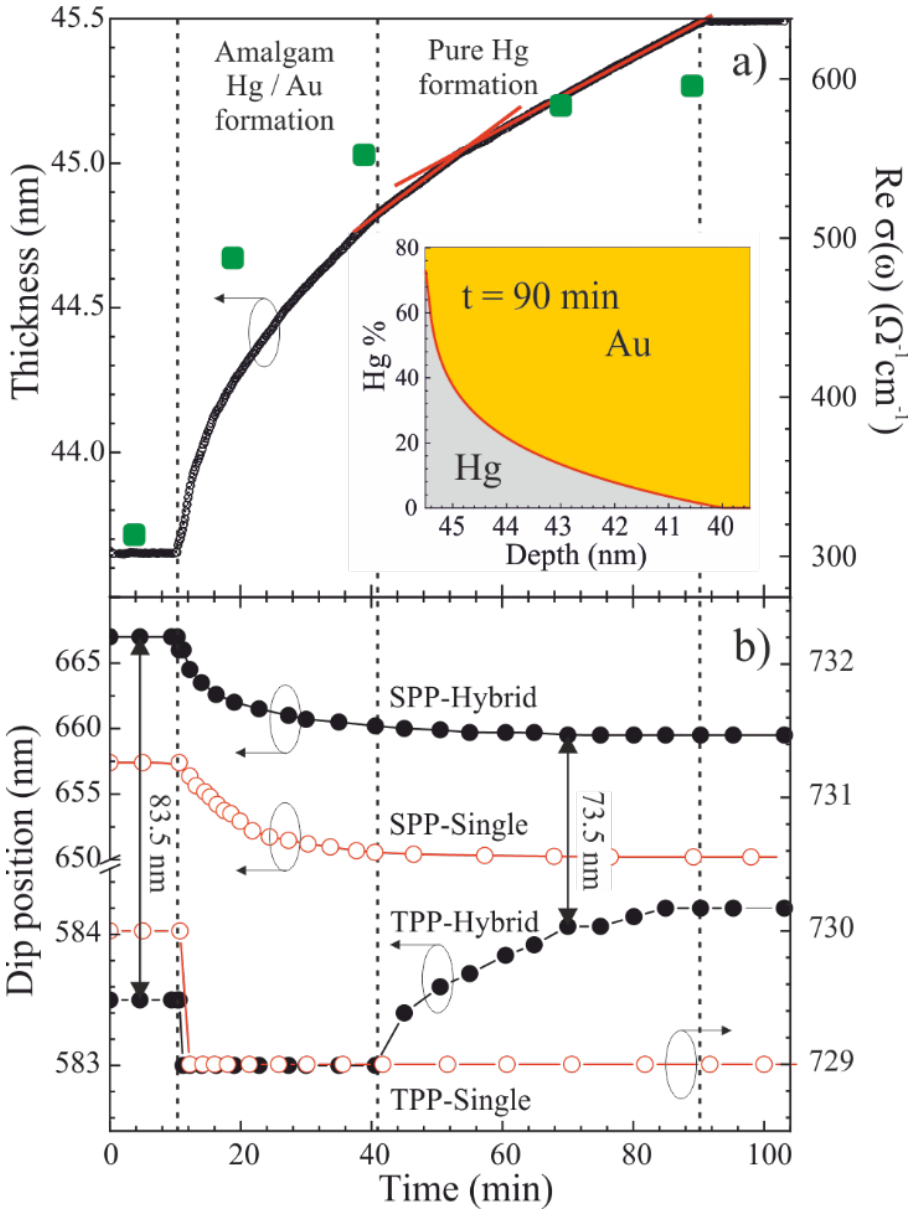

Figure 3.8. a) Thickness variation of the amalgam evaluated from regression analysis of the hybrid TPP-SPP mode. The inset shows the depth-profile of the gold and mercury at t = 90 min. Green dots correspond to real part of conductivity of Au/Hg layer at 700 nm wavelength. 5 b) The experimental $\Psi(\lambda)$ dip position dependence on the exposure time of the gold surface in the saturated mercury vapor.

Numerical calculations were also performed to study how coupling of TPP and SPP depends on the conductivity and thickness of Au/Hg layer. The influence of metal layer thickness on dispersion curve repulsion was shown earlier [64]. The curve repulsion or anti-crossing effect is a consequence of two interacting oscillators in strong coupling regime [64,152,153]. The stronger the interaction between oscillators the greater the distance between curves are. When coupling strength decreases curves moves closer to each other and eventually can overlap, this was showed in [64] with increasing the thickness of the thin metal film. However, the application of conductivity concept instead of thickness is more general from our point of view, because changes in metal layer thickness gives different conductivity as well.

Our evaluations were performed using the same parameters of the model structure as in the experiment for corresponding real time measurements. The calculation results revealed, that main influence at first minutes (t = 20 min.) of Hg adsorption on coupling between TPP and SPP resonances (Fig. 3.8b) was due to an increase of about 1.5 times of real part of conductivity from 300 to 500 $\Omega^{-1}cm^{-1}$ at 700 nm wavelength (Fig. 3.8a (green dots) or Fig. 3.10).

From the Fig. 3.9 we can see that gap change between dispersion curves of TPP and SPP resonances are much bigger in the first 20 minutes than in the last 20 minutes. Similar decrease in change can be seen in conductivity graph in Fig 3.10. This could be explained by the change of resonance condition for SPR component.

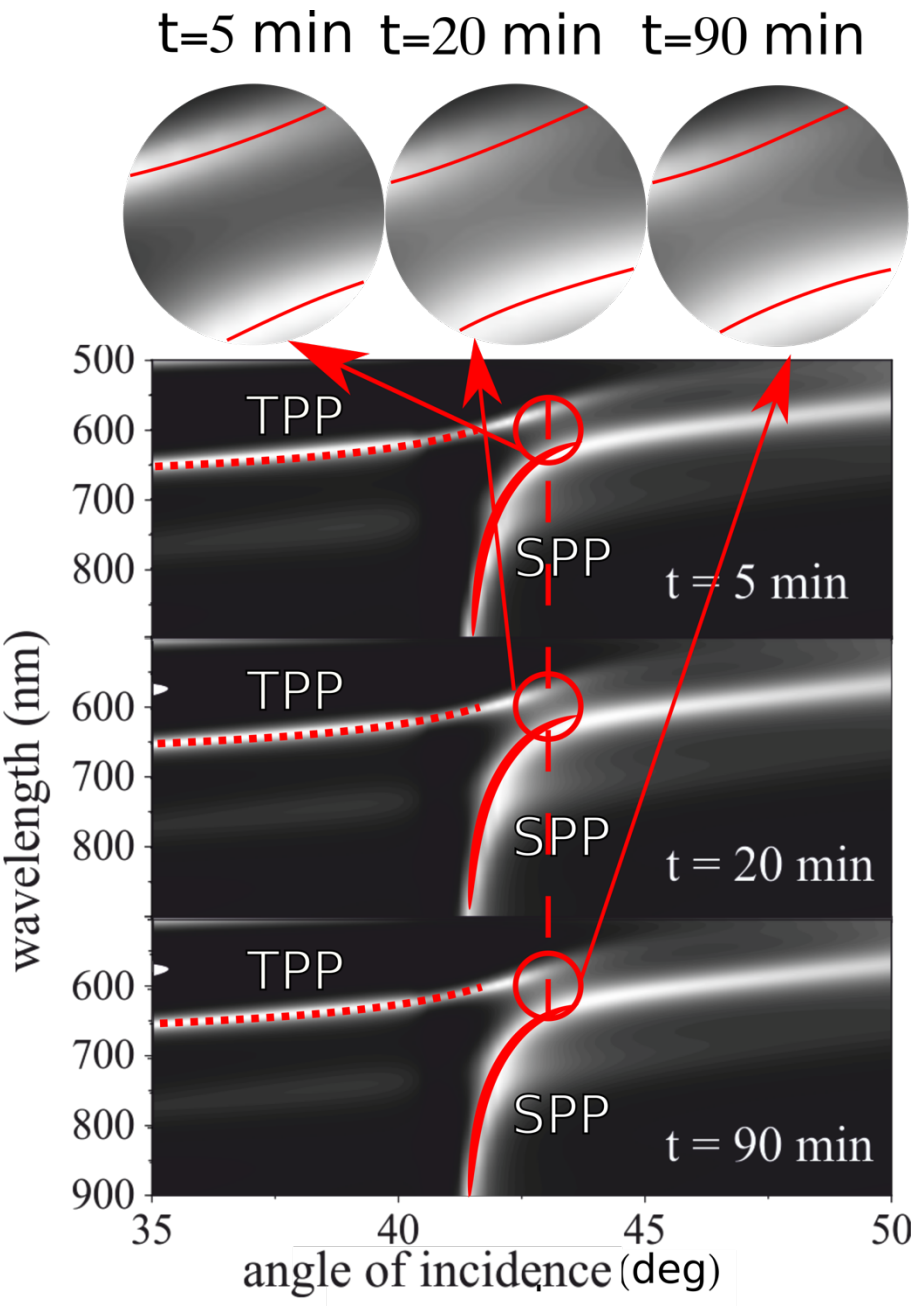

Figure 3.9. Image plots of the reflectivity spectra for p-polarization calculated at corresponding experimental time (white – 1, black - 0).

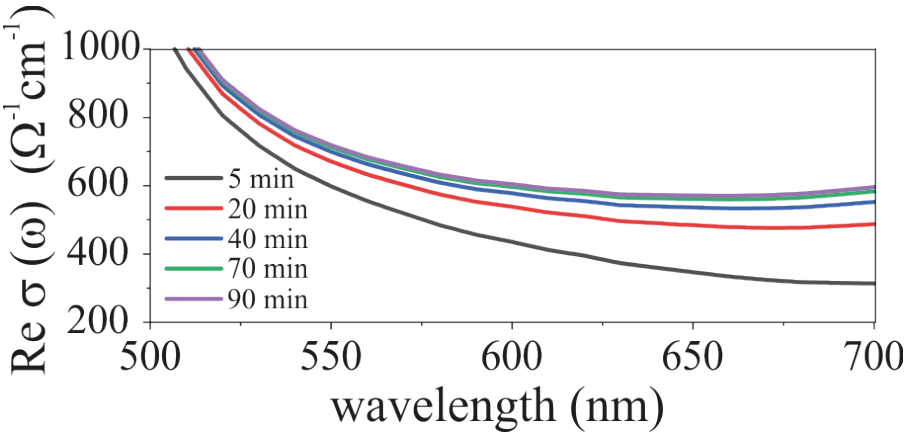

Figure 3.10. Spectra of the real part of Au/Hg optical conductivity at corresponding experiment time.

3.2.2 Conclusions

The spectroscopic dynamic TIRE method was used for the generation and study of the hybrid TPP-SPP mode as a sensor probe for the real time formation of amalgam structures on the surface of a plasmon active gold layer. The mercury atoms penetration into gold layer was determined through the experimental data acquired through TIRE and the regression analysis of a multi-layer model with an index-profile amalgam layer. In particular, from the regression analysis of all studied samples and previously reported publications [144,147,1*], we can conclude that mercury atoms penetrate about 5 nm into polycrystalline gold layers.

The present study has demonstrated the applicability of hybrid TPP-SPP mode to advanced optical gas sensors technologies. These results allow not only the evaluation of the coupling strength of the TPP and SPP components of the hybrid mode in the plasmon active layer, but also provide some insight into the real time formation of the amalgam on the sensor surface.

3.3. TIRE on nanolaminates

Recently, there has been a large interest in the results obtained from zinc oxide thin films and nanolaminates and their relevant properties for use as materials for optical biosensors [81–83]. ZnO thin films and nanolaminates can be deposited using various methods [82,83]. They are bio-compatible, non-toxic and chemically stable [84]. The high isoelectric point of ZnO can also be used for the immobilization of proteins with low isoelectric points through electrostatic interactions [85]. Additionally, ZnO nanomaterials demonstrate controllable wettability, which allows the reduction of the volume of the

sample, a quick response, increased sensitivity and signal-to-noise ratio of the developed biosensors [86]. Moreover, ZnO is compatible with complementary metal oxide semiconductor technology and therefore is suitable for the production of integrated circuits for devices with small integrated biosensors [81]. Thus, ZnO based multi-layered structures (nanolaminates) have been selected as substrates for optical biosensor designs in total internal reflection ellipsometry configurations.

The aim of these studies has been to evaluate the influence of the layered structures of Al_2O_3/ZnO nanolaminates on the optical responses of ellipsometric parameters Ψ and Δ in total internal reflection configurations and to demonstrate the advanced possibilities of such layered structures in optical biosensors designs.

3.3.1 Results and discussion

3.3.1.1 Simulations

In order to use Al_2O_3/ZnO nanolaminates on glass substrates for bio-sensing applications, simulations of the ellipsometric parameters were conducted to determine the best parameters (thicknesses and refractive index) of the multilayer structures in which the sensitivity properties would be optimized. Furthermore, the simulations were done in an external reflection (reflection ellipsometry) setup. Conventional reflection ellipsometry simulations showed that the features of the optical response of the ellipsometric parameters increased at 50 nm Al_2O_3 and ZnO layers thicknesses, while for thicker and thinner layers of Al_2O_3 and ZnO in nanolaminates, these optical features decreased. Thus, for further studies, nanolaminates with layers of 50 nm thickness were chosen in order to improve the sensitivity of the system. However, as mentioned above, the TIRE configuration is more appropriate for bio-sensing applications due to the possibility of conducting optical measurements in liquid and/or an opaque medium without light passing through them [154]. In this configuration, a better signal to noise ratio is obtained and the light scattering effect is minimized. Thus the Al_2O_3/ZnO nanolaminates on the glass substrates were examined in the TIRE configuration and the two bilayer (50 nm/50 nm) Al_2O_3/ZnO nanolaminates, the one bilayer (100 nm/100 nm), the single ZnO film (200 nm) and the single Al_2O_3 (200 nm) film with the same total thicknesses (200 nm) for all samples were compared in order to find out the differences in the sensitivity features (Fig. 3.11 a, b, Fig 3.12 a, b). Analysis of the maximal shift in the optical response of the conducted simulations showed that the multilayered structures

of the Al_2O_3/ZnO (50 nm/50 nm) nanolaminates had a two-fold increase in sensitivity to a 10 nm protein layer than the single ZnO film of the same total thickness (200 nm). As can be seen from Fig. 3.11 a, b, Fig. 3.12 a, b, the changes in the ellipsometric parameter Δ due to the 10 nm simulated bio-layer gives $\Delta = 11.8^o$, $\Delta = 5.44^o$, while for the Al_2O_3/ZnO nanolaminates with two bilayers, one bilayer, the single ZnO (200 nm) layer and the single Al_2O_3 (200 nm), these are $\Delta = 6.02^o$ and $\Delta = 1.4^o$, respectively. The protein refractive index dispersions were modelled with the Cauchy function and had the following values: A = 1.45, B = 0.01 and C = 0. The contribution of a few nanometers of the APTES layer was also taken into account. In order to determine the contribution of the layered structure, two samples with different bilayer numbers, but with the same amount of aluminum and zinc oxide were analyzed in more detail. From the optical response of these two samples, it can be clearly seen (Fig. 3.11 a, b) that a structure with two bilayers had better sensitivity at a 10 nm thickness of the simulated bio-layer ($\Delta = 11.8^o$) than a sample with one bilayer ($\Delta = 5.44^o$). As the amounts of both materials were the same in these simulated samples, it is reasonable to assume that enhancement of the optical response comes from the number of layers in the nanolaminate structures due to the multiple reflections of light from the interfaces between the Al_2O_3 and ZnO layers. Thus, for the TIRE experiment with proteins, the structure of the Al_2O_3/ZnO nanolaminates with two bilayers (50 nm/50 nm) with a total thickness of 200 nm was chosen.

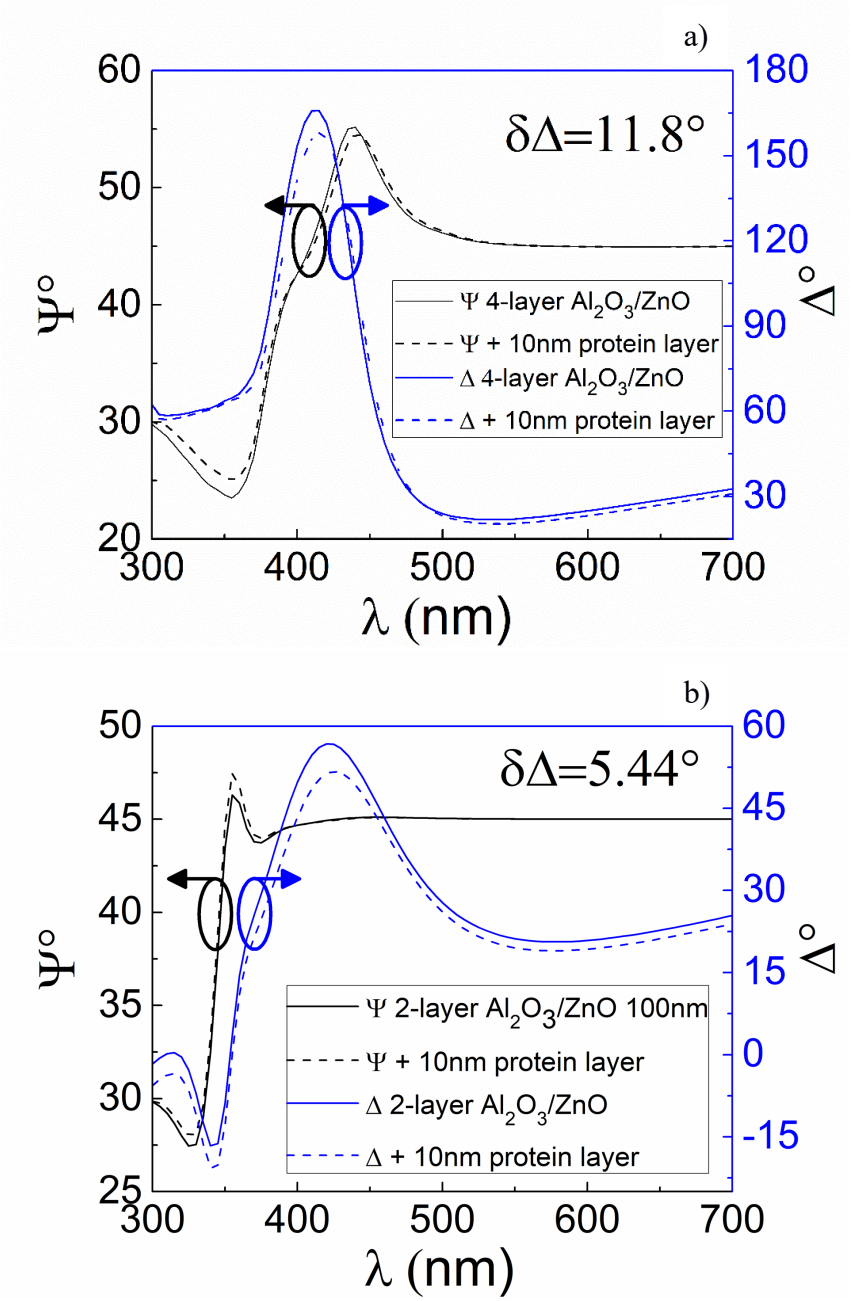

Figure 3.11. Simulated TIRE spectra (solid curves) of a) two bilayer (50 nm/ 50nm) Al_2O_3/ZnO nanolaminates, b) one bilayer (100nm/100nm) Al_2O_3/ZnO nanolaminates. The dashed curves represented the changes of ellipsometric parameters $\Psi(\lambda)$ and $\Delta(\lambda)$ due to the 10 nm thickness of the bio-layer on the top that was modeled by Cauchy function.

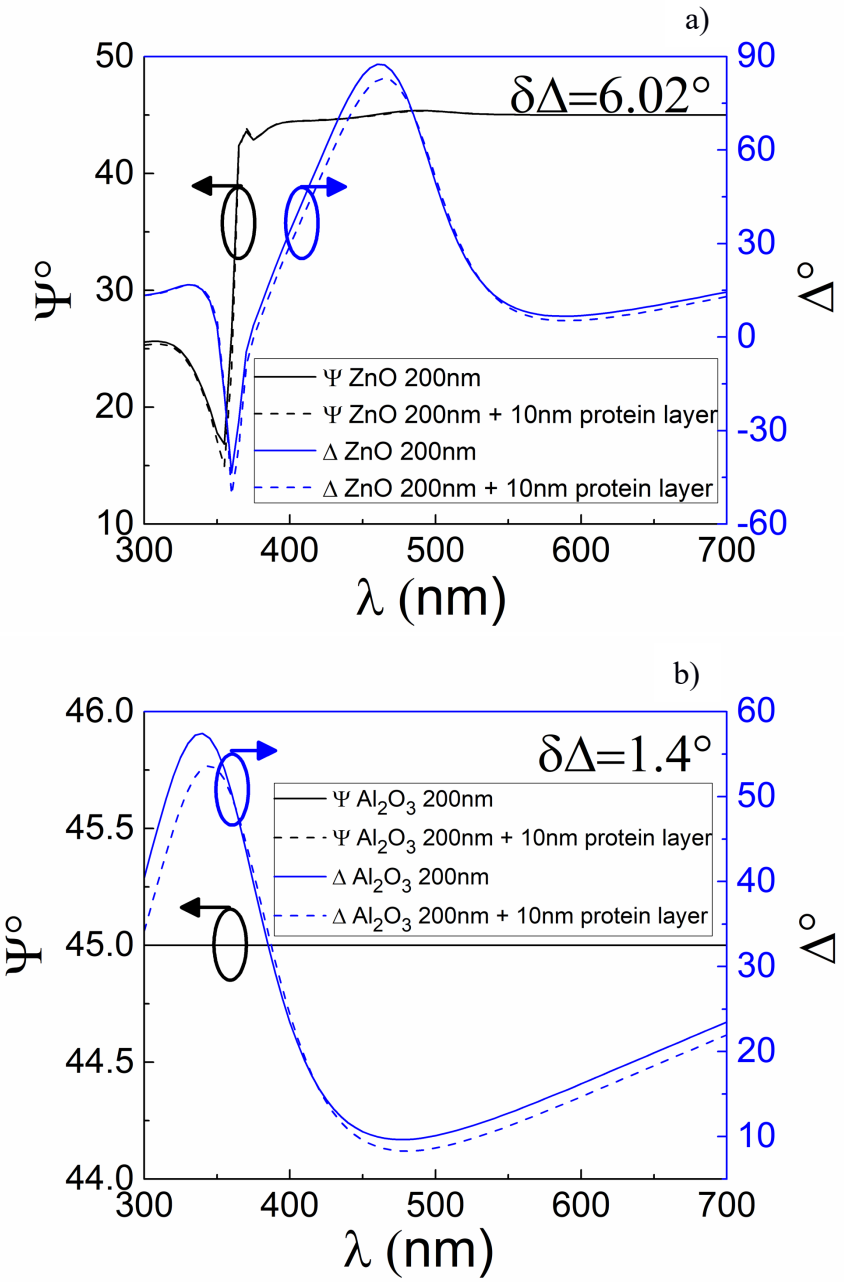

Figure 3.12. Simulated TIRE spectra (solid curves) of a) 200 nm ZnO films and b) 200 nm Al_2O_3. The dashed curves represented the changes of ellipsometric parameters $\Psi(\lambda)$ and $\Delta(\lambda)$ due to the 10 nm thickness of the bio-layer on the top that was modeled by Cauchy function.

3.3.1.2. Optical properties of Al_2O_3/ZnO nanolaminates

In order to use layered Al_2O_3/ZnO nanolaminate structures for the biosensor design, the optical properties of these samples have to be characterized. For this purpose, the ellipsometric spectra of the Al_2O_3/ZnO nanolaminates were recorded in a total internal reflection configuration. The spectra of the ellipsometric parameters $\Psi(\lambda)$ and $\Delta(\lambda)$ for the nanolaminates/APTES are shown in Fig. 3.13. The presence of optical losses due to ZnO absorption manifested themselves as the peaks in the $\Psi(\lambda)$ and $\Delta(\lambda)$. This takes place at the $\lambda \approx 400$ nm wavelength at an external angle of the light incidence to the prism equal to 70°. The optical dispersions of the refractive indexes of Al_2O_3 (Fig. 3.14) and ZnO (Fig. 3.14) were evaluated by regression analysis from the multilayer model and were then used as fixed parameters in the BSA covalent immobilization experiment.

In this study, the multi-layer model representing the five-phase structure of the nanolaminates consisted of two bilayers of Al_2O_3/ZnO (50 nm/50 nm) on glass substrates with each bilayer being 100 nm thick. In the regression analysis, the starting values of the optical dispersion were taken from the CompleteEASE database and the thicknesses of the layers were the 50 nm free fitting values. The optical constants of the Al_2O_3 layers in the nanolaminates were characterized using the Cauchy dispersion function. The regression results showed that the thicknesses of the Al_2O_3 layers in the nanolaminates were 49.72 ± 0.56 nm and 50.20 ± 0.43 nm for first and second bilayer, respectively. Meanwhile, the optical constants for the ZnO layers were determined by using PSemi-M0 and two Gaussian peaks functions. The obtained dispersions of the ZnO and Al_2O_3 optical constants are presented in Fig. 3.14. The evaluated thicknesses of the ZnO layers were 50.19 ± 0.47 nm and 49.77 ± 0.61 nm for the first and second bilayers, respectively. The refractive index and extinction coefficient of the APTES layer was also determined by the Cauchy function. The obtained optical constant dependences of the wavelength are presented in Fig 3.15. The evaluated thickness of the (3-Aminopropyl)trimethoxysilane layer using these optical constants was 6.99 ± 0.79 nm. For the six phase structure of the nanolaminates with the APTES layer on the top of the ZnO surface, the modelled data were fitted to the experimental ellipsometric results with a mean square error value of MSE = 12.72.

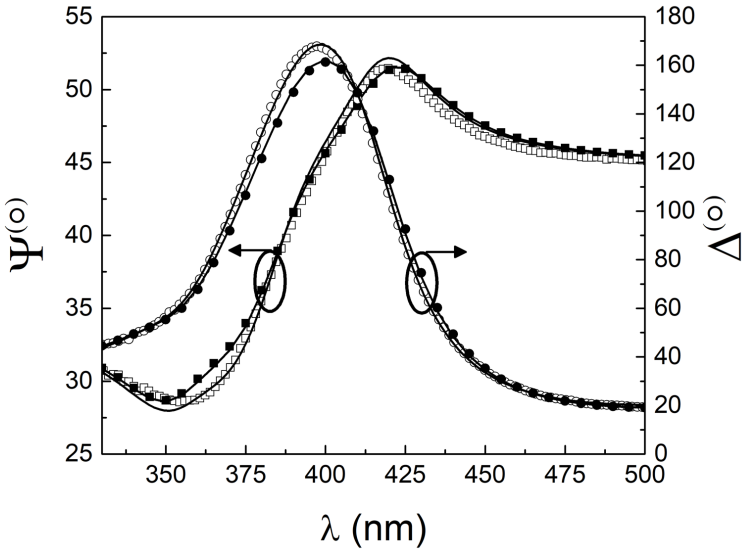

Figure 3.13. The TIRE data of the ellipsometric parameters' *Ψ(λ)* and *Δ(λ)* points and the fitted curves (solid lines) of the six phase structure of the two bilayer Al_2O_3/ZnO (50 nm/50 nm) nanolaminates, the APTES layer on the ZnO surface (*Δ* – ○; *Ψ* – □) with the BSA layer immobilized on the top of the APTES surface (*Δ* – ●; *Ψ*– ■).

3.3.1.3 Evaluation of Al_2O_3/ZnO nanolaminates as possible substrates for biosensing

As was noted above, for bio-sensing purposes, the top layer of the nanolaminates (ZnO, the sensing surface) was modified by APTES. Afterwards, the surface was functionalized by amino groups, which are necessary for bovine serum albumin covalent immobilization onto the ZnO surface. In this experiment, BSA (as a model protein) was used to form the bio-molecular layer on the top of the

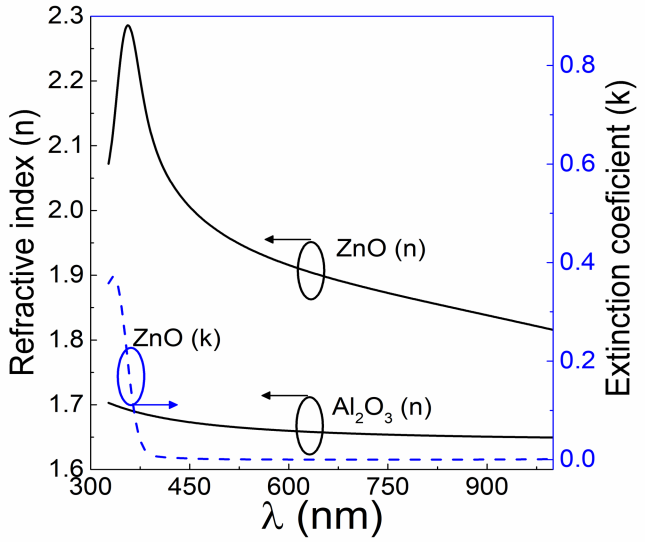

Figure 3.14. ZnO and Al_2O_3 optical dispersion of the complex refractive index in Al_2O_3/ZnO nanolaminates

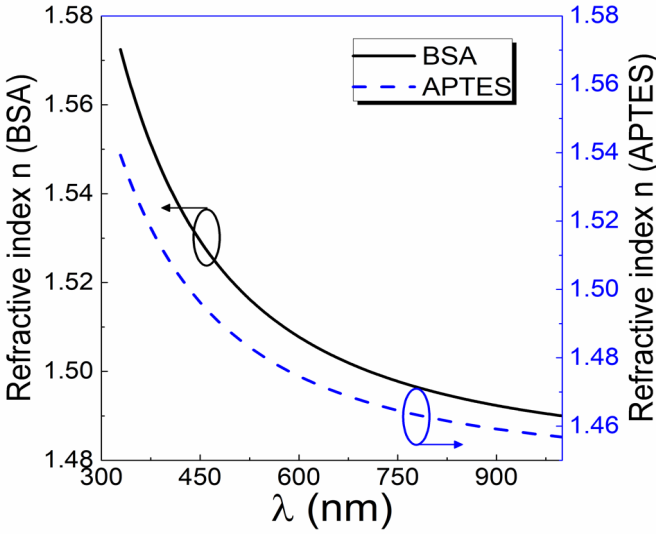

Figure 3.15. Refractive index (solid curve) of bovine serum albumin covalently immobilized on a ZnO surface modified with APTES. Refractive index dispersion of APTES film (dashed curve) formed on a ZnO surface.

ZnO surface at room temperature. The concentration of the BSA, which was used for recording the kinetic interaction between the BSA activated functional groups and salinized ZnO surface, was 0.1 mg/ml. The nonspecific BSA adsorption on a salinized surface was also investigated. The covalently immobilized BSA refractive index was determined by applying the Cauchy dispersion function as was used for the (3-Aminopropyl)trimethoxysilane layer (Fig. 3.15). As the BSA layer was being formed on the top of the modified ZnO surface, the peak was slightly red-shifted, producing a decrease of its amplitude for the $\Psi(\lambda)$. A similar behavior was observed for the $\Delta(\lambda)$ parameter in the vicinity of the absorption band of the ZnO (Fig. 3.13). Due to the formation of the BSA layer on top of the ZnO surface, the ellipsometric parameter $\Delta(\lambda)$ changed up to 12° at $\Psi(\lambda)$ and $\lambda = 390$ nm, while the maximum shift for $\Psi(\lambda)$ was 1.7° at $\lambda = 370$ nm. The regression analysis showed that such changes in ellipsometric parameters correspond to the 7.3 ± 0.67 nm thickness of the BSA layer. A detailed understanding of the protein immobilization process on the solid-liquid interfaces can be obtained by analyzing the evolution of the ellipsometric parameter $\Delta(t)$ over time (Fig. 3.16a). The TIRE method in its dynamic data acquisition mode is able to evaluate the changes of the refractive index and thickness over time however, obtained physical quantities usually are converted into more appropriate information about biomolecules. A common approach in various types of biosensors is the evaluation of the surface mass attached on the sensor surface. For this purpose, the dynamic TIRE data of the refractive index and thickness were converted to changes of the surface mass using de Feijter's formula [155] during the formation of the BSA layer (Fig. 3.16b). While both parameters - film thickness and refractive index - were determined from regression analysis. $\Gamma = \frac{d(n-n_{buffer})}{dn/dC} \times 100$ (3.1) was used to evaluate the surface mass (ng/cm^2), where $dn/dC = 0.18 \frac{cm^3}{g}$ [156] is the refractive index increment for the layer material, depending on the protein concentration in the buffered solution , d is the thickness (nm) of the protein layer obtained from regression analysis, n is the refractive index of the protein layer obtained from regression analysis and n_{buffer} is the refractive index of the buffered solution. The evolution of the surface mass amount was calculated at intervals of about 4 min. and the fast change of the BSA proteins surface mass up to 27 min. when saturation was clearly seen.

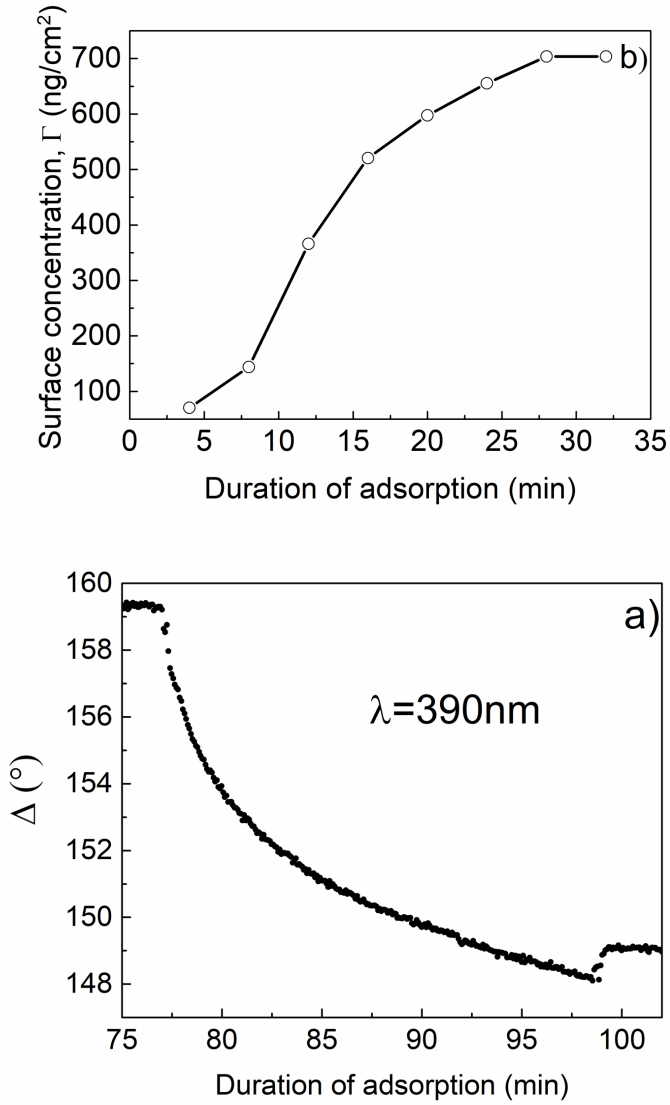

Figure 3.16. a) The kinetics covalently BSA immobilization on the surface of APTES-modified Al_2O_3/ZnO nanolaminate, parameter Δ at 390 nm wavelength; b) the surface concentration of BSA calculated from TIRE data using equation (3.1).

3.3.2. Conclusions

The spectroscopic dynamic TIRE method was utilized for the characterization of the real time formation of the BSA layer on the surface of the functionalized Al_2O_3/ZnO nanolaminates. The conducted simulations of the optical response

of structures with bilayers of Al_2O_3/ZnO (50 nm/50 nm) nanolaminates showed a twice better change of the ellipsometric parameter Δ of the bio-layer on the top of the ZnO surface compared to ZnO of 200nm thickness with one bilayer of Al_2O_3/ZnO (100 nm/100 nm) nanolaminates. The increased sensitivity of the ellipsometric parameters can be explained by the multiple reflection of the light waves in a condition of total internal reflection, especially for the ellipsometric parameter Δ. These studies showed that the number of bilayers and the thicknesses of the films have a noticeable influence on the sensitivity of these kinds of optical biosensors. Therefore, the refractive index dispersion of the layers needs to be optimized by taking into account the materials from which they are made. Such multiple total internal reflections are very commonly used in attenuated total reflection – Fourier transform infrared (ATR-FTIR) spectroscopies [9]. However, to the best of our knowledge, the exploitation of multiple TIR effect with spectroscopic ellipsometry in the UV-VIS spectral range for the optical biosensors design is being used for the first time. It should be noted, that the TIRE method with dielectric multilayer structures is less sensitive to surface changes than the TIRE with thin metal films, which utilizes the SPR effect. This observation can be explained by the different localization of the electric field on the sensing surfaces. However, the biocompatibility, the photoluminescence features of ZnO [157] and the optical properties of ZnO/Au nanostructures [158], such as the simultaneous real time monitoring of SPR [159] or localized SPR [70] effects in VIS and the photoluminescence peak of ZnO in the UV range, produce possibilities of constructing optical biosensors with advanced features.

- The spectroscopic dynamic TIRE method was utilized for the characterization of the real time formation of the amalgam layer on the surface of a thin gold film. To the best of our knowledge, the TIRE method in its dynamic acquisition mode was used for the first time to evaluate the percentage composition of the amalgam layer in real time. This makes it a promising method for obtaining rapid real time readouts. These results allow one not only to evaluate in real time the percentage composition of the amalgam layer, but also to get further insight into the formation process during the interaction of the gold and mercury atoms on the sensor surface, which leads to the changes of the gold layer's optical constants.

- Summarizing, the structural and optical parameters that were determined from the regression analysis of the TIRE data provide important information about the amalgam surface layer, such as the percentages of its composition and its thickness. In particular, the regression results obtained by applying Bruggeman EMA model from steady state allowed us to reveal that the completely formed amalgam layer consist of 16.00 $\pm$ 0.43% mercury and 84.00 $\pm$ 0.43% gold. It should be noted that during the interaction of the mercury with the gold, the surface roughness of the gold increases in most cases. This factor creates a challenge, however, for optical methods. Present studies have shown, however, that the application of an effective medium approximation can solve this problem reasonably well.

- The spectroscopic dynamic TIRE method was used for the generation and study of the hybrid TPP-SPP mode as a sensor probe for the real time formation of amalgam structures on the surface of a plasmon active gold layer. The mercury atoms penetration into gold layer was determined through the experimental data acquired through TIRE and the regression analysis of a multi-layer model with an index-profile amalgam layer. In particular, from the regression analysis of all studied samples, we can conclude that mercury atoms penetrate about 5 nm into polycrystalline gold layers.

- The present study has demonstrated the applicability of hybrid TPP-SPP mode to advanced optical gas sensors technologies. These results allow not only for the evaluation of the coupling strength of the TPP and SPP

components of the hybrid mode in the plasmon active layer, but also provide some insight into the real time formation of the amalgam on the sensor surface.

- The spectroscopic dynamic TIRE method was utilized for the characterization of the real time formation of the BSA layer on the surface of the functionalized Al_2O_3/ZnO nanolaminates. The increased sensitivity of the ellipsometric parameters can be explained by the multiple reflection of the light waves in a condition of total internal reflection, especially for ellipsometric parameter Δ.

- These studies showed that the number of bilayers and the thicknesses of the films have a noticeable influence on the sensitivity of these kinds of optical biosensors. Therefore, the refractive index dispersion of the layers needs to be optimized by taking into account the materials from which they are made.

- It should be noted, that the TIRE method with dielectric multilayer structures is less sensitive to surface changes than the TIRE with thin metal films, which utilizes the SPR effect. This observation can be explained by the different localization of the electric field on the sensing surfaces. However, the biocompatibility, the photoluminescence features of ZnO [157] and the optical properties of ZnO/Au nanostructures [158], produce possibilities of constructing optical biosensors with advanced features.

Notations and abbreviations

Main notations

A, B, C – Cauchy function coefficients
c – speed of light
C – concentration
d_{Ez}, d_{Iz} - penetration depth for electromagnetic field and intensity
e - electron electric charge
E - electric field
H - magnetic field
I - electromagnetic field intensity
k - wave vector
m_e - electron mass
n - refractive index
N_e - number of electrons per volume unit
p – parallel to the reflection plane polarization
r_p, r_s - Fresnel reflection coefficients
R - reflectance
s – perpendicular to the reflection plane polarization
t – time
x, y, z – cartesian coordinate axis
γ - shape and size dependent factor
Γ - surface mass
Γ – damping in Drude model
δ - phase change upon reflection
ϵ - dielectric constant
ϵ_0 - vacuum dielectric function
θ_B - Brewster's angle
θ_c - critical angle from which total internal reflection occurs
θ_i - incidence angle
λ - electromagnetic radiation wavelength
μ - magnetic permeability
ρ - complex reflectance ratio measured with ellipsometry
σ - electrical conductivity
χ - electromagnetic radiation's complex polarization state
Ψ, Δ - ellipsometric parameters
ω - electromagnetic radiation frequency
ω_p - plasma frequency
ω_{sp} - surface plasmon frequency

Abbreviations

1D – one dimensional
2D – two dimensional
3D – three dimensional
AFM – atomic force microscopy
ALD – atomic layer deposition
AOI – angle of incidence
APTES – N-(3-aminopropyl) triethoxysilane
ATR – attenuated total reflection
BSA – bovine serum albumin
BSW – Bloch surface wave
CCD – charge-coupled device
CVAAS – cold vapor atomic absorption spectroscopy
CVAFS – cold vapor atomic fluorescence spectroscopy
EDC – 1-ethyl-3-(3-diaminopropyl) carbodiimide hydrochloride
EDX – energy dispersion X-ray
EELS – electron energy loss spectroscopy
EMA – effective medium approximation
FECO – fringes of equal chromatic order
FTIR – Fourier transform infrared
ICP-AES – inductively coupled plasma-atomic emission spectroscopy
IRE – internal reflection ellipsometry
LC – liquid crystal
LO – longitudinal optical
MDF – model dielectric function
MSE – mean square error
NHS – N-hydroxysuccinimide
PBS – phosphate buffered saline
PC – photonic crystal
PL – photoluminescence
RMS – root mean square
SAMS – scanning Auger microscopy
SE – spectroscopic ellipsometry
SEM – scanning electron microscopy
SIMS – secondary ion mass spectroscopy
SP – surface plasmon
SPP – surface plasmon polariton
SPR – surface plasmon resonance
TE – transverse electric
TIR – total internal reflection
TIRE – total internal reflection ellipsometry
TM – transverse magnetic
TP – Tamm plasmon
TPP - Tamm plasmon polariton
UV – ultraviolet
VIS – visible
XPS – X-ray photoelectron spectroscopy

Bibliography

1. J. Hu, L. Ma, S. Wang, J. Yang, K. Chang, X. Hu, X. Sun, R. Chen, M. Jiang, J. Zhu, and Y. Zhao, "Biomolecular Interaction analysis using an optical surface plasmon resonance biosensor: The marquardt algorithm vs Newton iteration algorithm," PLoS One **10**(7), (2015).

2. Y. Zhang, Y. Chen, and G. Jin, "Serum tumor marker detection on PEGylated lipid membrane using biosensor based on total internal reflection imaging ellipsometry," Sensors Actuators, B Chem. **159**(1), 121–125 (2011).

3. Z. Balevicius, I. Baleviciute, S. Tumenas, L. Tamosaitis, A. Stirke, A. Makaraviciute, A. Ramanaviciene, and A. Ramanavicius, "In situ study of ligand-receptor interaction by total internal reflection ellipsometry," Thin Solid Films **571**(P3), 744–748 (2014).

4. M. Maisonneuve, I.-H. Song, S. Patskovsky, and M. Meunier, "Polarimetric total internal reflection biosensing," Opt. Express **19**(8), 7410 (2011).

5. K. Hinrichs, K. J. Eichhorn, G. Ertl, D. L. Mills, and H. Lüth, "Ellipsometry of Functional Organic Surfaces and Films," Springer Ser. Surf. Sci. **52**, (2014).

6. W. Wang, Y. Yang, S. Wang, V. J. Nagaraj, Q. Liu, J. Wu, and N. Tao, "Label-free measuring and mapping of binding kinetics of membrane proteins in single living cells," Nat. Chem. **4**(10), 846–853 (2012).

7. A. Lizana, M. Foldyna, M. Stchakovsky, B. Georges, D. Nicolas, and E. Garcia-Caurel, "Enhanced sensitivity to dielectric function and thickness of absorbing thin films by combining total internal reflection ellipsometry with standard ellipsometry and reflectometry," J. Phys. D. Appl. Phys. **46**(10), 105501 (2013).

8. Y. Zhou, H. Zou, L. Zhong, J. Li, B. Li, J. Tian, and X. Lu, "Dynamic refractive index distribution measurement of dynamic process by combining dual-channel simultaneous phase-shifting interferometry

and total internal reflection," Sci. Rep. **8**(1), 15231 (2018).

9. Z. Balevicius, D. Ignatjeva, G. Niaura, I. Ignatjev, V. Vaicikauskas, G. J. Babonas, and G. Valincius, "Crowding enhances lipase turnover rate on surface-immobilized substrates," Colloids Surfaces B Biointerfaces **131**, 115–121 (2015).

10. H. Arwin, M. Poksinski, and K. Johansen, "Total internal reflection ellipsometry: principles and applications.," Appl. Opt. **43**(15), 3028–3036 (2004).

11. A. V. Nabok, A. Tsargorodskaya, A. K. Hassan, and N. F. Starodub, "Total internal reflection ellipsometry and SPR detection of low molecular weight environmental toxins," Appl. Surf. Sci. **246**(4), 381–386 (2005).

12. K. Büchner, N. Ehrhardt, B. P. Cahill, and C. Hoffmann, "Internal reflection ellipsometry for real-time monitoring of polyelectrolyte multilayer growth onto tantalum pentoxide," Thin Solid Films **519**(19), 6480–6485 (2011).

13. S. Otsuki and M. Ishikawa, "Internal reflection ellipsometry in air and water ambient," Opt. Lett. **35**(24), 4226–4228 (2010).

14. S. Otsuki, K. Ohta, K. Tamada, and S. Wakida, "Thickness measurements on transparent substrates based on reflection ellipsometry. 1. Optical effects of high-refractive-index additional layers," Appl. Opt. **44**(28), 5910–5918 (2005).

15. S. Otsuki, K. Tamada, and S. Wakida, "Two-dimensional thickness measurements based on internal reflection ellipsometry.," Appl. Opt. **44**(8), 1410–5 (2005).

16. P. Drude, "Ueber die Gesetze der Reflexion und Brechung des Lichtes an der Grenze absorbirender Krystalle," Ann. der Phys. und Chemie **268**(12), 584–625 (1887).

17. R. M. A. Azzam and N. M. Bashara, *Ellipsometry and Polarized Light*, 2nd ed. (Elsevier, 1987).

18. H. G. Tompkins, *A User's Guide to Ellipsometry* (Academic Press, 1993).

19. A. Manallah and M. Bouafia, "Determination of Optical Constants of Semiconductor Thin Films by Ellipsometry," World Acad. Sci. Eng. Technol. Int. J. Chem. Mol. Nucl. Mater. Metall. Eng. **10**(7), 927–930 (2016).

20. H. Fujiwara, *Spectroscopic Ellipsometry Principles and Applications* (John Wiley & Sons, 2007).

21. Y. Guo, C. Divin, A. Myc, F. L. Terry, J. R. Baker, T. B. Norris, and J. Y. Ye, "Sensitive molecular binding assay using a photonic crystal structure in total internal reflection.," Opt. Express **16**(16), 11741–11749 (2008).

22. F. Goos and H. Hänchen, "Ein neuer und fundamentaler Versuch zur Totalreflexion," Ann. Phys. **436**(7–8), 333–346 (1947).

23. K. Johansen, H. Arwin, I. Lundström, and B. Liedberg, "Imaging surface plasmon resonance sensor based on multiple wavelengths: Sensitivity considerations," Rev. Sci. Instrum. **71**(9), 3530–3538 (2000).

24. T. Kovalevich, A. Ndao, M. Suarez, S. Tumenas, Z. Balevicius, A. Ramanavicius, I. Baleviciute, M. Häyrinen, M. Roussey, M. Kuittinen, T. Grosjean, and M.-P. Bernal, "Tunable Bloch surface waves in anisotropic photonic crystals based on lithium niobate thin films," Opt. Lett. **41**(23), 5616 (2016).

25. T. W. H. Oates, H. Wormeester, and H. Arwin, "Characterization of plasmonic effects in thin films and metamaterials using spectroscopic ellipsometry," Prog. Surf. Sci. **86**(11–12), 328–376 (2011).

26. R. A. Ferrell, "Predicted Radiation of Plasma Oscillations in Metal Films," Phys. Rev. **111**(5), 1214–1222 (1958).

27. R. H. Ritchie, "Plasma Losses by Fast Electrons in Thin Films," Phys. Rev. **106**(5), 874–881 (1957).

28. A. J. McAlister and E. A. Stern, "Plasma Resonance Absorption in Thin Metal Films," Phys. Rev. **132**(4), 1599–1602 (1963).

29. D. L. Mills and E. Burstein, "Polaritons: the electromagnetic modes of media," Reports Prog. Phys. **37**(7), 817–926 (1974).

30. S. A. Maier, *Plasmonics: Fundamentals and Applications* (Springer US, 2007).

31. M. Schubert, *Infrared Ellipsometry on Semiconductor Layer Structures*, Springer Tracts in Modern Physics (Springer Berlin Heidelberg, 2005), **209**.

32. Lord Rayleigh, "XVII. On the maintenance of vibrations by forces of double frequency, and on the propagation of waves through a medium endowed with a periodic structure," London, Edinburgh, Dublin Philos. Mag. J. Sci. **24**(147), 145–159 (1887).

33. E. Yablonovitch, "Inhibited Spontaneous Emission in Solid-State Physics and Electronics," Phys. Rev. Lett. **58**(20), 2059–2062 (1987).

34. S. John, "Strong localization of photons in certain disordered dielectric superlattices," Phys. Rev. Lett. **58**(23), 2486–2489 (1987).

35. G. von Freymann, V. Kitaev, B. V. Lotsch, and G. A. Ozin, "Bottom-up assembly of photonic crystals," Chem. Soc. Rev. **42**(7), 2528–2554 (2013).

36. K. Yoshino, Y. Shimoda, Y. Kawagishi, K. Nakayama, and M. Ozaki, "Temperature tuning of the stop band in transmission spectra of liquid-crystal infiltrated synthetic opal as tunable photonic crystal," Appl. Phys. Lett. **75**(7), 932–934 (1999).

37. J. Pol Vigneron, J.-F. Colomer, M. Rassart, A. L. Ingram, and V. Lousse, "Structural origin of the colored reflections from the black-billed magpie feathers," Phys. Rev. E **73**(2), 021914 (2006).

38. D. Gur, Y. Politi, B. Sivan, P. Fratzl, S. Weiner, and L. Addadi, "Guanine-Based Photonic Crystals in Fish Scales Form from an

Amorphous Precursor," Angew. Chemie **125**(1), 406–409 (2013).

39. P. Simonis and J. P. Vigneron, "Structural color produced by a three-dimensional photonic polycrystal in the scales of a longhorn beetle: Pseudomyagrus waterhousei (Coleoptera: Cerambicidae)," Phys. Rev. E **83**(1), 011908 (2011).

40. J. MATĚJKOVÁ-PLSKOVA, S. SHIOJIRI, and M. SHIOJIRI, "Fine structures of wing scales in Sasakia charonda butterflies as photonic crystals," J. Microsc. **236**(2), 88–93 (2009).

41. W. Geise and K. E. Linsenmair, "Adaptations of the reed frog Hyperolius viridiflavus (Amphibia, Anura, Hyperoliidae) to its arid environment," Oecologia **77**(3), 327–338 (1988).

42. J. Teyssier, S. V. Saenko, D. van der Marel, and M. C. Milinkovitch, "Photonic crystals cause active colour change in chameleons," Nat. Commun. **6**(1), 6368 (2015).

43. J. Park, J. Moon, H. Shin, D. Wang, and M. Park, "Direct-write fabrication of colloidal photonic crystal microarrays by ink-jet printing," J. Colloid Interface Sci. **298**(2), 713–719 (2006).

44. S. Kim, H. Chong, R. M. D. La Rue, J. H. Marsh, and A. C. Bryce, "Electron-beam writing of photonic crystal patterns using a large beam-spot diameter," Nanotechnology **14**(9), 1004–1008 (2003).

45. M. Scharrer, X. Wu, A. Yamilov, H. Cao, and R. P. H. Chang, "Fabrication of inverted opal ZnO photonic crystals by atomic layer deposition," Appl. Phys. Lett. **86**(15), 151113 (2005).

46. S. Shingubara, "Fabrication of Nanomaterials Using Porous Alumina Templates," J. Nanoparticle Res. **5**(1/2), 17–30 (2003).

47. M. Campbell, D. N. Sharp, M. T. Harrison, R. G. Denning, and A. J. Turberfield, "Fabrication of photonic crystals for the visible spectrum by holographic lithography," Nature **404**(6773), 53–56 (2000).

48. C. M. Soukoulis, "The history and a review of the modelling and

fabrication of photonic crystals," Nanotechnology **13**(3), 335 (2002).

49. Q. Wu, B. Liu, Z. Zhu, M. Gu, H. Chen, C. Xue, J. Zhao, Y. Wu, R. Tai, and X. Ouyang, "Directional emission of plastic luminescent films using photonic crystals fabricated by soft-X-ray interference lithography and reactive ion etching," Sci. Rep. **8**(1), 9254 (2018).

50. G. Calusine, A. Politi, and D. D. Awschalom, "Silicon carbide photonic crystal cavities with integrated color centers," Appl. Phys. Lett. **105**(1), 011123 (2014).

51. B. H. Juárez, P. D. García, D. Golmayo, A. Blanco, and C. López, "ZnO Inverse Opals by Chemical Vapor Deposition," Adv. Mater. **17**(22), 2761–2765 (2005).

52. I. E. Tamm, "On the possible bound states of electrons on a crystal surface," Phys. Z. Sowjetunion **1**, 733–735 (1932).

53. A. Kavokin, I. Shelykh, and G. Malpuech, "Optical Tamm states for the fabrication of polariton lasers," Appl. Phys. Lett. **87**(26), 261105 (2005).

54. M. E. Sasin, R. P. Seisyan, M. A. Kalitteevski, S. Brand, R. A. Abram, J. M. Chamberlain, A. Y. Egorov, A. P. Vasil'ev, V. S. Mikhrin, and A. V. Kavokin, "Tamm plasmon polaritons: Slow and spatially compact light," Appl. Phys. Lett. **92**(25), 251112 (2008).

55. M. Kaliteevski, I. Iorsh, S. Brand, R. A. Abram, J. M. Chamberlain, A. V. Kavokin, and I. A. Shelykh, "Tamm plasmon-polaritons: Possible electromagnetic states at the interface of a metal and a dielectric Bragg mirror," Phys. Rev. B **76**(16), 165415 (2007).

56. A. P. Vinogradov, A. V. Dorofeenko, S. G. Erokhin, M. Inoue, A. A. Lisyansky, A. M. Merzlikin, and A. B. Granovsky, "Surface state peculiarities in one-dimensional photonic crystal interfaces," Phys. Rev. B **74**(4), 045128 (2006).

57. M. E. Sasin, R. P. Seisyan, M. A. Kaliteevski, S. Brand, R. A. Abram, J. M. Chamberlain, I. V. Iorsh, I. A. Shelykh, A. Y. Egorov, A. P.

Vasil'ev, V. S. Mikhrin, and A. V. Kavokin, "Tamm plasmon-polaritons: First experimental observation," Superlattices Microstruct. **47**(1), 44–49 (2010).

58. S.-G. Huang, K.-P. Chen, and S.-C. Jeng, "Phase sensitive sensor on Tamm plasmon devices," Opt. Mater. Express **7**(4), 1267 (2017).

59. Y. Tsurimaki, J. K. Tong, V. N. Boriskin, A. Semenov, M. I. Ayzatsky, Y. P. Machekhin, G. Chen, and S. V. Boriskina, "Topological Engineering of Interfacial Optical Tamm States for Highly Sensitive Near-Singular-Phase Optical Detection," ACS Photonics **5**(3), 929–938 (2018).

60. B. Auguié, M. C. Fuertes, P. C. Angelomé, N. L. Abdala, G. J. A. A. Soler Illia, and A. Fainstein, "Tamm Plasmon Resonance in Mesoporous Multilayers: Toward a Sensing Application," ACS Photonics **1**(9), 775–780 (2014).

61. R. Das, T. Srivastava, and R. Jha, "Tamm-plasmon and surface-plasmon hybrid-mode based refractometry in photonic bandgap structures," Opt. Lett. **39**(4), 896 (2014).

62. H. Liu, X. Sun, F. Yao, Y. Pei, F. Huang, H. Yuan, and Y. Jiang, "Optical magnetic field enhancement through coupling magnetic plasmons to Tamm plasmons," Opt. Express **20**(17), 19160 (2012).

63. S. Azzini, G. Lheureux, C. Symonds, J.-M. Benoit, P. Senellart, A. Lemaitre, J.-J. Greffet, C. Blanchard, C. Sauvan, and J. Bellessa, "Generation and Spatial Control of Hybrid Tamm Plasmon/Surface Plasmon Modes," ACS Photonics **3**(10), 1776–1781 (2016).

64. B. I. Afinogenov, V. O. Bessonov, A. A. Nikulin, and A. A. Fedyanin, "Observation of hybrid state of Tamm and surface plasmon-polaritons in one-dimensional photonic crystals," Appl. Phys. Lett. **103**(6), 061112 (2013).

65. H. Arwin, "TIRE and SPR-Enhanced SE for Adsorption Processes," in *Ellipsometry of Functional Organic Surfaces and Films* (2014), pp. 249–264.

66. F. Abeles, "Optical properties of very thin films," Thin Solid Films **34**(2), 291–302 (1976).

67. E. Bortchagovsky, I. Yurchenko, Z. Kazantseva, J. Humliček, and J. Hora, "Spectroscopic ellipsometry of fullerene embedded Langmuir–Blodgett films with surface plasmon excitation," Thin Solid Films **313**–**314**, 795–798 (1998).

68. M. Poksinski and H. Arwin, "Total internal reflection ellipsometry: ultrahigh sensitivity for protein adsorption on metal surfaces," Opt. Lett. **32**(10), 1308 (2007).

69. P. Westphal and A. Bornmann, "Biomolecular detection by surface plasmon enhanced ellipsometry," Sensors Actuators B Chem. **84**(2–3), 278–282 (2002).

70. Z. Balevicius, R. Drevinskas, M. Dapkus, G. J. Babonas, A. Ramanaviciene, and A. Ramanavicius, "Total internal reflection ellipsometry of metal-organic compound structures modified with gold nanoparticles," Thin Solid Films **519**(9), 2959–2962 (2011).

71. Y. Guo, C. Divin, A. Myc, F. L. Terry Jr., J. R. Baker Jr., T. B. Norris, and J. Y. Ye, "Sensitive molecular binding assay using a photonic crystal structure in total internal reflection," Opt. Express **16**(16), 11741 (2008).

72. T. Kovalevich, A. Ndao, M. Suarez, S. Tumenas, Z. Balevicius, A. Ramanavicius, I. Baleviciute, M. Häyrinen, M. Roussey, M. Kuittinen, T. Grosjean, and M.-P. Bernal, "Tunable Bloch surface waves in anisotropic photonic crystals based on lithium niobate thin films," Opt. Lett. **41**(23), 5616–5619 (2016).

73. H. Raether, *Surface Plasmons on Smooth and Rough Surfaces and on Gratings*, Springer Tracts in Modern Physics (Springer Berlin Heidelberg, 1988), **111**.

74. J. W. Elam and S. M. George, "Growth of ZnO/Al2O3 Alloy Films Using Atomic Layer Deposition Techniques," Chem. Mater. **15**(4), 1020–1028 (2003).

75. R. Raghavan, M. Bechelany, M. Parlinska, D. Frey, W. M. Mook, A. Beyer, J. Michler, and I. Utke, "Nanocrystalline-to-amorphous transition in nanolaminates grown by low temperature atomic layer deposition and related mechanical properties," Appl. Phys. Lett. **100**(19), 191912 (2012).

76. E. Härkönen, B. Díaz, J. Światowska, V. Maurice, A. Seyeux, M. Vehkamäki, T. Sajavaara, M. Fenker, P. Marcus, and M. Ritala, "Corrosion Protection of Steel with Oxide Nanolaminates Grown by Atomic Layer Deposition," J. Electrochem. Soc. **158**(11), C369 (2011).

77. D. M. Hausmann and R. G. Gordon, "Surface morphology and crystallinity control in the atomic layer deposition (ALD) of hafnium and zirconium oxide thin films," J. Cryst. Growth **249**(1–2), 251–261 (2003).

78. K. Koski, J. Hölsä, and P. Juliet, "Properties of aluminium oxide thin films deposited by reactive magnetron sputtering," Thin Solid Films **339**(1–2), 240–248 (1999).

79. R. Viter, I. Baleviciute, A. Abou Chaaya, L. Mikoliunaite, Z. Balevicius, A. Ramanavicius, A. Zalesska, V. Vataman, V. Smyntyna, Z. Gertnere, D. Erts, P. Miele, and M. Bechelany, "Optical properties of ultrathin Al2O3/ZnO nanolaminates," Thin Solid Films **594**, 96–100 (2015).

80. A. A. Chaaya, R. Viter, I. Baleviciute, M. Bechelany, A. Ramanavicius, Z. Gertnere, D. Erts, V. Smyntyna, and P. Miele, "Tuning Optical Properties of Al2O3 /ZnO Nanolaminates Synthesized by Atomic Layer Deposition," J. Phys. Chem. C **118**(7), 3811–3819 (2014).

81. S. K. Arya, S. Saha, J. E. Ramirez-Vick, V. Gupta, S. Bhansali, and S. P. Singh, "Recent advances in ZnO nanostructures and thin films for biosensor applications: Review," Anal. Chim. Acta **737**, 1–21 (2012).

82. D. J. Kang, J. S. Kim, S. W. Jeong, Y. Roh, S. H. Jeong, and J. H. Boo, "Structural and electrical characteristics of R.F. magnetron sputtered ZnO films," Thin Solid Films **475**(1–2), 160–165 (2005).

83. R. Viter, I. Iatsunskyi, V. Fedorenko, S. Tumenas, Z. Balevicius, A. Ramanavicius, S. Balme, M. Kempiński, G. Nowaczyk, S. Jurga, and M. Bechelany, "Enhancement of Electronic and Optical Properties of ZnO/Al2O3 Nanolaminate Coated Electrospun Nanofibers," J. Phys. Chem. C **120**(9), 5124–5132 (2016).

84. R. Yakimova, "ZnO materials and surface tailoring for biosensing," Front. Biosci. **E4**(1), 254 (2012).

85. J. X. Wang, X. W. Sun, A. Wei, Y. Lei, X. P. Cai, C. M. Li, and Z. L. Dong, "Zinc oxide nanocomb biosensor for glucose detection," Appl. Phys. Lett. **88**(23), (2006).

86. P. I. Reyes, Z. Zhang, H. Chen, Z. Duan, J. Zhong, G. Saraf, Y. Lu, O. Taratula, E. Galoppini, and N. N. Boustany, "A ZnO nanostructure-based quartz crystal microbalance device for biochemical sensing," IEEE Sens. J. **9**(10), 1302–1307 (2009).

87. H. Fujiwara, J. Koh, P. I. Rovira, and R. W. Collins, "Assessment of effective-medium theories in the analysis of nucleation and microscopic surface roughness evolution for semiconductor thin films," Phys. Rev. B **61**(16), 10832–10844 (2000).

88. H. G. Tompkins and A. E. Irene, eds., *Handbook of Ellipsometry* (William Andrew, 2005).

89. V. G. Kravets, F. Schedin, R. Jalil, L. Britnell, R. V. Gorbachev, D. Ansell, B. Thackray, K. S. Novoselov, A. K. Geim, A. V. Kabashin, and A. N. Grigorenko, "Singular phase nano-optics in plasmonic metamaterials for label-free single-molecule detection," Nat. Mater. **12**(4), 304–309 (2013).

90. V. Kriechbaumer, A. Tsargorodskaya, M. K. Mustafa, T. Vinogradova, J. Lacey, D. P. Smith, B. M. Abell, and A. Nabok, "Study of Receptor-Chaperone Interactions Using the Optical Technique of Spectroscopic Ellipsometry," Biophys. J. **101**(2), 504–511 (2011).

91. Z. Balevicius, A. Ramanaviciene, I. Baleviciute, A. Makaraviciute, L. Mikoliunaite, and A. Ramanavicius, "Evaluation of intact- and

fragmented-antibody based immunosensors by total internal reflection ellipsometry," Sensors Actuators B Chem. **160**(1), 555–562 (2011).

92. I. Baleviciute, Z. Balevicius, A. Makaraviciute, A. Ramanaviciene, and A. Ramanavicius, "Study of antibody/antigen binding kinetics by total internal reflection ellipsometry," Biosens. Bioelectron. **39**(1), 170–176 (2013).

93. Z. Balevicius, A. Makaraviciute, G.-J. Babonas, S. Tumenas, V. Bukauskas, A. Ramanaviciene, and A. Ramanavicius, "Study of optical anisotropy in thin molecular layers by total internal reflection ellipsometry," Sensors Actuators B Chem. **181**, 119–124 (2013).

94. M. K. Mustafa, A. Nabok, D. Parkinson, I. E. Tothill, F. Salam, and A. Tsargorodskaya, "Detection of β-amyloid peptide (1–16) and amyloid precursor protein (APP770) using spectroscopic ellipsometry and QCM techniques: A step forward towards Alzheimers disease diagnostics," Biosens. Bioelectron. **26**(4), 1332–1336 (2010).

95. A. Nabok, A. Tsargorodskaya, A. Holloway, N. F. Starodub, and A. Demchenko, "Specific Binding of Large Aggregates of Amphiphilic Molecules to the Respective Antibodies," Langmuir **23**(16), 8485–8490 (2007).

96. M. Erber, J. Stadermann, and K.-J. Eichhorn, "Total Internal Reflection Ellipsometry under SPR Conditions: In-Situ Monitoring of the Growth of Poly(N-isopropylacrylamide) (PNIPAAm) Brushes," Macromol. Symp. **305**(1), 101–107 (2011).

97. B. Celen, G. Demirel, and E. Piskin, "Micro-array versus nano-array platforms: a comparative study for ODN detection based on SPR enhanced ellipsometry," Nanotechnology **22**(16), 165501 (2011).

98. S.-H. Kim, W. Chegal, J. Doh, H. M. Cho, and D. W. Moon, "Study of Cell-Matrix Adhesion Dynamics Using Surface Plasmon Resonance Imaging Ellipsometry," Biophys. J. **100**(7), 1819–1828 (2011).

99. G. Jin, Y. H. Meng, L. Liu, Y. Niu, S. Chen, Q. Cai, and T. J. Jiang, "Development of biosensor based on imaging ellipsometry and

biomedical applications," Thin Solid Films **519**(9), 2750–2757 (2011).

100. T. Basova, A. Tsargorodskaya, A. Nabok, A. K. Hassan, A. G. Gürek, G. Gümüş, and V. Ahsen, "Investigation of gas-sensing properties of copper phthalocyanine films," Mater. Sci. Eng. C **29**(3), 814–818 (2009).

101. A. Nooke, U. Beck, A. Hertwig, A. Krause, H. Krüger, V. Lohse, D. Negendank, and J. Steinbach, "On the application of gold based SPR sensors for the detection of hazardous gases," Sensors Actuators B Chem. **149**(1), 194–198 (2010).

102. J. Mårtensson, H. Arwin, and I. Lundström, "Thin films of phthalocyanines studied with spectroscopic ellipsometry: an optical gas sensor?," Sensors Actuators B Chem. **1**(1–6), 134–137 (1990).

103. S. Otsuki and M. Ishikawa, "Internal reflection ellipsometry in air and water ambient," Opt. Lett. **35**(24), 4226 (2010).

104. S. Rekveld, "Ellipsometric Studies of Protein Adsorption onto Hard Surfaces in a Flow Cell," University of Twent (1997).

105. M. Poksinski and H. Arwin, "In situ monitoring of metal surfaces exposed to milk using total internal reflection ellipsometry," Sensors Actuators B Chem. **94**(3), 247–252 (2003).

106. M. Poksinski and H. Arwin, "Protein monolayers monitored by internal reflection ellipsometry," Thin Solid Films **455**–**456**, 716–721 (2004).

107. M. Baitimirova, R. Viter, J. Andzane, A. Van Der Lee, D. Voiry, I. Iatsunskyi, E. Coy, L. Mikoliunaite, S. Tumenas, K. Zaleski, Z. Balevicius, I. Baleviciute, A. Ramanaviciene, A. Ramanavicius, S. Jurga, D. Erts, and M. Bechelany, "Tuning of Structural and Optical Properties of Graphene/ZnO Nanolaminates," J. Phys. Chem. C **120**(41), 23716–23725 (2016).

108. M. Zhu, M. Z. Lerum, and W. Chen, "How to prepare reproducible, homogeneous, and hydrolytically stable aminosilane-derived layers on

silica," Langmuir **28**(1), 416–423 (2012).

109. "SCHOTT datasheet overview," https://www.schott.com/d/advanced_optics/6959f9a4-0e4f-4ef2-a302-2347468a82f5/1.29/schott-optical-glass-overview-zemax-format-english-20180601.zip.

110. T. Inagaki, E. T. Arakawa, and M. W. Williams, "Optical properties of liquid mercury," Phys. Rev. B **23**(10), 5246–5262 (1981).

111. C. M. Herzinger, B. Johs, W. A. McGahan, J. A. Woollam, and W. Paulson, "Ellipsometric determination of optical constants for silicon and thermally grown silicon dioxide via a multi-sample, multi-wavelength, multi-angle investigation," J. Appl. Phys. **83**(6), 3323–3336 (1998).

112. D. I. Yakubovsky, A. V. Arsenin, Y. V. Stebunov, D. Y. Fedyanin, and V. S. Volkov, "Optical constants and structural properties of thin gold films," Opt. Express **25**(21), 25574 (2017).

113. J. A. Woollam, "CompleteEASE," .

114. R. M. Azzam, M. Elshazly-Zaghloul, and N. M. Bashara, "Combined reflection and transmission thin-film ellipsometry: a unified linear analysis.," Appl. Opt. **14**(7), 1652–1663 (1975).

115. W. A. McGahan, B. Johs, and J. A. Woollam, "Techniques for ellipsometric measurement of the thickness and optical constants of thin absorbing films," Thin Solid Films **234**(1–2), 443–446 (1993).

116. S. E. Schober, T. H. Sinks, R. L. Jones, P. M. Bolger, M. Mcdowell, J. Osterloh, E. S. Garrett, R. A. Canady, C. F. Dillon, Y. Sun, C. B. Joseph, and K. R. Mahaffey, "Blood Mercury Levels in US Children and Women of Childbearing Age , 1999-2000," J. Am. Med. Assoc. **289**(13), 1667–1674 (2003).

117. D. C. Evers, Y.-J. Han, C. T. Driscoll, N. C. Kamman, M. W. Goodale, K. F. Lambert, T. M. Holsen, C. Y. Chen, T. a. Clair, T. Butler, and R. K. Munson, "Mercury Contamination in Forest and Freshwater

Ecosystems in the Northeastern United States," Bioscience **57**(1), 29–43 (2007).

118. A. Carpi, "Mercury from combustion sources: A review of the chemical species emitted and their transport in the atmosphere," Water. Air. Soil Pollut. **98**(3–4), 241–254 (1997).

119. K. Vikrant and K.-H. Kim, "Nanomaterials for the adsorptive treatment of Hg(II) ions from water," Chem. Eng. J. **358**, 264–282 (2019).

120. R. L. Lancione and D. M. Drew, "Evaluation of ICP atomic fluorescence for the determination of mercury," Spectrochim. Acta Part B At. Spectrosc. **40**(1–2), 107–113 (1985).

121. D. S. Bushee, "Speciation of Mercury Using Liquid-Chromatography With Detection By Inductively Coupled Plasma Mass-Spectrometry," Analyst **113**(8), 1167–1170 (1988).

122. N. Bloom and W. F. Fitzgerald, "Determination of volatile mercury species at the picogram level by low-temperature gas chromatography with cold-vapour atomic fluorescence detection," Anal. Chim. Acta **208**(C), 151–161 (1988).

123. W. R. Hatch and W. L. Ott, "Determination of submicrogram quantities of mercury by atomic absorption spectrophotometry," Anal. Chem. **40**(14), 2085–2087 (1968).

124. A. Urba, K. Kvietkus, J. Sakalys, Z. Xiao, and O. Lindqvist, "A New Sensitive and Portable Mercury Vapor Analyzer Gardis-1A," in *Mercury as a Global Pollutant* (Springer Netherlands, 1995), pp. 1305–1309.

125. A. Urba, K. Kvietkus, and R. Marks, "Gas-phase mercury in the atmosphere over the southern Baltic Sea coast," Sci. Total Environ. **259**(1–3), 203–210 (2000).

126. T.-H. Kuo, C.-F. Chang, A. Urba, and K. Kvietkus, "Atmospheric gaseous mercury in Northern Taiwan," Sci. Total Environ. **368**(1), 10–18 (2006).

127. J. Šakalys, K. Kvietkus, I. Garbarienė, and A. Urba, "Long-term study of atmospheric mercury deposition at monitoring stations in Lithuania," Lith. J. Phys. **59**(1), (2019).

128. A. Urba, D. Valiulis, J. Šarlauskas, K. Kvietkus, J. Šakalys, and A. Selskis, "A pilot study of different materials applied for active sampling of gaseous oxidized mercury in the atmospheric air," Atmos. Pollut. Res. **8**(4), 791–799 (2017).

129. M. Amyot, G. A. Gill, and F. M. M. Morel, "Production and loss of dissolved gaseous mercury in coastal seawater," Environ. Sci. Technol. **31**(12), 3606–3611 (1997).

130. H.-T. Wang, B. S. Kang, T. F. Chancellor, T. P. Lele, Y. Tseng, F. Ren, S. J. Pearton, W. J. Johnson, P. Rajagopal, J. C. Roberts, E. L. Piner, and K. J. Linthicum, "Fast electrical detection of Hg(II) ions with AlGaN/GaN high electron mobility transistors," Appl. Phys. Lett. **91**(May), 42114–421143 (2007).

131. B. Mazzolai, V. Mattoli, V. Raffa, G. Tripoli, D. Accoto, A. Menciassi, and P. Dario, "A microfabricated physical sensor for atmospheric mercury monitoring," Sensors Actuators, A Phys. **113**(3), 282–287 (2004).

132. Y. M. Sabri, S. J. Ippolito, J. Tardio, A. J. Atanacio, D. K. Sood, and S. K. Bhargava, "Mercury diffusion in gold and silver thin film electrodes on quartz crystal microbalance sensors," Sensors Actuators, B Chem. **137**(1), 246–252 (2009).

133. Y. M. Sabri, S. J. Ippolito, J. Tardio, and S. K. Bhargava, "Study of surface morphology effects on Hg sorption-desorption kinetics on gold thin-films," J. Phys. Chem. C **116**(3), 2483–2492 (2012).

134. T. Hou, M. Chen, G. W. Greene, and R. G. Horn, "Mercury Vapor Sorption and Amalgamation with a Thin Gold Film," ACS Appl. Mater. Interfaces **7**(41), 23172–23181 (2015).

135. T. Morris and G. Szulczewski, "Evaluating the Role of Coinage Metal Films in the Detection of Mercury Vapor by Surface Plasmon

Resonance Spectroscopy," Langmuir **18**(15), 5823–5829 (2002).

136. M. Vasjari, Y. M. Shirshov, A. V. Samoylov, and V. M. Mirsky, "SPR investigation of mercury reduction and oxidation on thin gold electrodes," J. Electroanal. Chem. **605**(1), 73–76 (2007).

137. C. Wang, L. Ma, M. Hossain, H. Wang, S. Zou, J. J. Hickman, and M. Su, "Direct visualization of molecular scale chemical adsorptions on solids using plasmonic nanoparticle arrays," Sensors Actuators, B Chem. **150**(2), 667–672 (2010).

138. J. Z. James, D. Lucas, and C. P. Koshland, "Gold nanoparticle films as sensitive and reusable elemental mercury sensors," Environ. Sci. Technol. **46**(17), 9557–9562 (2012).

139. T. Morris, K. Kloepper, S. Wilson, and G. Szulczewski, "A spectroscopic study of mercury vapor adsorption on gold nanoparticle films.," J. Colloid Interface Sci. **254**, 49–55 (2002).

140. T. Hou, M. Chen, G. W. Greene, and R. G. Horn, "Mercury Vapor Sorption and Amalgamation with a Thin Gold Film," ACS Appl. Mater. Interfaces **7**(41), 23172–23181 (2015).

141. M. Levlin, E. Ikävalko, and T. Laitinen, "Adsorption of mercury on gold and silver surfaces," Fresenius. J. Anal. Chem. **365**(7), 577–586 (1999).

142. N. A. Joy, M. I. Nandasiri, P. H. Rogers, W. Jiang, T. Varga, S. V. N. T. Kuchibhatla, S. Thevuthasan, and M. A. Carpenter, "Selective Plasmonic Gas Sensing: H2 , NO2 , and CO Spectral Discrimination by a Single Au-CeO2 Nanocomposite Film," Anal. Chem. **84**(11), 5025–5034 (2012).

143. Z. Balevicius, V. Vaicikauskas, and G. J. Babonas, "The role of surface roughness in total internal reflection ellipsometry of hybrid systems," Appl. Surf. Sci. **256**(3), 640–644 (2009).

144. C. Battistoni, E. Bemporad, A. Galdikas, S. Kačiulis, G. Mattogno, S. Mickevičius, and V. Olevano, "Interaction of mercury vapour with thin

films of gold," Appl. Surf. Sci. **103**(2), 107–111 (1996).

145. M. A. Butler, A. J. Ricco, and R. J. Baughman, "Hg adsorption on optically thin Au films," J. Appl. Phys. **67**(9), 4320–4326 (1990).

146. E. Palik, *Handbook of Optical Constants of Solids: Index* (1998), (225).

147. T. Morris and G. Szulczewski, "A Spectroscopic Ellipsometry, Surface Plasmon Resonance, and X-ray Photoelectron Spectroscopy Study of Hg Adsorption on Gold Surfaces," Langmuir **18**(6), 2260–2264 (2002).

148. A. Nooke, "Gas Detection by Means of Surface Plasmon Resonance Enhanced Ellipsometry," Technischen Universitat (2012).

149. W. L. Barnes, "Surface plasmon–polariton length scales: a route to sub-wavelength optics," J. Opt. A Pure Appl. Opt. **8**(4), S87–S93 (2006).

150. M. A. George and W. S. Glaunsinger, "The electrical and structural properties of gold films and mercury-covered gold films," Thin Solid Films **245**(1–2), 215–224 (1994).

151. M. Levlin, H. E.-M. Niemi, P. Hautojärvi, E. Ikävalko, and T. Laitinen, "Mercury adsorption on gold surfaces employed in the sampling and determination of vaporous mercury: a scanning tunneling microscopy study," Fresenius J. Anal. Chem. **355**(1), 2–9 (1996).

152. P. Törmä and W. L. Barnes, "Strong coupling between surface plasmon polaritons and emitters: a review," Reports Prog. Phys. **78**(1), 013901 (2015).

153. L. Novotny, "Strong coupling, energy splitting, and level crossings: A classical perspective," Am. J. Phys. **78**(11), 1199–1202 (2010).

154. H. Arwin, "TIRE and SPR-Enhanced SE for Adsorption Processes," in *Ellipsometry of Functional Organic Surfaces and Films* (Springer, 2018), pp. 419–435.

155. J. A. De Feijter, J. Benjamins, and F. A. Veer, "Ellipsometry as a tool to study the adsorption behavior of synthetic and biopolymers at the air–water interface," Biopolymers **17**(7), 1759–1772 (1978).

156. V. Ball and J. J. Ramsden, "Buffer dependence of refractive index increments of protein solutions," Biopolymers **46**(7), 489–492 (1998).

157. D. Thapa, J. Huso, J. L. Morrison, C. D. Corolewski, M. D. McCluskey, and L. Bergman, "Achieving highly-enhanced UV photoluminescence and its origin in ZnO nanocrystalline films," Opt. Mater. (Amst). **58**, 382–389 (2016).

158. R. Viter, Z. Balevicius, A. Abou Chaaya, I. Baleviciute, S. Tumenas, L. Mikoliunaite, A. Ramanavicius, Z. Gertnere, A. Zalesska, V. Vataman, V. Smyntyna, D. Erts, P. Miele, and M. Bechelany, "The influence of localized plasmons on the optical properties of Au/ZnO nanostructures," J. Mater. Chem. C **3**(26), 6815–6821 (2015).

159. Z. Balevicius, I. Baleviciute, S. Tumenas, L. Tamosaitis, A. Stirke, A. Makaraviciute, A. Ramanaviciene, and A. Ramanavicius, "In situ study of ligand–receptor interaction by total internal reflection ellipsometry," Thin Solid Films **571**, 744–748 (2014).

UŽRAŠAMS

UŽRAŠAMS

Vilniaus universiteto leidykla
Saulėtekio al. 9, LT-10222 Vilnius
El. p. info@leidykla.vu.lt,
www.leidykla.vu.lt
Tiražas 15 egz.